Review

International Journal of Modern Physics E
Vol. 30, No. 2 (2021) 2130001 (106 pages)

DOI: 10.1142/S0218301321300010

World Scientific
www.worldscientific.com

Dynamics of QCD matter — current status

Amaresh Jaiswal[*,§§§§§], Najmul Haque[*,¶¶¶¶¶], Aman Abhishek[†], Raktim Abir[‡], Aritra Bandyopadhyay[§], Khatiza Banu[‡], Samapan Bhadury[*], Sumana Bhattacharyya[¶], Trambak Bhattacharyya[‖,‖‖‖‖‖‖], Deeptak Biswas[¶], H. C. Chandola[**], Vinod Chandra[††], Bhaswar Chatterjee[‡‡], Chandrodoy Chattopadhyay[§§], Nilanjan Chaudhuri[¶¶,‖‖], Aritra Das[‖‖,***], Arpan Das[†], Santosh K. Das[†††], Ashutosh Dash[*], Kishan Deka[*], Jayanta Dey[‡‡‡], Ricardo L. S. Farias[§], Utsab Gangopadhyaya[¶¶], Ritesh Ghosh[***], Sabyasachi Ghosh[‡‡‡], Snigdha Ghosh[***], Ulrich Heinz[§§], Sunil Jaiswal[§§§], Guruprasad Kadam[¶¶¶], Pallavi Kalikotay[‖‖‖], Bithika Karmakar[***], Gastão Krein[****], Avdhesh Kumar[††††], Deepak Kumar[†,††], Lokesh Kumar[‡‡‡‡], Manu Kurian[††], Soumitra Maity[¶], Hiranmaya Mishra[†], Payal Mohanty[*], Ranjita K. Mohapatra[§§§§], Arghya Mukherjee[***], Munshi G. Mustafa[***], Subrata Pal[§§§], H. C. Pandey[¶¶¶¶], Mahfuzur Rahaman[¶¶], Ralf Rapp[‖‖‖‖‖], Deependra Singh Rawat[**], Sutanu Roy[*], Victor Roy[*], Kinkar Saha[*****], Nihar R. Sahoo[†††††], Subhasis Samanta[*], Sourav Sarkar[¶¶, ‖‖], Sarthak Satapathy[‡‡‡], Fernando E. Serna[****], Mariyah Siddiqah[‡], Pracheta Singha[¶], V. Sreekanth[‡‡‡‡‡], Sudipa Upadhaya[¶¶], Nahid Vasim[‡] and Dinesh Yadav[**]

[*]*National Institute of Science Education and Research, HBNI, Jatni 752050, Odisha, India*

[†]*Theory Division, Physical Research Laboratory, Navrangpura, Ahmedabad 380 009, India*

[‡]*Department of Physics, Aligarh Muslim University, Aligarh (U.P.)-202002, India*

[§]*Departamento de Física, Universidade Federal de Santa Maria, Santa Maria, RS, 97105-900, Brazil*

[¶]*Center for Astroparticle Physics & Space Science, Bose Institute, EN-80, Sector-5, Bidhan Nagar, Kolkata-700091, India*

[‖] *University of Cape Town, Rondebosch 7701, Cape Town, South Africa*

[**]*Department of Physics (UGC- of Advanced Study), Kumaun University, Nainital, India*

[††]*Indian Institute of Technology Gandhinagar, Gandhinagar 382 355, Gujarat, India*

[‡‡]*Department of Physics, Indian Institute of Technology Roorkee, Roorkee 247 667, India*

[§§]*Department of Physics, The Ohio State University, Columbus, Ohio 43210-1117, USA*

[§§§§§,¶¶¶¶¶]Corresponding authors.

¶¶*Variable Energy Cyclotron Centre,*
1/AF Bidhan Nagar, Kolkata 700 064, India

‖‖*Homi Bhabha National Institute, Training School Complex,*
Anushaktinagar, Mumbai - 400085, India

****Saha Institute of Nuclear Physics,*
1/AF Bidhan Nagar, Kolkata 700064, India

†††*School of Physical Sciences,*
Indian Institute of Technology Goa, Ponda-403401, Goa, India

‡‡‡*Indian Institute of Technology Bhilai,*
GEC Campus, Sejbahar, Raipur 492015, Chhattisgarh, India

§§§*Department of Nuclear and Atomic Physics,*
Tata Institute of Fundamental Research, Mumbai 400005, India

¶¶¶*Department of Physics, Shivaji University,*
Kolhapur, Maharashtra-416004, India

‖‖‖*Department of Physics, Kazi Nazrul University,*
Asansol - 713340, West Bengal, India

*****Instituto de Física Teórica,*
Universidade Estadual Paulista, Rua Dr. Bento Teobaldo Ferraz,
271 - Bloco II, 01140-070 São Paulo, SP, Brazil

††††*Institute of Nuclear Physics Polish Academy of Sciences,*
PL-31-342 Kraków, Poland

‡‡‡‡*Department of Physics, Panjab University, Chandigarh, 160014, India*

§§§§*Department of Physics, Indian Institute of Technology Bombay,*
Mumbai, 400076, India

¶¶¶¶*Birla Institute of Applied Sciences, Bhimtal, India*

‖‖‖‖*Texas A & M University,*
Department of Physics and Astronomy and Cyclotron Institute,
College Station, TX 77843-3366, USA

******Department of Physics, University of Calcutta,*
92, A. P. C. Road, Kolkata - 700009, India

†††††*Shandong University, Qingdao, P. R. China*

‡‡‡‡‡*Department of Sciences, Amrita School of Engineering,*
Coimbatore, Amrita Vishwa Vidyapeethom, India

‖‖‖‖‖‖‖*Presently at Bogoliubov Laboratory of Theoretical Physics,*
Joint Institute for Nuclear Research, Dubna, 141980,
Moscow region, Russian Federation

§§§§§*a.jaiswal@niser.ac.in*
¶¶¶¶¶*nhaque@niser.ac.in*

Received 21 October 2020
Revised 24 December 2020
Accepted 24 December 2020
Published 24 February 2021

In this article, there are 18 sections discussing various current topics in the field of relativistic heavy-ion collisions and related phenomena, which will serve as a snapshot of the current state of the art. Section 1 reviews experimental results of some recent light-flavored particle production data from ALICE collaboration. Other sections are

mostly theoretical in nature. Very strong but transient magnetic field created in relativistic heavy-ion collisions could have important observational consequences. This has generated a lot of theoretical activity in the last decade. Sections 2, 7, 9, 10 and 11 deal with the effects of the magnetic field on the properties of the QCD matter. More specifically, Sec. 2 discusses mass of π^0 in the linear sigma model coupled to quarks at zero temperature. In Sec. 7, one-loop calculation of the anisotropic pressure are discussed in the presence of strong magnetic field. In Sec. 9, chiral transition and chiral susceptibility in the NJL model is discussed for a chirally imbalanced plasma in the presence of magnetic field using a Wigner function approach. Sections 10 discusses electrical conductivity and Hall conductivity of hot and dense hadron gas within Boltzmann approach and Sec. 11 deals with electrical resistivity of quark matter in presence of magnetic field. There are several unanswered questions about the QCD phase diagram. Sections 3, 11 and 18 discuss various aspects of the QCD phase diagram and phase transitions. Recent years have witnessed interesting developments in foundational aspects of hydrodynamics and their application to heavy-ion collisions. Sections 12 and 15–17 of this article probe some aspects of this exciting field. In Sec. 12, analytical solutions of viscous Landau hydrodynamics in 1+1D are discussed. Section 15 deals with derivation of hydrodynamics from effective covariant kinetic theory. Sections 16 and 17 discuss hydrodynamics with spin and analytical hydrodynamic attractors, respectively. Transport coefficients together with their temperature- and density-dependence are essential inputs in hydrodynamical calculations. Sections 5, 8 and 14 deal with calculation/estimation of various transport coefficients (shear and bulk viscosity, thermal conductivity, relaxation times, etc.) of quark matter and hadronic matter. Sections 4, 6 and 13 deal with interesting new developments in the field. Section 4 discusses color dipole gluon distribution function at small transverse momentum in the form of a series of Bells polynomials. Section 6 discusses the properties of Higgs boson in the quark–gluon plasma using Higgs–quark interaction and calculate the Higgs decays into quark and anti-quark, which shows a dominant on-shell contribution in the bottom-quark channel. Section 13 discusses modification of coalescence model to incorporate viscous corrections and application of this model to study hadron production from a dissipative quark–gluon plasma.

Keywords: Quark gluon plasma; relativistic heavy ion collisions; quantum chromodynamics.

PACS Number(s): 12.38.−t, 12.38.Aw, 12.38.Mh, 25.75.−q, 25.75.Nq

1. Recent Selected Results from ALICE on Particle Production

Lokesh Kumar

We present a selection of recent results on light-flavored particle production from ALICE experiment. The results are presented on the charge particle multiplicity, average transverse momentum, kinetic freeze-out parameters, enhancement of strangeness production, suppression of resonance yields in central nucleus–nucleus collisions, and first experimental observation of spin–orbit coupling in high-energy heavy-ion collisions, latest estimation of hypertriton lifetime from ALICE. Comparison of these results among several collision systems such as pp, p–Pb, Pb–Pb and Xe–Xe at various center-of-mass energies is presented.

1.1. *Introduction*

The ALICE experiment at the Large Hadron Collider has collected a large amount of data for various systems and energies. In view of the large data sample collected

in small systems, it is possible to study the multiplicity dependence of various observables. Many interesting observations have come out of ALICE by comparing results from of small systems pp and p–Pb with large systems Pb–Pb and Xe–Xe. We present a selection of recent results, mostly on light-flavored particle production.

1.2. *Collectivity*

Figure 1 shows the new results on charged particle pseudorapidity density for various centrality classes over a broad range of η in Xe–Xe collisions at $\sqrt{s_{\rm NN}} = 5.44\,\text{TeV}$.[1] The data are presented for 12 centrality classes. At midrapidity, the $\langle dN_{\rm ch}/d\eta\rangle$ is about 1302 ± 17 for Xe–Xe at $\sqrt{s_{\rm NN}} = 5.44\,\text{TeV}$. The charged particle multiplicity has been measured for small systems as well as Pb–Pb collisions and it is observed that energy dependence behavior of midrapidity $\langle dN_{\rm ch}/d\eta\rangle/(0.5\langle N_{\rm part}\rangle)$ is different for small systems and large systems. The $\langle dN_{\rm ch}/d\eta\rangle/(0.5\langle N_{\rm part}\rangle)$ does not scale with number of participant nucleons $\langle N_{\rm part}\rangle$; however, it scales approximately with number of wounded constituent quarks $\langle N_{\rm q-part}\rangle$ calculated using quark–Glauber parameterization.[2]

Figure 2 shows the average transverse momentum $\langle p_T\rangle$ of identified hadrons plotted as a function of $\langle dN_{\rm ch}/d\eta\rangle_{|\eta|<0.5}$ in different collision systems pp, p–Pb, Xe–Xe and Pb–Pb at various center-of-mass energies.[3] In general, the $\langle p_T\rangle$ increases with increasing multiplicity for all systems and energies. It is observed that for central A–A collisions, the $\langle p_T\rangle$ increases with mass of hadrons. This is referred to as the mass ordering and is consistent with hydrodynamical behavior. As can be seen, the proton and $\phi(1020)$ meson having similar masses have same $\langle p_T\rangle$ values in central A–A collisions. However, in peripheral A–A, p–Pb and pp collisions, the mass ordering seems to be violated for $\phi(1020)$ mesons whereas it is observed that its $\langle p_T\rangle$ even exceeds those of protons and Λ. It is also observed that the increase in $\langle p_T\rangle$ with $\langle dN_{\rm ch}/d\eta\rangle_{|\eta|<0.5}$ is faster in light systems than in heavy ions.

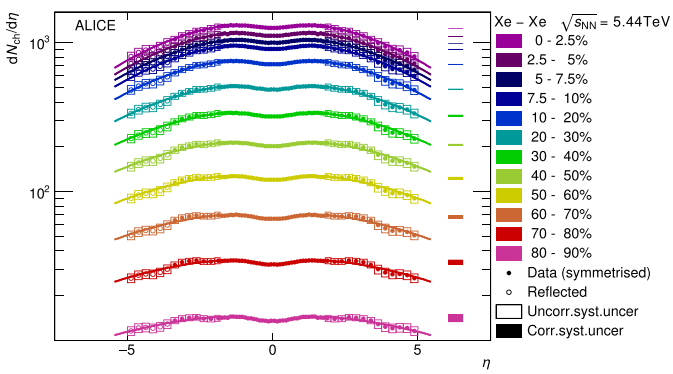

Fig. 1. Charged particle pseudorapidity density for various centrality classes over a broad range of η in Xe–Xe collisions at $\sqrt{s_{\rm NN}} = 5.44\,\text{TeV}$.[1]

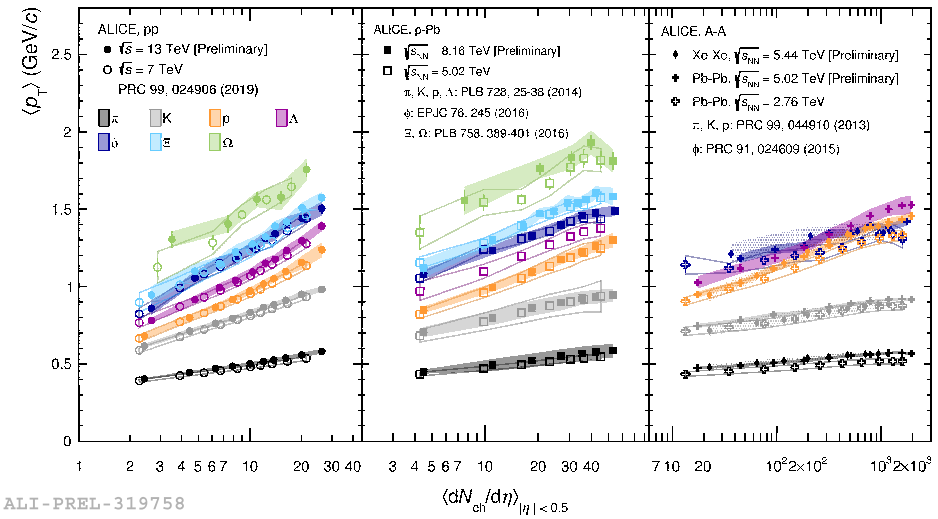

Fig. 2. Average transverse momentum $\langle p_T \rangle$ of identified hadrons as a function of $\langle dN_{\rm ch}/d\eta \rangle_{|\eta|<0.5}$ in different collision systems pp, p–Pb, Xe–Xe and Pb–Pb at various center-of-mass energies.[3]

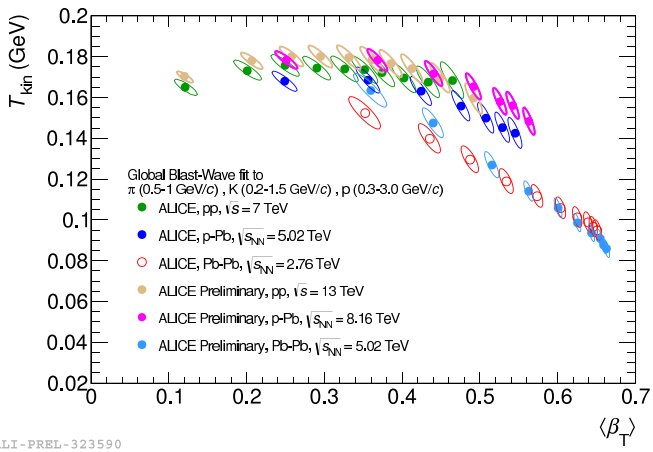

Fig. 3. The extracted kinetic freeze-out parameters using blast-wave model for various collision systems and energies.[4,5]

Figure 3 shows the extracted kinetic freeze-out parameters using blast-wave model for various collision systems and energies.[4,5] Blast-wave model is a hydrodynamical based model which assumes that the system is expanding radially with common radial flow velocity and undergoing common freeze-out. Simultaneous blast wave fits are performed on the transverse momentum spectra of pions, kaons and protons. The fit parameters, kinetic freeze-out temperature $T_{\rm kin}$ and average

transverse flow velocity $\langle\beta_T\rangle$ are plotted in Fig. 3 for various multiplicity classes. The multiplicity increases from left to right in the shown figure. It is observed that for heavy-ions A–A collisions, the $T_{\rm kin}$ decreases with multiplicity while $\langle\beta_T\rangle$ increases. There is no clear energy dependence of the freeze-out parameters. For small systems pp and p–Pb, the $T_{\rm kin}$ remains constant while $\langle\beta_T\rangle$ increases rapidly with multiplicity. At similar multiplicity values, the $\langle\beta_T\rangle$ is larger for small systems.

1.3. *Strangeness production*

Figure 4 shows the ratios of various particle yields to pion yield as a function of $\langle dN_{\rm ch}/d\eta\rangle_{|\eta|<0.5}$ for small systems pp and p–Pb, and for large systems A–A at various center-of-mass energies.[6–8] The ratios evolve smoothly as a function of multiplicity. There is no energy dependence neither the system-size dependence observed. This suggests that the particle production is driven by the charged particle multiplicity. It is observed that the ratios that involve strange particles increase with increasing multiplicity and saturate for heavy ions. Thus, enhancement in strange particle yields as a function of multiplicity. Strangeness enhancement has been predicted as a signature of QGP in heavy-ion collisions.[9] However, for small systems, we also observe the enhancement in strange particle yields. It is observed that the particle with more strangeness content exhibits larger enhancement. It is further noted that $\phi(1020)$ also exhibits strangeness enhancement through its "hidden strangeness" state and has total strangeness zero. It is observed that all particles with open strangeness undergo canonical suppression in small systems but $\phi(1020)$ does not.[10] The investigations based on model calculations are ongoing to understand this observation. Recent studies with $\phi(1020)$ meson using statistical

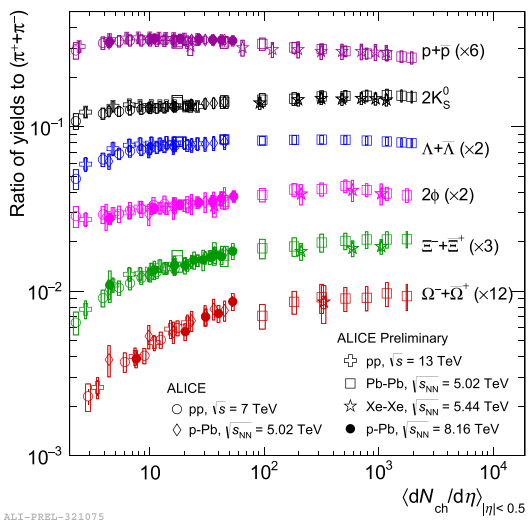

Fig. 4. Ratios of various particle yields to pion yield as a function of $\langle dN_{\rm ch}/d\eta\rangle_{|\eta|<0.5}$ for small systems pp and p–Pb, and for large systems A–A at various center-of-mass energies.[6–8]

thermal model in small systems and various ratios involving $\phi(1020)$ suggest that the "effective strangeness" of $\phi(1020)$ meson is 1–2 units.[3,11]

1.4. *Resonance production*

Figure 5 shows the ratios of particle yields involving short- and long-lived resonance particles as a function of $\langle dN_{\rm ch}/d\eta\rangle^{1/3}$ for various systems and energies.[3] Results are compared with EPOS model.[12] The resonance particles are reconstructed through their hadronic decay channel. The yields of resonances are affected by the medium through rescattering and regeneration processes. In re-scattering, the resonance particles that decay in the hadronic phase are not reconstructed due to the re-scattering of their decay daughters in the hadronic phase. There may be also regeneration of resonance particles due to the pseudo-elastic scattering. At the kinetic freeze-out stage, the resonance yields depend on various factors that include chemical freeze-out temperature, lifetime of hadronic phase, resonance particle lifetime and scattering cross-section of decay products. In Fig. 5, it is observed that yields of short-lived resonances such as $\rho(770)^0$, $K^*(892)^0$ and $\Lambda(1520)$ decrease as a function of multiplicity. The lifetimes of these particles are 1.3, 4.2 and 12.6 fm/c, respectively; hence, the decrease in their yields as a function of multiplicity is consistent with the fact that the yields might have been reduced due to re-scattering in the hadronic phase. The $\phi(1020)$ yield remains constant as a function of multiplicity. Since its lifetime is about 46.2 fm/c, this suggests that the $\phi(1020)$ meson decays after the hadronic phase and is not affected by rescattering or regeneration processes. It is also observed that all these ratios, too, do not depend on the system size and energy but only depend on the multiplicity. The EPOS model with UrQMD to describe the hadronic scattering effects describes the centrality dependence of ratios in heavy ions, while turning-off the UrQMD results in poorer description.

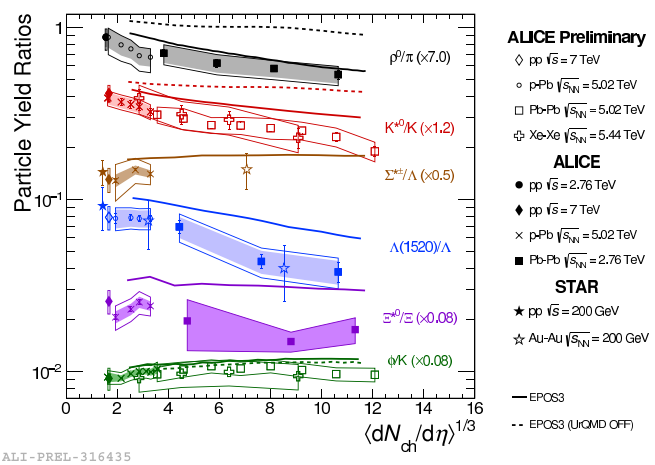

Fig. 5. Ratios of particle yields involving short- and long-lived resonance particles as a function of $\langle dN_{\rm ch}/d\eta\rangle^{1/3}$ for various systems and energies.[3] Results are compared with EPOS model.[12]

1.5. *Spin alignment*

In high-energy heavy-ion collisions with nonzero impact parameter, a large angular momentum ($\sim 10^5\hbar$) and magnetic field (10^{14} T) is expected to be created.[13,14] The deconfined state of quarks and gluons, called the Quark–Gluon Plasma (QGP), is also created in high-energy heavy-ion collisions. In the large angular momentum, the spin–orbit coupling of quantum chromodynamics (QCD) could lead to polarization of quarks and hence, net-polarization of spin 1 vector mesons along the direction of the angular momentum.[15,16] The spin alignment is studied through the angular distribution of decay daughters of the vector mesons with respect to the quantization axis. The quantization axis is perpendicular to the production plane of the vector meson, defined by the momentum of the vector meson and the beam direction, or normal to the reaction plane of the system, defined by impact parameter and the beam direction. The angular distribution is given by[17]

$$\frac{dN}{d\cos\theta^*} \propto [1 - \rho_{00} + \cos^2\theta^*(3\rho_{00} - 1)], \tag{1}$$

where the ρ_{00} is the zeroth element of the 3×3 spin-density matrix.[16] It is the probability of finding a vector meson in the spin state of zero out of the possible spin states of $-1, 0$ and 1. If there is no polarization, all spin states are expected to be equally probable leading to $\rho_{00} = 1/3$. Thus, any deviation of ρ_{00} value from the 1/3 would lead to nonuniform angular distribution preferring a spin state. Figure 6 shows the ρ_{00} values as a function of p_T for K^{*0} in pp collisions at $\sqrt{s} = 13$ TeV

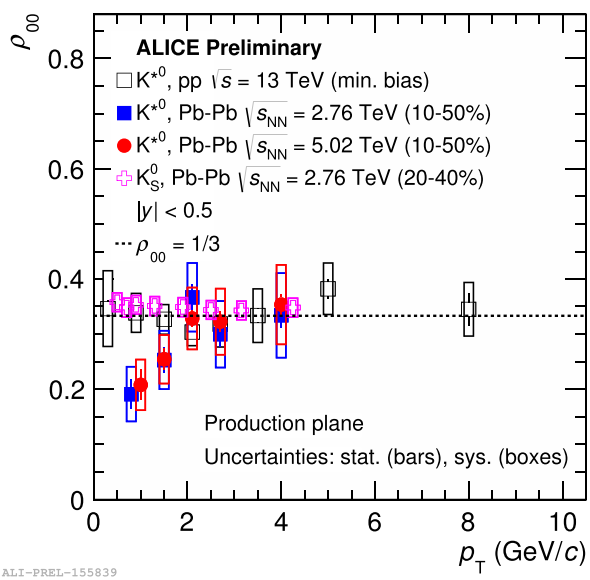

Fig. 6. The ρ_{00} values as a function of p_T for K^{*0} in pp collisions at $\sqrt{s} = 13$ TeV and Pb–Pb collisions $\sqrt{s_{\rm NN}} = 2.76$ and 5.02 TeV, and K^0_S in Pb–Pb collisions at $\sqrt{s_{\rm NN}} = 2.76$ TeV at mid-rapidity corresponding to the production plane.

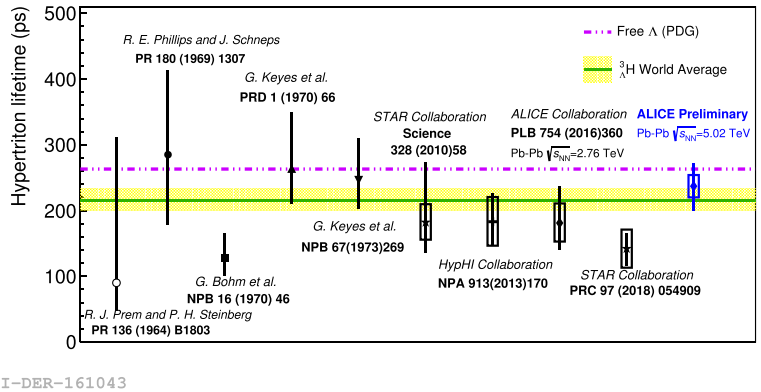

Fig. 7. Comparison of new hypertriton lifetime measurement results from ALICE at $\sqrt{s_{\rm NN}}$ = 5.02 TeV with previously published results.

and Pb–Pb collisions $\sqrt{s_{\rm NN}}$ = 2.76 and 5.02 TeV, and K^0_S in Pb–Pb collisions at $\sqrt{s_{\rm NN}}$ = 2.76 TeV at mid-rapidity corresponding to the production plane. It is observed that $\rho_{00} < 1/3$ for K^{*0} in Pb–Pb collisions at both energies. As expected, the $\rho_{00} = 1/3$ for K^{*0} (and ϕ meson) in pp collisions and for spin 0 state K^0_S. The results are consistent between event and production planes. The results suggest the first experimental observation of the spin–orbital interaction in heavy-ion collisions.

There have been a lot of efforts in estimating the lifetime of hypertriton ${}^3_\Lambda$H which is a bound state of proton, neutron and Λ and is the lightest hypernucleus. Very small Λ binding energy has led to the hypothesis that ${}^3_\Lambda$H is lower than free Λ. Figure 7 shows the comparison of new hypertriton lifetime measurement results from ALICE at $\sqrt{s_{\rm NN}}$ = 5.02 TeV with previously published results. The new results from ALICE are obtained from the full statistics data of Pb–Pb 5.02 TeV and the ${}^3_\Lambda$H are reconstructed through the two-body decay ${}^3_\Lambda\mathrm{H} \rightarrow {}^3\mathrm{He} + \pi$. The new ALICE results are consistent with both free Λ and world average.

1.6. *Summary*

In summary, we have presented a selected recent results on particle production from ALICE. The latest results on charged particle multiplicity confirm the violation of scaling of number of participant nucleons. The $\langle p_T \rangle$ of identified hadrons increases with multiplicity for both small and large systems. Mass ordering is observed for heavy-ions but seems to be broken for small systems. The kinetic freeze-out parameters are extracted for small and large systems. The extracted $\langle \beta_T \rangle$ increases with increasing multiplicity for all systems. At similar multiplicity values, the $\langle \beta_T \rangle$ is larger for small systems. The strangeness enhancement as a function of multiplicity is also observed for the first time in small systems. The short-lived resonance particles yield decreases with increasing multiplicity suggesting re-scattering effect in hadronic phase. The results on spin alignment studies suggest the first experimental

observation of spin–orbit coupling in heavy-ion collisions. The latest hypertriton lifetime measurement from ALICE is consistent with free Λ and the world average.

2. Study of Neutral Pion Mass in Presence of a Magnetic Field in the Linear Sigma Model Coupled to Quarks

Aritra Das and Najmul Haque

In the framework of linear sigma model coupled to quark, we calculate the neutral pion mass in the presence of an external arbitrary magnetic field at zero temperature. A nonmonotonic behavior of pion mass as a function of magnetic field is found. Existing weak-field result has also been reproduced.

2.1. *Introduction*

In heavy-ion collisions experiments, a very strong anisotropic magnetic field ($\sim 10^{19}$ Gauss) is generated in peripheral collisions perpendicular to the reaction plane due to the relative motion of the colliding ions.[18] In the interior of dense astrophysical objects like compact stars, magnetars[19] and also in the early universe, magnetic field is also involved. The effects of such magnetic fields on fundamental particles cannot be neglected and the detailed study of the effects on the elementary particles is essential at fundamental levels.

The linear sigma model (LSM) is one of the simplest model in pre-QCD era. It was originally proposed by Gell–Mann and Lévy to study phenomena such as pion–nucleon interaction. The addition of light quarks to the LSM Lagrangian density has given more flexibility to the existing model and it is called linear sigma model coupled to quark (LSMq).

In this proceedings contribution, we discuss the π^0-mass in the presence of an arbitrary magnetic field using LSMq.

2.2. *Linear sigma model coupled to quarks*

The Lagrangian of the model is written as

$$\mathcal{L} = \underbrace{\frac{1}{2}(\partial_\mu\sigma)^2 + \frac{1}{2}(\partial_\mu\boldsymbol{\pi})^2 + \frac{a^2}{2}(\sigma^2+\boldsymbol{\pi}^2) - \frac{\lambda}{4}(\sigma^2+\boldsymbol{\pi}^2)^2}_{\text{LSM part}}$$
$$+ \underbrace{i\bar{\psi}\gamma^\mu\partial_\mu\psi - g\bar{\psi}(\sigma + i\gamma_5\boldsymbol{\tau}\cdot\boldsymbol{\pi})\psi}_{\text{quark part}}. \tag{2}$$

The charged and neutral pion fields are usually defined as

$$\pi^\pm = \frac{1}{\sqrt{2}}(\pi^1 \pm i\pi^2), \quad \pi^0 = \pi^3. \tag{3}$$

σ is the sigma meson of LSM, and ψ is the u, d quark doublet as

$$\psi = \begin{pmatrix} u \\ d \end{pmatrix}, \tag{4}$$

$\boldsymbol{\tau} = (\tau^1, \tau^2, \tau^3)$ represents the Pauli spin matrices; a^2 is the mass parameter of the theory and we take $a^2 < 0$ in y unbroken state. Finally, λ is the coupling within σ-σ, π-π, σ-π; g represents the coupling between degrees of freedom (DOFs) of LSM with that of quarks.

When $a^2 > 0$, the symmetry is broken. After symmetry breaking, the Lagrangian takes the form

$$\begin{aligned} \boldsymbol{L} &= \bar{\psi}(i\gamma^\mu \partial_\mu - M_f)\psi + \frac{1}{2}(\partial_\mu \sigma)^2 + \frac{1}{2}(\partial_\mu \boldsymbol{\pi})^2 - \frac{1}{2}M_\sigma^2 \sigma^2 - \frac{1}{2}M_\pi^2 \boldsymbol{\pi}^2 \\ &\quad - g\bar{\psi}(\sigma + i\gamma_5 \boldsymbol{\tau} \cdot \boldsymbol{\pi})\psi - V(\sigma, \pi) - V_{\text{tree}}(v), \end{aligned} \tag{5}$$

with

$$V(\sigma, \pi) = \lambda v \sigma(\sigma^2 + \boldsymbol{\pi}^2) + \frac{\lambda}{4}(\sigma^2 + \boldsymbol{\pi}^2)^2, \tag{6}$$

$$V_{\text{tree}}(v) = -\frac{1}{2}a^2 v^2 + \frac{1}{4}\lambda v^4. \tag{7}$$

In unbroken state, the masses of quarks, sigma and three pions are given by

$$\begin{aligned} M_f &= gv, \\ M_\sigma^2 &= 3\lambda v^2 - a^2, \\ M_\pi^2 &= \lambda v^2 - a^2. \end{aligned} \tag{8}$$

To incorporate nonvanishing pion mass, we add a term $\boldsymbol{L}_{ESB} = \frac{1}{2}m_\pi^2 v(\sigma + v)$ to the Lagrangian density that is obtained after symmetry breaking and as a result, the masses are modified to

$$\begin{aligned} M_f(v_0') &= g\left(\frac{a^2 + m_\pi^2}{\lambda}\right)^{1/2}, \\ M_\sigma^2(v_0') &= 2a^2 + 3m_\pi^2, \\ M_\pi^2(v_0') &= m_\pi^2. \end{aligned} \tag{9}$$

2.3. *Background magnetic field*

We considered a homogeneous, time-independent background magnetic field in z-direction as $\vec{\boldsymbol{B}} = B\,\hat{\boldsymbol{z}}$ and the corresponding four-potential is $\boldsymbol{A}^\mu = \frac{B}{2}(0, -y, x, 0)$. The four-derivative ∂_μ is replaced by covariant four-derivative $D_\mu = \partial_\mu + i\boldsymbol{Q}\boldsymbol{A}^\mu$ for the charged DOFs (quarks and charged pions). Here $\boldsymbol{Q} = q_f$ for quark of flavor f and $\boldsymbol{Q} = e$ for $\pi^\pm$, respectively.

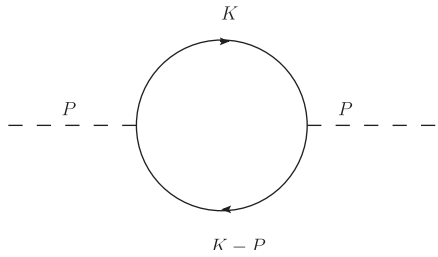

Fig. 8. Feynman diagram for the π^0 self-energy containing quark–antiquark loop.

2.4. *One-loop pion self-energy*

The neutral pion self-energy has the following four contributions:

$$\Pi(B,P) = \Pi_{f\overline{f}}(B,P) + \Pi_{\pi^\pm}(B) + \Pi_{\pi^0} + \Pi_\sigma. \tag{10}$$

The one-loop diagram for quark–antiquark contribution $\Pi_{f\overline{f}}(B,P)$ is depicted in Fig. 8, whereas that for charged pion contribution $\Pi_{\pi^\pm}(B)$ is depicted in Fig. 9. Note that for the last two terms [Π_{π^0} and Π_σ], there are no magnetic corrections as the particles in the loop are chargeless.

2.4.1. *Pion to quark–antiquark loop*

The expression for the pion self-energy with a quark loop in presence of magnetic field reads

$$\Pi_{f\bar{f}}(B,P) = i\sum_f g^2 \int \frac{d^4K}{(2\pi)^4} \mathrm{Tr}[\gamma_5 i S_f^B(K)\gamma_5 i S_f^B(K-P)], \tag{11}$$

where $S_f^B(K)$ is the quark propagator given as

$$\begin{aligned} iS_f^B(K) = &\int_0^\infty ds\, \exp\left[is\left\{K_\shortparallel^2 + K_\perp^2 \frac{\tan(|q_f B|s)}{|q_f B|s} - M_f^2 + i\epsilon\right\}\right] \\ &\times [(\not{K}_\shortparallel + M_f)\{1 + \mathrm{sgn}(q_f B)\tan(|q_f B|s)\gamma^1\gamma^2\} + \not{K}_\perp \sec^2(|q_f B|s)], \end{aligned} \tag{12}$$

where sgn is the sign-function. Now, to carry out the loop-momentum integration over K, we switch from Minkowski to Euclidean space-time by replacement $k^0 \to ik_E^0$ and also with the additional substitution $(s \to -is, t \to -it)$ as in Ref. 20. The subscript E represents the momentum components in Euclidean spacetime. Thus, after integration over the four-momentum, the expression for $\Pi_{f\bar{f}}$ can be written in terms of two proper-time integrations as

$$\begin{aligned} &\Pi_{f\bar{f}}(B,P) \\ &= \sum_f \frac{g^2}{4\pi^2} \int 0^\infty ds\, dt\, \frac{|q_f B|}{(s+t)} e^{-\{M_f^2(s+t) + (p_E^\shortparallel)^2 \frac{st}{s+t} + \frac{(p_E^\perp)^2}{|q_f B|} \frac{\sinh(|q_f B|s)\sinh(|q_f B|t)}{\sinh[|q_f B|(s+t)]}\}} \end{aligned}$$

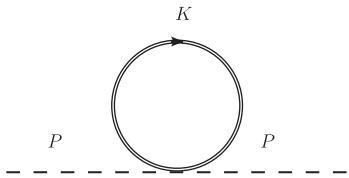

Fig. 9. Feynman diagram for one-loop charged pion contribution to the π^0 self-energy.

$$\times\left[\frac{1+M_f^2(s+t)-(p_E^{\shortparallel})^2\dfrac{st}{s+t}}{(s+t)\tanh(|q_fB|(s+t))}-\frac{|q_fB|}{\sinh^2(|q_fB|(s+t))}\right.$$
$$\left.\times\left(1-\frac{(p_E^{\perp})^2}{|q_fB|}\frac{\sinh(|q_fB|s)\sinh(|q_fB|t)}{\sinh[|q_fB|(s+t)]}\right)\right]. \tag{13}$$

2.4.2. *Charged pion loop*

The tadpole diagram, shown in Fig. 9, reads

$$\Pi_{\pi_\pm}(B)=\frac{\lambda}{4}\int\frac{d^4K}{(2\pi)^4}iD_B(K). \tag{14}$$

Charged pion propagator $D_B(K)$ in the presence of magnetic field is given by

$$iD_B(K)=\int_0^\infty\frac{ds}{\cos(|eB|s)}e^{i(K_{\shortparallel}^2+K_\perp^2\frac{\tan(|eB|s)}{|eB|s}-m_\pi^2)s}. \tag{15}$$

After momentum integration, we are left with the expression of $\Pi_{\pi_\pm}(B)$ given as

$$\Pi_{\pi_\pm}(B)=\frac{\lambda}{4}\frac{|eB|}{16\pi^2}\int_0^\infty\frac{ds}{s}\frac{e^{-sm_\pi^2}}{\sinh(|eB|s)}. \tag{16}$$

2.5. *Pion mass*

We need to solve the equation

$$p_0^2-|\boldsymbol{p}|^2-m_\pi^2-\mathrm{Re}[\Pi(B,P)]=0 \tag{17}$$

in the limit $\boldsymbol{p}\to 0$ and $p_0=M_\pi(B)$ to obtain modified pion mass $M_\pi(B)$. The self-energy of π^0 has four contributions out of which $\Pi_{f\bar{f}}(B,P)$ and $\Pi_{\pi_\pm}(B)$ will contribute to magnetic field correction as mentioned in Eq. (10). The total self-energy $\Pi(B,p_0,\boldsymbol{p}=\boldsymbol{0})$ can be written as

$$\Pi(B,p_0)=\sum_f\frac{g^2}{4\pi^2}\int_0^\infty ds\,dt\,\frac{|q_fB|}{(s+t)}e^{-(s+t)M_f^2-\frac{st}{s+t}(p_E^0)^2}$$
$$\times\left[\frac{1+M_f^2(s+t)-\dfrac{st}{s+t}(p_E^0)^2}{(s+t)\tanh(|q_fB|(s+t))}-\frac{|q_fB|}{\sinh^2(|q_fB|(s+t))}\right.$$

$$-\frac{M_f^2(s+t)-\frac{st}{s+t}(p_E^0)^2}{|q_fB|(s+t)^2}\Bigg]+\frac{\lambda}{4}\frac{1}{16\pi^2}\int_0^\infty ds\frac{e^{-sm_\pi^2}}{s}\left[\frac{|eB|}{\sinh(|eB|s)}-\frac{1}{s}\right]. \tag{18}$$

We can make a variable change from (s,t) to $(u,v$[20,21] in Eq. (18) as

$$s=\frac{1}{2}u(1-v),\quad t=\frac{1}{2}u(1+v). \tag{19}$$

This leads Eq. (17) to

$$M_\pi^2(B)=(v_0')^2\lambda-a^2-\sum_f\frac{g^2}{4\pi^2}\int_0^\infty du\int_{-1}^1 dv\,\frac{|q_fB|}{2}e^{-u\left[M_f^2-\frac{1}{4}(1-v^2)M_\pi^2(B)\right]}$$
$$\times\Bigg[\left\{\frac{1+uM_f^2+\frac{1}{4}u(1-v^2)M_\pi^2(B)}{u\tanh(|q_fB|u)}-\frac{|q_fB|}{\sinh^2(|q_fB|u)}\right\}$$
$$-\frac{M_f^2+\frac{1}{4}(1-v^2)M_\pi^2(B)}{u}\Bigg]-\frac{\lambda}{4}\frac{1}{16\pi^2}\int_0^\infty du\frac{e^{-u\,m_\pi^2}}{u}\left[\frac{|eB|}{\sinh(|eB|u)}-\frac{1}{u}\right]. \tag{20}$$

Equation (20) for the magnetic-field-dependent neutral pion mass is incomplete; one also needs to incorporate the one-loop magnetic-field correction to the boson self-coupling λ, the fermion coupling g and the minimum of the potential v_0'.

Now, the effective fermion mass becomes

$$M_{f,\text{eff}}=g_{\text{eff}}\,v_0^B, \tag{21}$$

where g_{eff} represents magnetic-field-dependent one-loop effective fermion vertex whereas v_0^B is the magnetic-field-dependent minimum of the potential after symmetry breaking.

Using Eq. (21) and replacing g_{eff} with the other effective quantities, Eq. (20) becomes

$$M_\pi^2(B)=(v_0^B)^2\lambda_{\text{eff}}-a^2-\sum_f\frac{1}{4\pi^2}\frac{1}{(v_0^B)^2}\int_0^\infty du\int_{-1}^1 dv$$
$$\times\frac{|q_fB|\,M_{f,\text{eff}}^2}{2}e^{-u\left[M_f^2-\frac{1}{4}(1-v^2)M_\pi^2(B)\right]}$$
$$\times\Bigg[\left\{\frac{1+uM_f^2+\frac{1}{4}u(1-v^2)M_\pi^2(B)}{u\tanh(|q_fB|u)}-\frac{|q_fB|}{\sinh^2(|q_fB|u)}\right\}$$

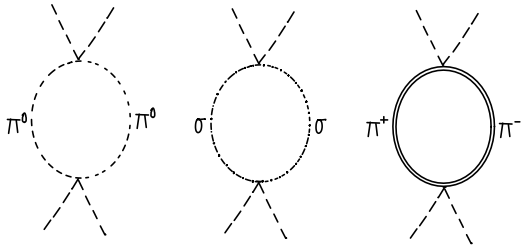

Fig. 10. One-loop corrections to the self-coupling λ. The dashed line denotes π^0, double line denotes $\pi^{\pm}$ and dashed-dotted line denotes σ-meson.

$$- \frac{M_f^2 + \frac{1}{4}(1-v^2)M_\pi^2(B)}{u}\Bigg]$$

$$- \frac{\lambda_{\text{eff}}}{4}\frac{1}{16\pi^2}\int_0^\infty du \frac{e^{-u\,m_\pi^2}}{u}\left[\frac{|eB|}{\sinh(|eB|u)} - \frac{1}{u}\right]. \tag{22}$$

The expression of effective self-coupling (λ_{eff}) can be obtained from the following vertex diagrams.

The effective self-coupling λ_{eff} to one-loop order is obtained from Fig. 10 as

$$\lambda_{\text{eff}} = \lambda + \frac{3\lambda^2}{8\pi^2}\int_{-1}^{1} dv \int_0^\infty du\, e^{-u\left\{m_\pi^2 + \frac{1}{4}(1-v^2)(p_E^0)^2\right\}} \times \left[\frac{|eB|}{2\sinh\left(|eB|u\right)} - \frac{1}{2u}\right]. \tag{23}$$

The other effective magnetic-field-dependent quantities, namely, v_0^B and $M_{f,\text{eff}}$, can be found in appendices of Ref. 22.

Solving Eq. (22) numerically, we get π^0 mass as shown in Fig. 11 in which a nonmonotonic behavior with magnetic field is observed.[22] It *decreases* with increasing magnetic field at weak magnetic field[23] but in large values of magnetic field it starts to increase.

2.6. *Conclusion and outlook*

In conclusion, we have studied effect of external magnetic field to the mass of the neutral pion mass under the framework of LSMq. The calculation is performed taking into account one-loop self-coupling of pions λ_{eff}, one-loop effective fermion mass $M_{f,\text{eff}}$ and one-loop effective minimum of the potential v_0^B. When the strength of magnetic field is increased, we get a nonmonotonic behavior. Our result also qualitatively agrees with LQCD studies as in Ref. 24 up to a moderate strength of the magnetic field. Looking to the future, the present calculation can be extended to the case of astrophysical objects where the baryon density and also the magnetic field are very high. Nevertheless, using LSMq model, we can qualitatively capture essential features that is obtained by much more involving and rigorous studies.

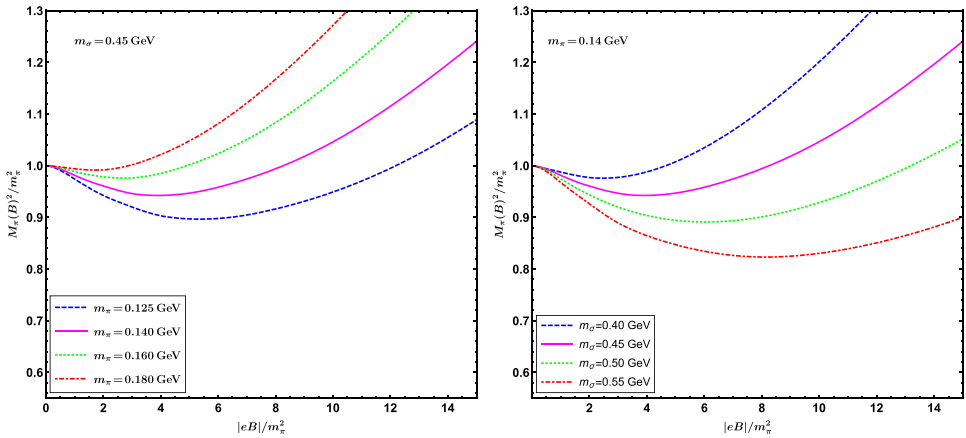

Fig. 11. Figure shows magnetic field dependence of neutral pion mass for a fixed $m_\sigma = 0.45$ GeV with $m_\pi = 0.125$, 0.140, 0.160, 0.180 GeV (left panel) and for a fixed $m_\pi = 0.14$ GeV with $m_\pi =$ 0.40, 0.45, 0.50, 0.55 GeV (right panel).

3. Flow Correlations as a Measure of Phase Transition

Ashutosh Dash and Victor Roy

In the present exploratory study, using a hydrodynamic model, we study the imprint of two different equation of state: one with crossover transition and other with first-order phase transition, on the flow correlations developed in the medium. We find that the normalized symmetric cummulants between different flow harmonics are sensitive to the nature of phase transition.

3.1. *Introduction*

It is well known that at low temperature (T) and baryon chemical potential (μ_B), nuclear matter is in a state of confined color neutral hadrons while at high temperature or high baryon chemical potential, nuclear matter is in a state of deconfined matter of quarks and gluons called the quark–gluon plasma (QGP). Nuclear matter at small baryon chemical potential and finite temperature is believed to undergo a crossover transition from the hadronic phase to the QGP phase and a first-order phase transition at relatively larger μ_B and the first-order phase transition line terminates at a critical point.[25]

This study aims to find a unique observable which connects QCD Equation of State (EoS) and the experimental data of heavy-ion collisions using hydrodynamical model. We find the linear/Pearson correlation (defined later) of initial geometric asymmetry of colliding nuclei to the corresponding flow coefficient (particularly the second-order flow coefficient v_2, Eq. (26)) is a unique observable which can differentiate between EoS with a first-order phase transition to that with a crossover transition irrespective of the initial condition used. It has been known that the event averaged v_2, and the eccentricity of the averaged initial state, ϵ_2, Eq. (25) is

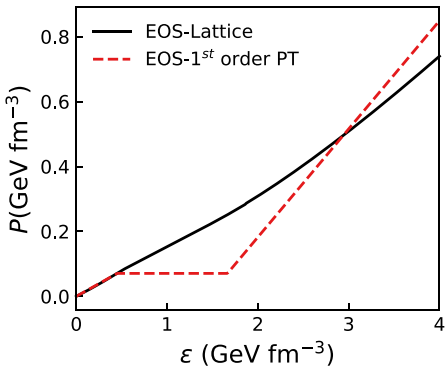

Fig. 12. (Color online) Equation of state with a cross-over transition (solid black line) and with first-order phase transition (dashed red line), at $\mu_B = 0\,\text{MeV}$.

approximately linearly correlated,[26] and the Pearson correlation is quite insensitive to the shear viscosity of the fluid and the initial condition used,[26] which makes it a robust observable to disentangle between the two different EoSs.

Results and discussion

In this work, we will be using two kinds of EoSs (shown in Fig. 12) [27]:

(i) A parameterized EoS (EoS Lattice) which has a cross-over transition between high temperature QGP phase obtained from lattice QCD and a hadron resonance gas below the crossover temperature.
(ii) An EoS (EoS first-order PT) connecting a noninteracting massless QGP gas at high temperature to a hadron resonance gas at low temperatures through a first-order phase transition. The bag constant B is a parameter adjusted to yield a critical temperature $T_c = 164\,\text{MeV}$.

Similarly, we consider here two initial conditions, where the initial energy density $\varepsilon(x, y)$ is obtained at initial time $\tau_0 = 0.6$ fm from the MC–Glauber and the Trento model using Gaussian smearing,

$$\varepsilon(x, y) = \kappa \sum_{i=1}^{N_{\text{WN}}} \exp\left(\frac{-(\vec{r} - \vec{r}_i)^2}{(2\sigma^2)}\right), \tag{24}$$

where $\vec{r}_i = (x_i, y_i)$ are the spatial coordinates of either wounded nucleons (initial condition ε_{WN}) or binary collisions (initial condition ε_{BC}). κ is a normalization constant fixed to provide the observed multiplicity of pions at $\sqrt{s_{\text{NN}}} = 62.4\,\text{GeV}$ and $\sigma = 0.7\,\text{fm}$ is the spatial scale of a wounded nucleon or a binary collision. The initial geometry/anisotropy of the overlap zone of two colliding nucleus is quantified

in terms of coefficients ϵ_n

$$\epsilon_n e^{\mathrm{in}\Phi_n} = -\frac{\int dxdyr^n e^{\mathrm{in}\phi}\varepsilon(x,y)}{\int dxdyr^n \varepsilon(x,y)}, \tag{25}$$

where ϕ is the azimuthal angle in position space and $\varepsilon(x,y)$ as defined in Eq. (24). The final azimuthal momentum anisotropy is characterized in terms of the coefficients v_n and is defined as Fourier expansion of the single particle azimuthal distribution

$$\frac{\mathrm{d}N}{\mathrm{d}\phi_p} \propto 1 + 2\sum_{n=1}^{\infty} v_n^{\mathrm{obs}} \cos n\left(\phi_p - \Psi_n^{\mathrm{obs}}\right), \tag{26}$$

where ϕ_p is the azimuthal angle in momentum space and Ψ_n^{obs} is the event plane angle. In order to quantify the linear correlation, we use Pearson's correlation coefficient which is defined as

$$c(x,y) = \left\langle \frac{(x - \langle x\rangle_{\mathrm{ev}})\,(y - \langle y\rangle_{\mathrm{ev}})}{\sigma_x \sigma_y} \right\rangle_{\mathrm{ev}}, \tag{27}$$

where σ_x and σ_y are the standard deviations of the quantities x and y. A value of $1(-1)$ implies that a linear (anti-linear) correlation between x and y. A value of 0 implies that there is no linear correlation between the variables.

For centrality 0–5% as shown in Fig. 13, using two different EoS, we found $\sim 15\%$ decrease in $c(\epsilon_2, v_2)$ for first-order phase transition compared to a crossover transition, which clearly indicates that $c(\epsilon_2, v_2)$ can be treated as a good signal of phase transition in the nuclear matter. However, the initial eccentricities ϵ_n are not accessible in real experiments (and are model dependent) which makes $c(v_n, v_m)$ more interesting. Nevertheless, instead of $c(v_n, v_m)$, a better experimental

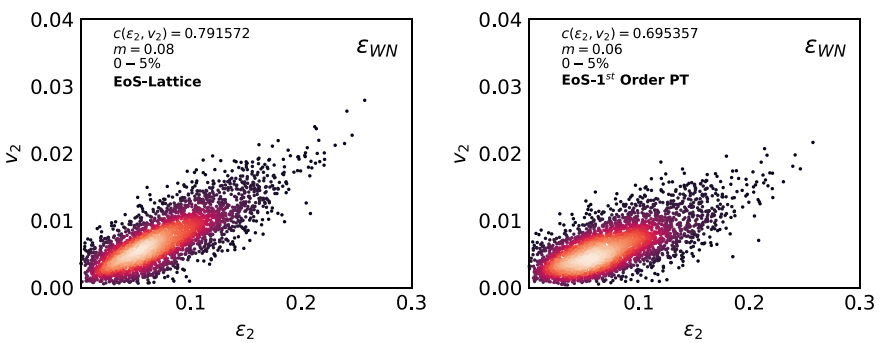

(a) (b)

Fig. 13. (a) Event-by-event distribution of v_2 versus ϵ_2 for 0–5% Au+Au collisions at $\sqrt{s_{\mathrm{NN}}} = 200$ GeV. (b) Same as left panel but for EoS with first-order phase transition.

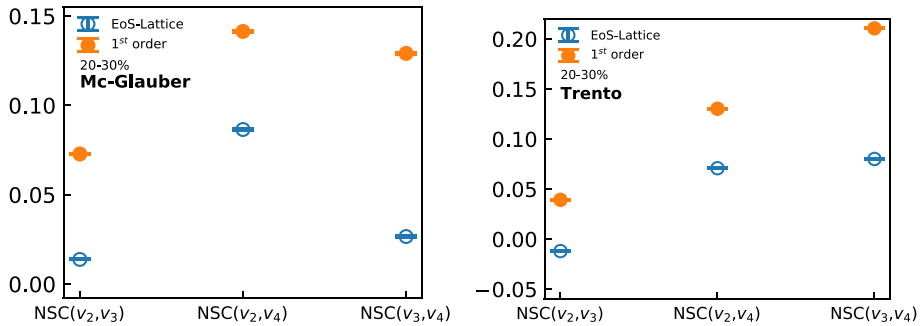

(a) (b)

Fig. 14. (Color online) (a) Normalized symmetric cummulants $NSC(m,n)$ for EoS–Lattice (solid red circles), and first-order phase transition (open blue circle) for 20–30% collision centrality. (b) Same as left panel but for Trento model. Error bars are statistical.

observable would rather be *normalized symmetric cummulants* (NSC) defined as

$$\mathrm{NSC}(m,n) = \frac{\langle v_m^2 v_n^2 \rangle - \langle v_m^2 \rangle \langle v_n^2 \rangle}{\langle v_m^2 \rangle \langle v_n^2 \rangle}. \tag{28}$$

The results of $\mathrm{NSC}(m,n)$ two different initial condition are shown in Fig. 14. We found in the mid central collisions always show higher values of $\mathrm{NSC}(m,n)$ for the EoS with first-order phase transition than crossover transition irrespective of the initial conditions. For example, we can calculate $\mathrm{NSC}(m,n)$ from available experimental data for various $\sqrt{s_{\mathrm{NN}}}$ and pinpoint the energies where $\mathrm{NSC}(m,n)$ shows an enhancement. These observations may be attributed to very different evolutionary dynamics of the system for the two different EoS, as the speed of sound becomes zero in first-order phase transition; hence, the linear/nonlinear coupling of ϵ_n–v_n and v_n–v_m is different in the two scenarios.

4. Color Dipole Distribution at Small Transverse Momentum

Mariyah Siddiqah, Nahid Vasim, Khatiza Banu, Raktim Abir, Trambak Bhattacharyya

We derive analytical results for unintegrated color dipole gluon distribution function at small transverse momentum in the form of a series of Bells polynomials. Interestingly, when resumming the series in leading log accuracy, the results show striking similarity with the Sudakov form factor when one identifies the coupling term with a constant that stems from the saddle point condition along the saturation line.

4.1. *Introduction*

Parton distribution function (PDF) encodes the nonperturbative structure of hadrons by providing information about the probability distribution of partons with

longitudinal momentum fraction x at some resolution scale Q^2 inside the hadron or nucleus. PDFs are the source of attraction for numerous dedicated experimental and theoretical efforts. PDFs are universal as they can be extracted from one experiment and used in some other scattering process at some other resolution scale. They play a central role in QCD predictions.

In order to know transverse momentum distribution of quarks and gluons inside the hadron/nucleus, it is necessary to consider some other distribution function. In this context, transverse momentum-dependent (TMD) parton distributions or unintegrated parton distribution functions (UPDFs) are objects of interest. They not only provide the information about the longitudinal momentum distributions but also give the information about the transverse momentum distributions of partons within the hadron/nucleus, thus providing a more detailed information on the internal structure of protons.[28]

TMDs have recently attracted a huge amount of interest and are fully investigated at the current and future facilities including JLAB 12 GeV upgrade, RHIC and planed electron–ion collider (EIC). Recently, unpolarized quark TMD from global data analysis has been extracted from the TMD factorized formulas derived from the semi-inclusive deep inelastic scattering and Drell–Yan and Z-boson production in proton–proton (pp) collisions.

The deep inelastic scattering experiments at HERA also provide intense indications that there exists a novel, yet unexplored, saturation regime in high energy limit of QCD which corresponds the small values of Bjorken-x. In this regime, the gluon cascade occupies all the phase space available to them to such an extent that the fusion of newly emitted gluons starts, leading to the gluon saturation. A dynamical scale gets generated due to this QCD self-regulation mechanism known as saturation scale Q_s.[29] At this scale, the gluon splitting balances gluon recombination.

In last few years, lot of efforts have been done in connecting TMDs and small-x saturation physics. Like PDFs, TMDs are also nonperturbative quantities and can be extracted from experiment using the same factorization approach but they are not universal as their operator definitions are process dependent. This process dependence of UPDFs is related to different choices of gauge links. The future and past gauge links correspond to final and initial state interactions, respectively. Depending on these gauge links, there are various UPDFs, but only two of them are universal and all other more complicated UPDFs can be seen as the convolution of these two gluon distribution functions.[30] The two different UPDFs are Weizsäcker–Williams (WW) gluon distribution and dipole gluon (DP) distribution function.[30–33]

4.2. *Gluon distributions*

Weizsäcker–Williams gluon distribution can be directly probed in the quark–antiquark jet correlation in deep inelastic scattering while the dipole gluon distribution can be probed in the direct photon-jet correlation in pA collisions. In the light-cone

gauge with the proper boundary conditions, the gauge links in the definition of WW gluon distribution disappear completely, indicating that WW gluon distribution can be interpreted as the genuine gluon density. On the other hand, the dipole gluon distribution does not have any such interpretation as the gauge link dependence always remains in its definition; thus, it is defined as the Fourier transform of the color dipoles.

The operator definition of Weizsäcker–Williams gluon distribution is

$$xG^{\mathrm{WW}}(x,k_\perp) = 2\int \frac{d\xi^- d^2\xi_\perp}{(2\pi)^3 P^+} e^{ixP^+\xi^- - ik_\perp.\xi_\perp} \times \langle P|\mathrm{Tr}[F^{+i}(\xi^-,\xi_\perp)\boldsymbol{U}^{[+]\dagger}\ F^{+i}(0,0)\ \boldsymbol{U}^{[+]}]|P\rangle, \tag{29}$$

whereas the operator definition of color dipole gluon distribution in the fundamental representation is

$$xG^{\mathrm{DP}}(x,k_\perp) = 2\int \frac{d\xi^- d^2\xi_\perp}{(2\pi)^3 P^+} e^{ixP^+\xi^- - ik_\perp.\xi_\perp} \times \langle P|\mathrm{Tr}[F^{+i}(\xi^-,\xi_\perp)\boldsymbol{U}^{[-]\dagger}\ F^{+i}(0,0)\boldsymbol{U}^{[+]}]|P\rangle. \tag{30}$$

In both the definitions, $F^{\mu\nu}$ is gluon field strength tensor $F_a^{\mu\nu}$ and the gauge links involved are

$$\boldsymbol{U}^{[+]} = U^n[0^-,0_\perp;\infty^-,0_\perp]U^t[\infty^-,0_\perp;\infty^-,\infty_\perp] \times U^t[\infty^-,\infty_\perp;\infty^-,\xi_\perp]U^n[\infty^-,\xi_\perp;\xi^-,\xi_\perp], \tag{31}$$

$$\boldsymbol{U}^{[-]} = U^n[0^-,0_\perp;-\infty^-,0_\perp]U^t[-\infty^-,0_\perp;-\infty^-,\infty_\perp] \times U^t[-\infty^-,\infty_\perp;-\infty^-,\xi_\perp]U^n[-\infty^-,\xi_\perp;\xi^-,\xi_\perp], \tag{32}$$

where the longitudinal (U^n) and transverse (U^t) gauge links are defined as

$$U^n[a^-,x_\perp;b^-,x_\perp] = \boldsymbol{P}\exp\left[ig\int_{a^-}^{b^-} dx^- A^+(0,x^-,x_\perp)\right],$$

$$U^t[x^-,a_\perp;x^-,b_\perp] = \boldsymbol{P}\exp\left[ig\int_{a_\perp}^{b_\perp} dx_\perp.A_\perp(0,x^-,x_\perp)\right].$$

Both these gluon distributions in the McLerran–Venugopalan model for a larger nucleus show a dramatic behavior as a function of $k_\perp$. For the larger values of $k_\perp$, both the WW gluon distribution and DP gluon distribution are proportional to $Q^2/k_\perp^2$ while at smaller values of $k_\perp$ WW gluon distribution is proportional to $\ln Q^2/k_\perp^2$ and DP gluon distribution is proportional to $k_\perp^2$.

4.3. *Results and discussions*

Recently, we have derived the analytical results of color dipole distribution function at small transverse momentum in series of Bells polynomial.[34] We consider

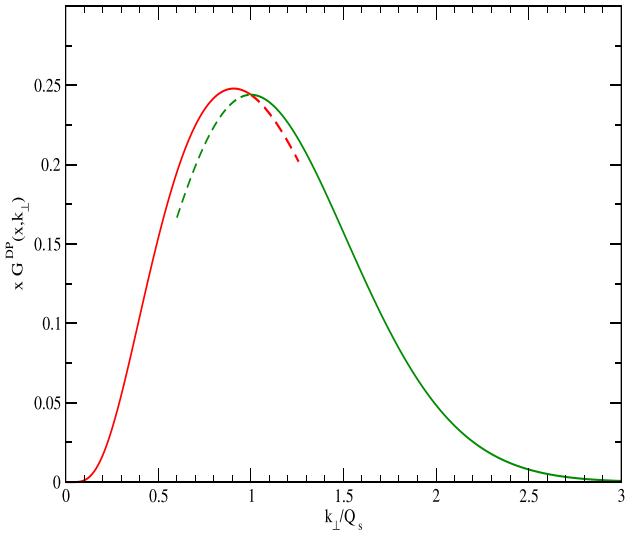

Fig. 15. (Color online) The unintegrated dipole gluon distribution $xG^{\rm DP}(r_\perp, Y)$ plotted as function of $\xi = k_\perp/Q_s(Y)$ for nucleus of typical radius ~ 7 fm at $\alpha_s \sim 0.1$. The tail of the green curve has been tweaked by scaling down to match at $\xi = 1$, about to follow power law fall.

the Levin–Tuchin (LT) solution[35,36] of the leading order Balitsky–Kovchegov equation in the black disc limit. Interestingly, when resuming the series in leading log accuracy, the results showing up striking similarity with the Sudakov form factor with role play of coupling are being done by a constant ($\tau = 0.2$) that stems from the saddle point condition along the saturation line. The key result of our study, unintegrated dipole gluon distribution at small transverse momentum, is as follows:

$$xG^{\rm DP}(x, k_\perp) \approx -\frac{S_\perp N_c \tau}{\pi^3 \alpha_s} \ln\left(\frac{k_\perp^2}{4Q_s^2}\right) \exp\left[-\tau \ln^2\left(\frac{k_\perp^2}{4Q_s^2}\right)\right].$$

The result (as shown in Fig. 15) indicates that at small transverse momentum, $xG^{\rm DP}(x, k_\perp)$, is not actually proportional to $k_\perp^2$ as previously anticipated; rather it is proportional to $\ln(k_\perp^2/4Q_s^2)$ times the double log soft factor.

5. Viscous Coefficients and Thermal Conductivity of a πKN Gas Mixture in the Medium

Pallavi Kalikotay, Nilanjan Chaudhuri, Snigdha Ghosh, Utsab Gangopadhyaya, Sourav Sarkar

The temperature and density dependence of the relaxation times, thermal conductivity, shear viscosity and bulk viscosity for a hot and dense gas consisting of pions, kaons and nucleons have been evaluated in the kinetic theory approach. The in-medium cross-sections for $\pi\pi$, πK and πN scatterings were obtained by using complete propagators for the exchanged ρ, σ, K^* and Δ excitations derived using thermal field theoretic techniques. Significant deviations have been observed

when compared with corresponding calculations using vacuum cross-sections usually employed in the literature. The value of the specific shear viscosity η/s is found to agree well with available estimates.

5.1. *Introduction*

The effects of dissipation on the dynamical evolution of matter produced in relativistic heavy-ion collisions have been a much discussed topic in recent times. Dissipative phenomena are generally studied by considering small deviations from equilibrium at the microscopic level. Transport coefficients such as shear and bulk viscosity and thermal conductivity are estimated considering the transport of momenta and heat among the constituents. Collisions among constituents are responsible for the transport of momenta, heat, etc. within the system and so the scattering cross-section is the principal dynamical input in transport equations where it appears in the collision integral. It is thus necessary that the relaxation time which quantifies the time scale of approach to equilibrium should be evaluated using in-medium scattering cross-sections in order to obtain a more realistic estimate of the transport coefficients. We have considered a hadron gas mixture consisting of Pions — the most abundant hadron gas produced in HIC, Kaons — the next abundant species and Nucleons — for introducing finite baryon density.

Using the kinetic theory approach, the expressions for thermal conductivity λ, shear viscosity η and bulk viscosity ζ are found to be

$$\lambda = \frac{1}{3T^2}\sum_{k=1}^{N}\int\frac{d^3p_k}{(2\pi)^3}\frac{g_k\tau_k}{E_k^2}p_k^2(p_k^\nu u_\nu - h_k)^2 f_k^{(0)}(1\pm f_k^{(0)}),$$

$$\eta = \frac{1}{15T}\sum_{k=1}^{N}\int\frac{d^3p_k}{(2\pi)^3}\frac{g_k\tau_k}{E_{p_k}^2}|\vec{p}_k|^4 f_k^{(0)}(1\pm f_k^{(0)}),$$

$$\zeta = \frac{1}{T}\sum_{k=1}^{N}\int\frac{d^3p_k}{(2\pi)^3}\frac{g_k\tau_k}{E_{p_k}^2}Q_k^2 f_k^{(0)}(1\pm f_k^{(0)}).$$

We will now start to discuss the results of our work. Figure 16 shows the elastic scattering cross-sections for $\pi\pi \to \pi\pi$, $\pi N \to \pi N$ and $\pi K \to \pi K$. The thermal medium has the effect of suppressing the cross-section at the resonance energy, which shows to be about 50–70% at $T = 160\,\text{MeV}$.

We have calculated all the results for three different sets of values of pion, nucleon and kaon chemical potential; the choice of these sets has been tabulated below.

Chemical potential	μ_π	μ_k	μ_N
Set 1	0	0	0
Set 2	50	100	200
Set 3	100	200	500

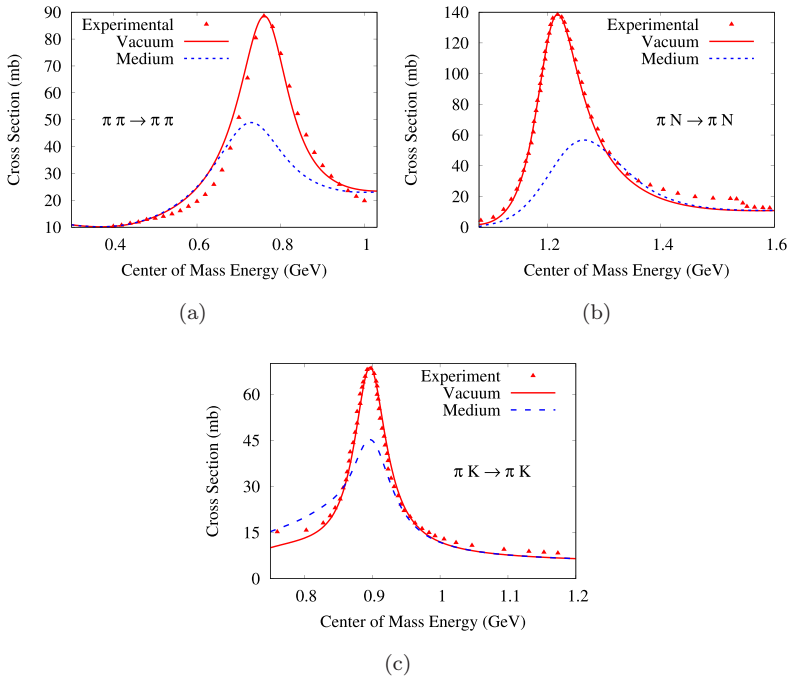

Fig. 16. The (a) $\pi\pi \to \pi\pi$, (b) $\pi N \to \pi N$ and (c) $\pi K \to \pi K$ elastic scattering cross-section as a function of center-of-mass energy compared among experiment, vacuum and medium corresponds to $T = 160\,\text{MeV}$ and $\mu_N = 200\,\text{MeV}$. Experimental data have been taken from Ref. 37.

Figure 17 shows the average relaxation times of π, K and N in πKN system as a function of temperature and baryon chemical potential. With the increase in temperature, number density of the system increases. As relaxation time is inversely related to number density of the system, hence relaxation time decreases with increase in temperature. Also with the increase of temperature, cross-section (in-medium cross-section) gets suppressed as shown in Fig. 16; hence, the magnitude of relaxation time increases. When baryonic density increases, the number of particle available for collision increases; hence, the system relaxes faster. This explains the decreasing relaxation time with increase in baryonic chemical potential.

5.2. *Thermal conductivity*

Plot of λ/T^2 as a function of temperature is shown for different sets of chemical potential in Fig. 18. The figure shows a decrease in its magnitude with the increase of temperature. The decrease in relaxation time with increase of temperature causes λ/T^2 to decrease with temperature. The medium effects increase the magnitude of λ/T^2. The increasing chemical potential causes λ/T^2 to decrease which is because of the increase in relaxation time brought down by the increase in density of nucleons and kaons.

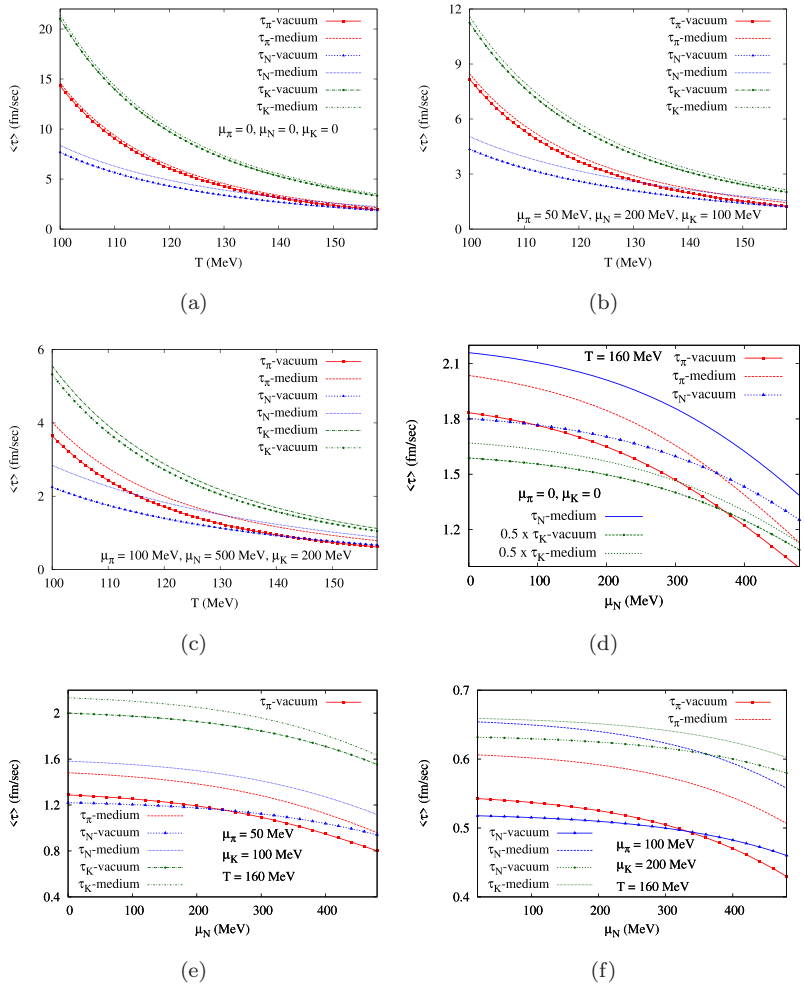

Fig. 17. Momentum averaged relaxation time of pions, nucleons and kaons in a pion–nucleon–kaon hadronic gas as function of temperature for (a) Set 1, (b) Set 2 and (c) Set 3 of chemical potentials of individual components and as function of baryonic density at $T = 160\,\mathrm{MeV}$ for (d) $\mu_\pi = 0$, $\mu_K = 0$, (e) $\mu_\pi = 50\,\mathrm{MeV}$, $\mu_K = 100\,\mathrm{MeV}$, (f) $\mu_\pi = 100\,\mathrm{MeV}$, $\mu_K = 200\,\mathrm{MeV}$.

Variation of η and η/s with temperature is shown in Fig. 19. Plots (a), (b) and (c) show increase in η with increase in temperature which is due to the increase in density. η/s decreases with increase in temperature due to the increase in entropy density with increase in temperature. Entropy density increases with increase in chemical potential, thus decreasing η/s. Here η/s respects the KSS bound. Due to the medium effects, both η and η/s increase in magnitude.

Figure 20 shows plot of ζ and ζ/s with temperature. The trend in the plots can be explained in similar lines done for η and η/s. The medium effects are visible here as well.

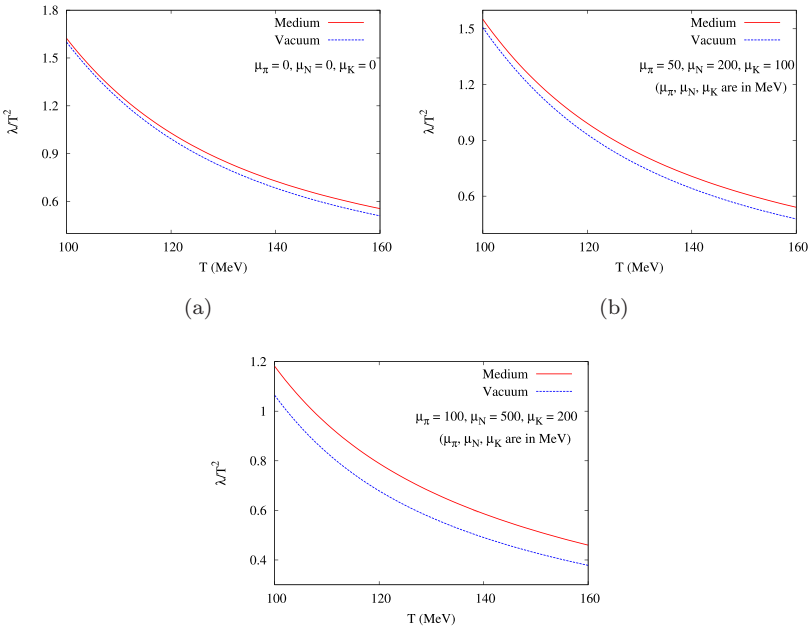

Fig. 18. λ/T^2 as a function of temperature for different sets of chemical potential of individual components. (a) Set 1, (b) Set 2 and (c) Set 3.

Variation of η/s and ζ/s with temperature and baryon chemical potential has been studied using both vacuum and in-medium cross-sections for μ_π =0 and μ_K =0 in Fig. 21. It is seen from the figure that η/s decreases with increasing μ_N whereas ζ/s increases with increase in μ_N.

Figure 22 shows the comparison of η/s from our work with other data in the literature. From the figure, we see that our results are well within the range. We also

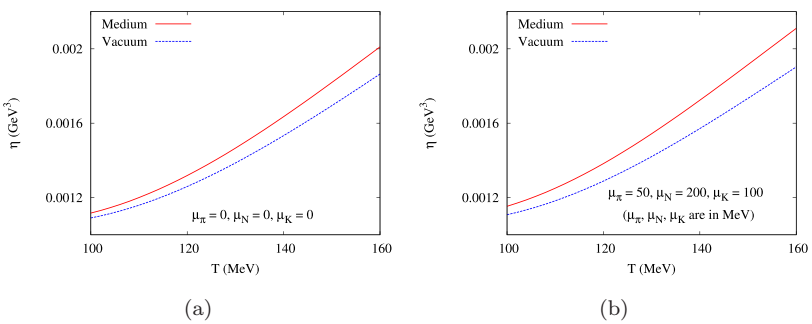

Fig. 19. Shear viscosity(η) and specific shear viscosity(η/s) versus temperature (T) for a pion–kaon–nucleon hadronic gas for different sets of chemical potential of individual components with and without including medium effects.

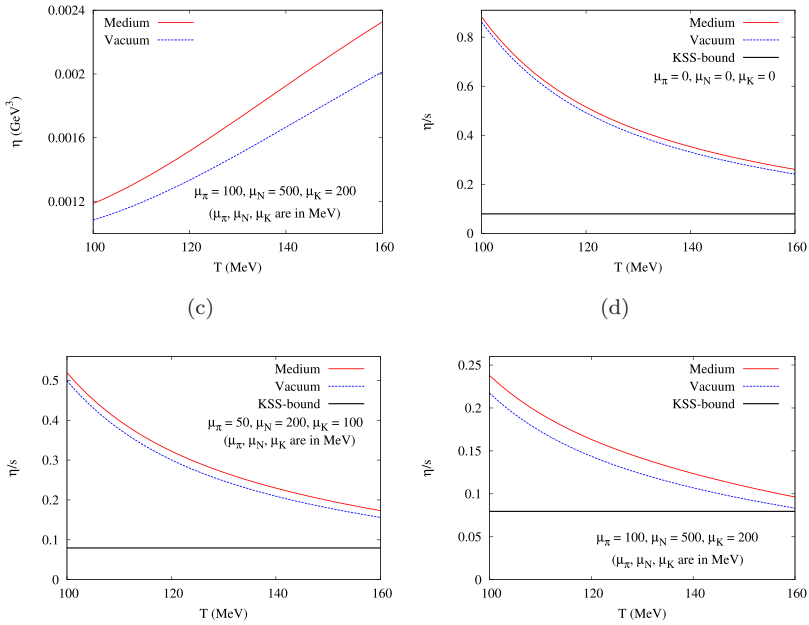

Fig. 19. (*Continued*)

found that η/s calculated for $\mu_\pi = 0$, $\mu_k = 0$ and $\mu_N = 0$ shows a good agreement with the data obtained by Ref. 38.

5.3. *Summary and discussions*

In this work, we have considered a hot and dense hadronic gas mixture consisting of pions, kaons and nucleons which are the most important components of the system produced during the later stages of heavy-ion collisions. We . endeavored to

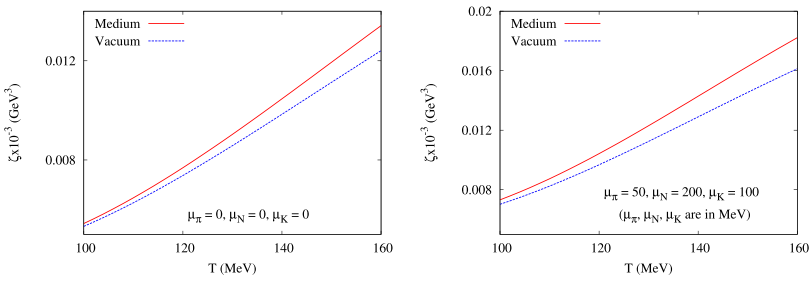

Fig. 20. Bulk viscosity(ζ) and its entropy ratio (ζ/s) versus temperature (T) for different sets of chemical potentials with and without including medium effects.

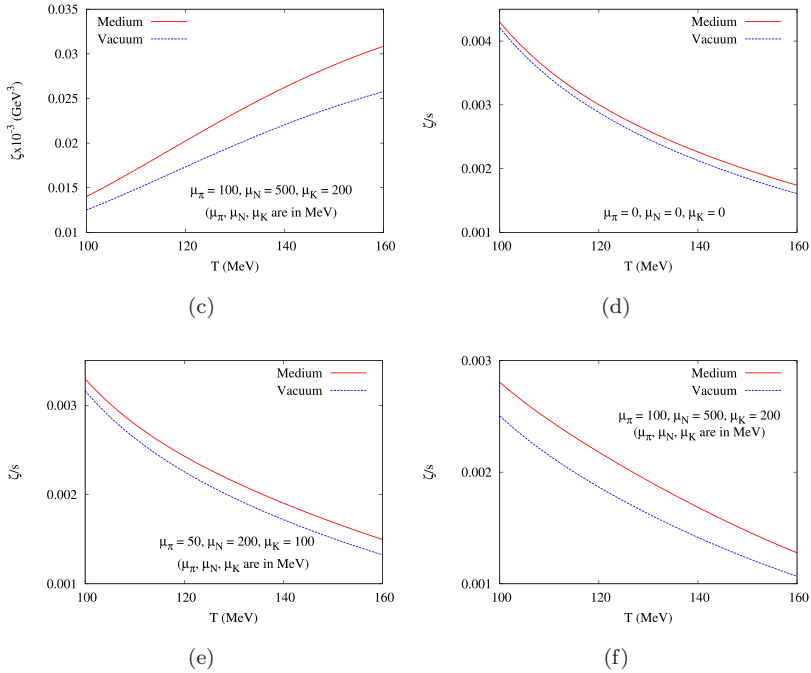

Fig. 20. (*Continued*)

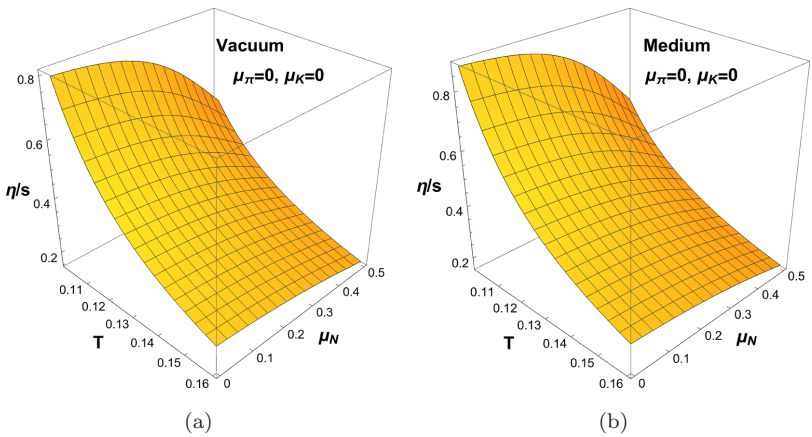

Fig. 21. Shear viscosity to entropy density ration (η/s) as a function of temperature and nucleon chemical potential at $\mu_\pi = \mu_K = 0$ with (a) vacuum and (b) in-medium cross-sections. Bulk viscosity to entropy density ration (ζ/s) as a function of temperature and nucleon chemical potential at $\mu_\pi = \mu_K = 0$ with (c) vacuum and (d) in-medium cross-sections.

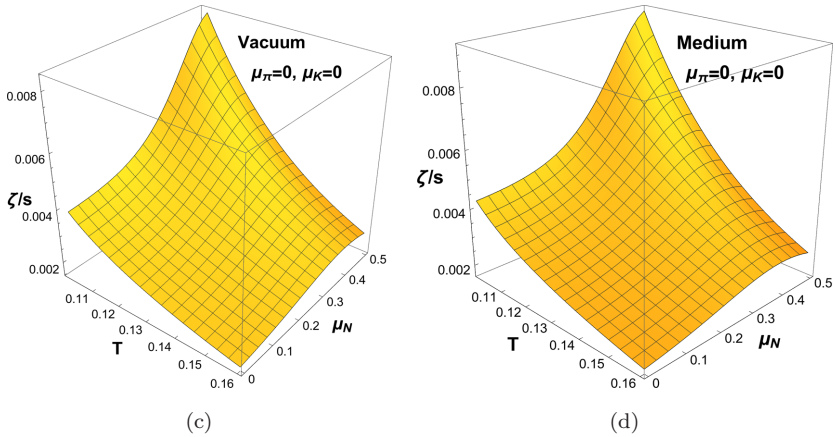

(c) (d)

Fig. 21. (*Continued*)

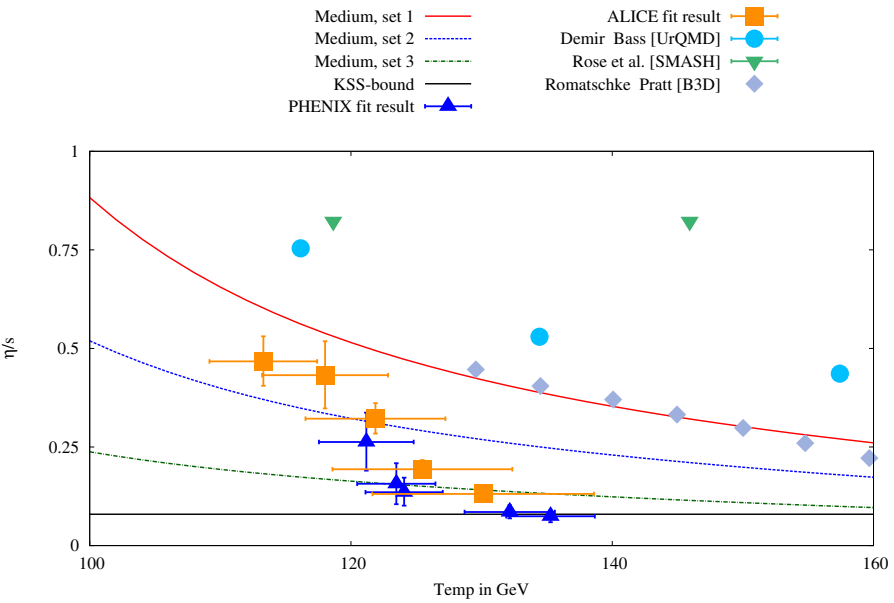

Fig. 22. The result obtained in this paper compared to various data of the specific shear viscosity η/s as a function of temperature available in the literature. A line of KSS bound has been drawn as a reference.

present a systematic study of the relaxation times, viscous coefficients and thermal conductivity for a system consisting only of pions, a system of pions and kaons and finally for a pion–kaon–nucleon system using the Boltzmann transport equation which has been linearized using the Enskog expansion. The key ingredient is the use of in-medium cross-sections which were obtained using one-loop corrected thermal propagators in the matrix elements for $\pi\pi$, πK and πN scattering. The suppression

of the in-medium cross-sections at finite temperature and density were reflected in the enhancement of relaxation times. This in turn results in a significant modification of the temperature dependence of the viscous coefficients. In particular, the value of η/s in the medium was found to be in good agreement with those found in the literature. These results may have significant effects on the evolution of the hot/dense hadronic matter produced in the later stages of heavy-ion collisions.

6. Higgs Propagation in Quark–Gluon Plasma

Sarthak Satapathy, Sabyasachi Ghosh, Santosh K. Das, Ralf Rapp, Nihar R. Sahoo

We are studying the properties of Higgs boson in the quark–gluon plasma (QGP). From the Higgs–quark interaction Lagrangian density, we calculate the Higgs decays into quark and anti-quark, which shows a dominant on-shell contribution in the bottom-quark channel. A large thermal suppression of the in-medium correction to the Higgs width is found in a straightforward thermal-field theory calculation. Alternatively, an operator product expansion has been adopted in a recent calculation In the present project, we aim at building a unified picture, including both decay and scattering diagrams, thereby also being able to include the impact of nonequilibrium effects. In the future, these interactions will be implemented into transport simulations to estimate the nuclear suppression factor of Higgs in QGP as formed in high-energy collisions of heavy nuclei.

6.1. *Introduction*

In the standard model, the Higgs boson, whose mass is measured at around 125 GeV,[39] has a very small decay width of about 4 MeV. With respect to typical tie scales in Quantum Chromodynamics (QCD) $\sim$ 1 fm/c, the mean lifetime of the Higgs (50 fm/c) is quite large, whereas the lifetime of the quark–gluon plasma (QGP) created in ultrarelativistic heavy-ion collisions is about 10 fm/c. This leads to a rather intriguing hierarchy of time scales for the interaction of the Higgs in the medium formed in heavy-ion collision. Indeed, it has been conjectured as a possibly relevant topic in the discussion of the Future Circular Collider (FCC), where these interactions might have nonnegligible consequences. Inspired by recent work on Higgs boson suppression in the QGP[40] and on its thermal width,[41] we are interested in finite-temperature calculation of the Higgs boson spectral function and its phenomenological connections.

In Sec. 6.2, we will first carry out a quantum field-theoretical calculation of Higgs boson decay width through quark–anti-quark channels and confirm that a straightforward application gives almost no width enhancement relative to the vacuum. We will then discuss an alternative calculation of the thermal width correction calculation through the operator product expansion (OPE) methodology as well as a study of thermal scattering and suppression of Higgs in QGP, following along the lines of Ref. 41. In Sec. 6.3, we give a brief summary an indicate a future strategy of our ongoing work.

6.2. *Framework and discussion*

The particles in the standard model acquire mass through the Higgs mechanism. The carriers of the weak interactions are the $W^{\pm}$and Z^0 bosons, which is a $SU(2)$ gauge theory, and the electromagnetic interactions are carried by the photon (γ), which is a $U(1)$ gauge theory. Electromagnetic and weak interactions are unified within a $SU(2)_L \times U(1)_Y$ symmetry to form the Electroweak theory. In addition to this, the standard model contains the strong interactions mediated by gluons which are based on a $SU(3)$ gauge theory, QCD. Thus, the complete gauge group of the standard model is $SU(3) \times SU(2) \times U(1)$.

Spontaneous symmetry breaking is the essence governing Higgs mechanism which is triggered by a Mexican-hat potential for a complex scalar field theory as shown in Fig. 23. The Electroweak Lagrangian is constructed to allow for the Higgs mechanism giving rise to interaction terms fermions and bosons with a Higgs field.

Here we are interested in Higgs boson's coupling to particles in the QCD sector. The interaction Lagrangian term for Higgs decaying to quark and anti-quark is given by

$$\mathcal{L}_{Hq\bar{q}} = -\frac{m_q H \psi_q \bar{\psi}_q}{v}, \tag{33}$$

where $v = 246\,\text{GeV}$ is the vacuum expectation value of the Higgs field and m_q is the bare mass of the various quarks. To calculate Higgs decay width in vacuum, we evaluate the quark–anti-quark loop diagram of Higgs boson, given by

$$\Pi(q) = \int \frac{d^4q}{(2\pi)^4} L(k,q) D_k D_{k-q}, \tag{34}$$

where

$$L(k,q) = \left(\frac{-im_q}{v}\right)^2 Tr[(\not{k}+m)(\not{k}-\not{q}+m)] = -\frac{4m_q^2}{v^2}\left[k^2 - \frac{q^2}{2} + m^2\right], \tag{35}$$

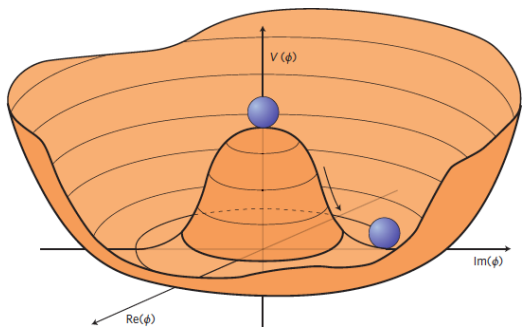

Fig. 23. A sketch of Mexican-hat type potential, $V(\phi)$, having degenerate vacua, one of which is chosen during the spontaneous symmetry breaking in the Higgs mechanism.

and D_k , D_{k-q} are the scalar terms of the fermionic propagator given by

$$D_{k,k-q} = \frac{1}{(k,k-q)^2 - m_q^2}. \tag{36}$$

The decay width Γ_H can be obtained from imaginary part of the vacuum self-energy,

$$\Gamma(q) = \frac{\mathrm{Im}\Pi(\mathrm{q})}{q} = N_c \frac{m_q^2 q}{8\pi v^2}\left[1 - \frac{4m_q^2}{q^2}\right]^{3/2}, \tag{37}$$

where q is the 4-momentum of Higgs boson and N_c is color degeneracy factor.

The off-mass shell distributions of the Higgs boson decay widths $\Gamma_{b\bar{b}}$ and $\Gamma_{c\bar{c}}$ for charm- and bottom-quark decay channels are shown in Fig. 24, where their unitarity cut thresholds of $2m_c$ and $2m_b$ can be seen very distinctly. The dotted vertical line indicates the pole mass of the Higgs, which marks the on-shell values of $\Gamma_{b\bar{b}}$ and $\Gamma_{c\bar{c}}$, where former is the dominant contribution with a value of approximately 4 MeV. The light-quark channels are rather suppressed, by factors of $\frac{m_{u,d,s}^2}{m_b^2}$; the quark masses are the bare ones, with $m_{u,d} \simeq 5\,\mathrm{MeV}$, much smaller than heavy quark masses $m_{c,b}$ (recall that while the phase space is ultraelativistic in all cases, the respective coupling constants are proportional to the masses).

The thermal corrections to the decay of Higgs boson are given by the expression of the finite-temperatures self-energies,

$$\mathrm{Im}\left(\Pi^T\right) = \frac{m_q^2 q^2}{8\pi v^2 |\overrightarrow{q}|}\left[1 - \frac{4m_q^2}{q^2}\right]\left(\frac{1}{\beta}\ln\left|\frac{e^{\beta(\omega_k^+ - \mu)} - 1}{e^{\beta(\omega_k^- - \mu)} - 1}\right| + \frac{1}{\beta}\ln\left|\frac{e^{\beta(\omega_k^- - \mu)} + 1}{e^{\beta(\omega_k^- + \mu)} + 1}\right|\right), \tag{38}$$

where $\omega_k^{\pm} = \frac{1}{2}[q_0 \pm |\overrightarrow{q}|]$. These corrections are very small compared to the vacuum decay width because of the v^2 term figures in the denominator and the large M_H value figures in the logarithmic term in Eq. (38) and thus contributes rather little.

A nontrivial evaluation of the decay of Higgs to quarks and gluons in a hot QCD medium has recently been in Ref. 41 using an alternative technique — the

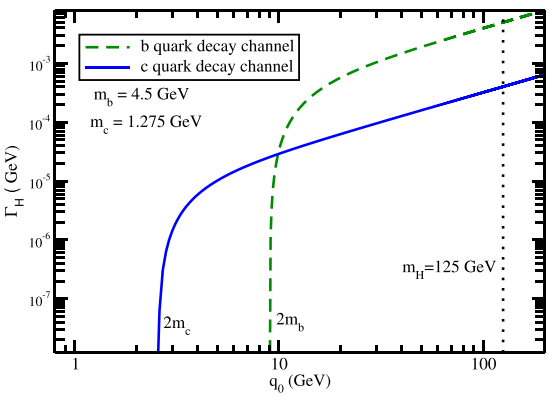

Fig. 24. Off-mass shell distribution of vacuum widths for the $H \to b\bar{b}$ and $H \to c\bar{c}$ decay channels.

operator product expansion (OPE). Pioneering work in Ref. 42 has utilized the use OPE technique[43,44] to study the asymptotic behavior of different spectral functions and stress–energy tensors at finite temperature in the high-energy time-like region, $\omega >> T$, and their thermal corrections in Euclidean Yang–Mills theory. The Euclidean current–current correlator relates the spectral function with the Euclidean Green's function. Thermal corrections to the decay rate depend on thermal corrections to the spectral function.[42,45,46] Reference[41] makes use of the technique of Ref. 42 for obtaining a pertinent result for the Higgs boson. The Euclidean OPE coefficients are calculated by taking the Euclidean current–current correlator given by

$$G_E(q) = \int d^4x e^{-iqx} \langle J(x)J(0)\rangle, \tag{39}$$

evaluated at $q = (0, 0, 0, q_E)$.

The dispersion relation which relates Euclidean Green's function to the spectral function is[41,42]

$$G_E(q_E) = P(q_E) + \int_{-\infty}^{+\infty} \frac{d\omega}{(2\pi)(\omega - iq_E)} \rho_J(\omega), \tag{40}$$

whose bulk channel is useful for calculating decay widths, as has been done for the problem at hand in Ref. 41. The asymptotic expansion of $\rho_J(K)$ for large time-like K has then been obtained from matching term-by-term to the OPE of $G_E(q_E)$ for large space-like q_E.

Leading thermal corrections to spectral functions in QCD are proportional to T^4, which is a standard result in perturbative QCD. To apply OPE, one has to then distinguish the kinematic regions based on the validity of the OPE technique. A detailed analysis of OPE applied to the Higgs in the QGP has been carried out in Ref. 41, and the thermal correction to the decay width of Higgs to quark and anti-quark pairs (in particular bottom) has been obtained as

$$\delta\Gamma_{H\to b\bar{b}} = -\Gamma^{\rm vac}_{H\to b\bar{b}}\, \alpha_s \frac{T^4}{m_H^4} \frac{128\pi^3}{135}, \tag{41}$$

where $\Gamma^{\rm vac}_{H\to b\bar{b}} \approx N_c \frac{m_q^2 m_H}{8\pi v^2}$ is the on-shell vacuum decay width of Higgs the boson to bottom quarks by ignoring the multiplicative factor of $(1 - \frac{m_q^2}{m_H^2})^{3/2}$. For all partial decay widths into $q\overline{q}$ pairs, the thermal correction is of $\mathcal{O}(\alpha_s \frac{T^4}{m_H^4})$ to the vacuum decay width.

In another recent work[40] on the interactions of Higgs in quark–gluon matter, the scattering amplitude is employed for estimating the Higgs adsorption in QGP. Here, the cross-sections for Higgs-parton scattering have been analyzed and reproduced by a power-law fit of the form

$$\sigma_{Hgq}(\sqrt{s}) = K.A[\mu b]((\sqrt(s) - m_H)/[GeV])^{-n}, \tag{42}$$

with an amplitude $A = 2\mu b$ and $n = 3$. They have taken a $K = 3$ factor to map higher order corrections in Higgs-parton scattering. This has been obtained

through N^3LO/LO ratio of the $gg \to H+X$ production cross-section, featuring the same diagrams. They have made use of thermal mass prescriptions for partons in medium giving finite Higgs-parton scattering ratio of the order of μb. By using this in-medium cross-section, they obtain a nonnegligible suppression of Higgs in QGP. However, when also including virtual corrections, they find a large cancellation which results in an essentially negligible final result compatible with that of Ref. 41.

6.3. *Summary and future plan*

In this article, we have first given a brief survey of the Higgs boson connection to the quark–gluon plasma. Starting with the spontaneous symmetry breaking mechanism of the standard-model Mexican-hat potential within the QCD sector, our interest has been focused on the Higgs coupling to quarks as described by the interaction Lagrangian density. After illustrating the off-shell mass distribution function of Higgs boson going to quark and anti-quark decay channels in vacuum, we have addressed its thermal-field theoretical correction, which turns out to be very small. This is in line with previous works by Ghiglieri and Wiedemann adopting an operator product expansion methodology, and by d'Enterria and Loizides using a fitted cross-section including virtual corrections. Based on these existing investigations, we have attempted a unified description, which includes both decay and scattering both diagrams, as a work in progress. Realizing the suppressed thermal correction, we also plan to develop a nonequilibrium spectral function of Higgs from QGP via an intermediate nonequilibrium mechanism of diffusing heavy quarks, whose number in heavy-ion collisions is usually much larger than the equilibrium value. The rough sketch would be to obtain nonequilibrium Higgs properties from nonequilibrium heavy quarks in an equilibrium light-quark and gluon bath. After developing the spectral form, our next step is to implement it into a transport approach for revisiting the nuclear suppression factor of the Higgs in heavy-ion collisions.

7. Anisotropic Pressure of Deconfined Hot QCD Matter in Presence of Strong Magnetic Field within One-Loop Approximation

Ritesh Ghosh, Bithika Karmakar, Aritra Bandyopadhyay, Najmul Haque, Munshi G. Mustafa

We constructed general structure of fermion self-energy in strong magnetic field and obtained dispersion relation by calculating one-loop fermion self-energy. We obtained analytic expression for anisotropic pressure and magnetization of a strongly magnetized hot QCD matter created in heavy-ion collisions considering the general structure of the two-point functions of both quarks and gluons (within one-loop approximation) using hard thermal loop approximation for the heat bath. The obtained anisotropic pressure may be useful for a magnetohydrodynamics description of a hot and dense deconfined QCD matter produced in heavy-ion collisions.

7.1. *Introduction*

A new hot and dense state of quarks and gluons is created in relativistic heavy-ion collisions(HIC) in RHIC at BNL and LHC at CERN in recent times. This new state known as QGP can be explained by non-Abelian gauge theory of QCD which is the theory of strong interaction of quarks and gluons. This theory explains a phase transition from confined state in low energy to deconfined state of quarks and gluons(QGP) in high energy. It is believed that such QGP state was created in early universe after few microseconds of big bang and exists in core of neutron star where matter density is much higher than normal matter density. Upcoming experiments are to be performed in FAIR at GSI and NICA at Dubna to explore more. In recent years, study of noncentral collisions says that high magnetic field can be generated in direction perpendicular to reaction plane due to the spectator particles.[47] Strength of magnetic field decreases very fast from (30–10) m_π^2 to (1–2) m_π^2 in about (4–5) fm/c.[48] So one can work in two different regions: one is strong magnetic field limit ($q_f B > T^2$) and other is weak magnetic field limit ($q_f B < T^2$).

As EoS has phenomenological importance for studying hot and dense QCD matter, we computed the EoS within the strong limit. We work in lowest Landau level (LLL) with scale hierarchy ($q_f B > T^2 > m_f^2$) as in strong field limit magnetic field pushes the higher Landau level (HLL) to infinity compared to LLL.[49]

7.2. *Quarks in strong magnetic field*

7.2.1. *General structure*

Presence of heat bath breaks the Lorentz (boost) invariance, whereas the presence of magnetic field breaks the rotational invariance of the system. So one needs to construct a manifestly covariant structure of the self-energy. We have external fermion momentum P^μ. We have worked in rest frame of heat bath $u^\mu = (1, 0, 0, 0)$. As we are considering noncentral HIC, we are taking background magnetic field in z-direction $n_\mu = \frac{1}{2B}\epsilon_{\mu\nu\rho\lambda} u^\nu F^{\rho\lambda} = (0, 0, 0, 1)$, where $F^{\mu\nu}$ is the electromagnetic field tensor.

The fermion self-energy is a 4×4 matrix as well as Lorentz scalar. General structure should be made of basis matrices $\{\mathbf{I}, \gamma_\mu, \gamma_\mathbf{5}, \gamma_\mu\gamma_\mathbf{5}, \sigma_{\mu\nu}\}$. As we are working in strong magnetic field limit ($q_f B \gg T^2$), we confine ourselves in LLL where transverse component of fermion momentum $P_\perp = 0$. General structure of fermion self-energy in LLL can be written as[50]

$$\Sigma(p_0, p_3) = a\not{u} + b\not{n} + c\gamma_5\not{u} + d\gamma_5\not{n}, \tag{43}$$

where

$$a = \frac{1}{4}\,\mathrm{Tr}[\Sigma\not{u}], \quad b = -\frac{1}{4}\,\mathrm{Tr}[\Sigma\not{n}],$$
$$c = \frac{1}{4}\,\mathrm{Tr}[\gamma_5\Sigma\not{u}] \quad \text{and} \quad d = -\frac{1}{4}\,\mathrm{Tr}[\gamma_5\Sigma\not{n}].$$

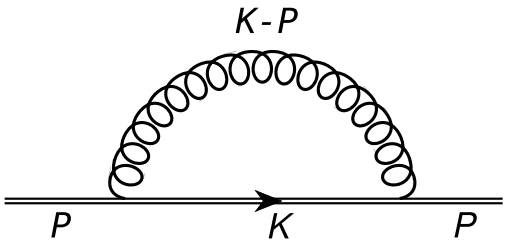

Fig. 25. Self-energy diagram for a quark in a strong magnetic field approximation. The double line indicates the modified quark propagator in presence of strong magnetic field.

7.2.2. *One-loop quark self energy in strong field*

One-loop quark self-energy in Feynman gauge can be written from Fig. 25 as

$$\Sigma(P) = -ig^2 C_F \int \frac{d^4K}{(2\pi)^4} \gamma_\mu S(K) \gamma^\mu \Delta(K-P), \tag{44}$$

where the unmodified gluonic propagator is given as

$$\Delta(K-P) = \frac{1}{(K-P)_{\shortparallel}^2 - (K-P)_{\perp}^2} \tag{45}$$

and modified fermion propagator in LLL is given by

$$iS(K) = ie^{-k_\perp^2/q_f B} \frac{\not{K}_{\shortparallel} + m_f}{K_{\shortparallel}^2 - m_f^2}(1 - i\gamma_1\gamma_2). \tag{46}$$

Here we used $(K-P)_{\shortparallel}^2 = (k_0 - p_0)^2 - (k_3 - p_3)^2$ and $(K-P)_{\perp}^2 = (k_1 - p_1)^2 + (k_2 - p_2)^2$.

7.2.3. *Effective propagator and dispersion relation*

In LLL, the effective fermion propagator can be written as

$$S_{\text{eff}}(P_{\shortparallel}) = \frac{1}{\not{P}_{\shortparallel} + \Sigma}. \tag{47}$$

Using chiral projectors effective propagator can also be written as

$$S_{\text{eff}}(P_{\shortparallel}) = \mathsf{P}_R \frac{\not{R}}{R^2} \mathsf{P}_L + \mathsf{P}_L \frac{\not{L}}{L^2} \mathsf{P}_R, \tag{48}$$

where $\mathsf{P}_R = \frac{1}{2}(1+\gamma_5)$ and $\mathsf{P}_L = \frac{1}{2}(1-\gamma_5)$. We have

$$L^2 = (p_0 + (a+c))^2 - (p_3 - (b+d))^2, \tag{49}$$

$$R^2 = (p_0 + (a-c))^2 - (p_3 - (b-d))^2. \tag{50}$$

We find the expression of form factors from one-loop fermion self-energy and then obtain dispersion curves by solving $R^2 = 0$ and $L^2 = 0$ from Eq. (48). There are four modes, two comes from $L^2 = 0$ and two from $R^2 = 0$. In LLL, only two modes are allowed:[51] one L-mode with energy ω_L of a positively charged fermion

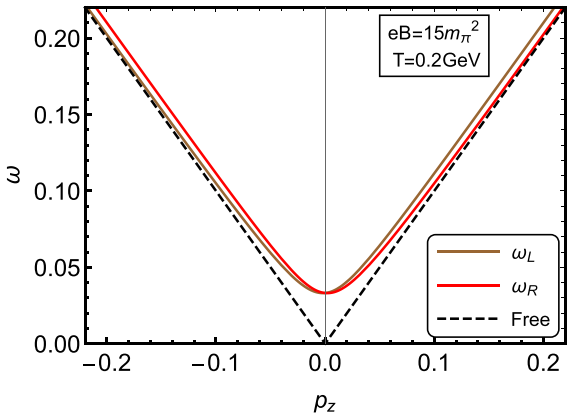

Fig. 26. Dispersion relation of fermion in presence of strong magnetic field.

having spin up and another one from R-mode with energy ω_R of a negatively charged fermion having spin down. These two modes are plotted in Fig. 26. At high p_z, both the mode of dispersion resembles free dispersion mode. We also note that the reflection symmetry is broken in the presence of magnetic field.[51]

7.3. *Gluon and quark free-energy in a strongly magnetized hot medium*

General structure of gauge boson two-point function in strong magnetic field and one-loop dispersion relation is obtained in paper.[52] We have calculated hard and soft contribution (considering soft gluon momentum $P \sim gT$) of gluon free energy up to $O(g^4)$ in hard thermal loop approximation. We also calculate quark free-energy up to $O(g^4)$. Analytic expressions of quark and gluon free-energy can be found in Ref. 50.

7.4. *Anisotropic pressure in strong magnetic field*

So total one-loop free energy of deconfined QCD matter can be written as

$$F = F_q + F_g^{\text{hard}} + F_g^{\text{soft}} + F_0 + \Delta E_T^0 + \Delta E_T^B, \tag{51}$$

where F_q, F_g^{hard}, F_g^{soft} are quark free-energy and hard and soft contribution of gluon self-energy, respectively. From one-loop calculation, different kinds of divergences arise of $O[\frac{1}{\epsilon}]$ and these are renormalized by adding the last three counter terms in the $\overline{MS}$ renormalization scheme. In the presence of strong magnetic field, space becomes anisotropic and we get different pressures[53] for direction parallel and perpendicular to magnetic field. Longitudinal and transverse pressures are defined as

$$P_z = -F, \quad P_\perp = -F - eB \cdot M = P_z - eB \cdot M, \tag{52}$$

where the magnetization per unit volume $M = -\frac{\partial(F)}{\partial(eB)}$.

7.5. *Results and conclusions*

From Fig. 27, we can see that one-loop pressure increases with the increase in temperature and field strength, respectively. However, the one-loop interacting pressure is higher than that of ideal[50] one in both panels. From Fig. 28, we can see that the one-loop transverse pressure increases with temperature showing similar nature as longitudinal pressure (left panel of Fig. 27) but lower in magnitude. Dashed lines represent transverse ideal pressure which is independent of magnetic field. For a

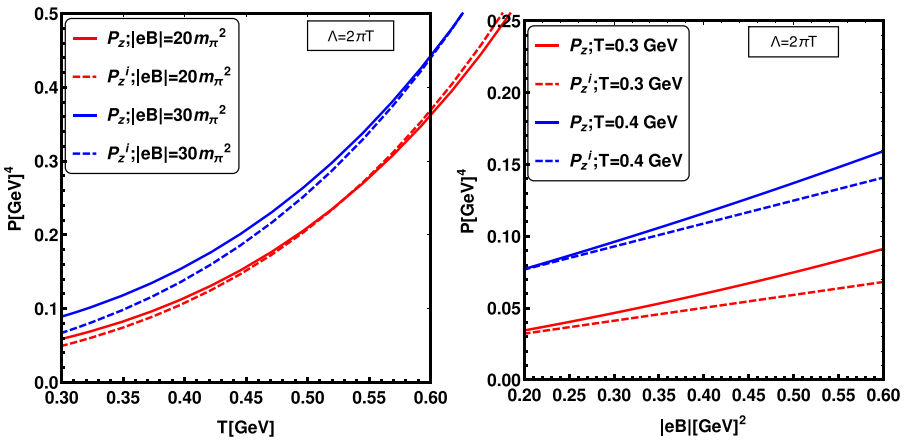

Fig. 27. Variation of one-loop longitudinal pressure as a function of temperature for different value of magnetic field (left panel) and as a function of magnetic field at different temperature (right panel) for number of quark flavor $N_f = 3$ and the central value of the renormalization scale, $\Lambda = 2\pi T$. Dashed curves represent ideal longitudinal pressure.

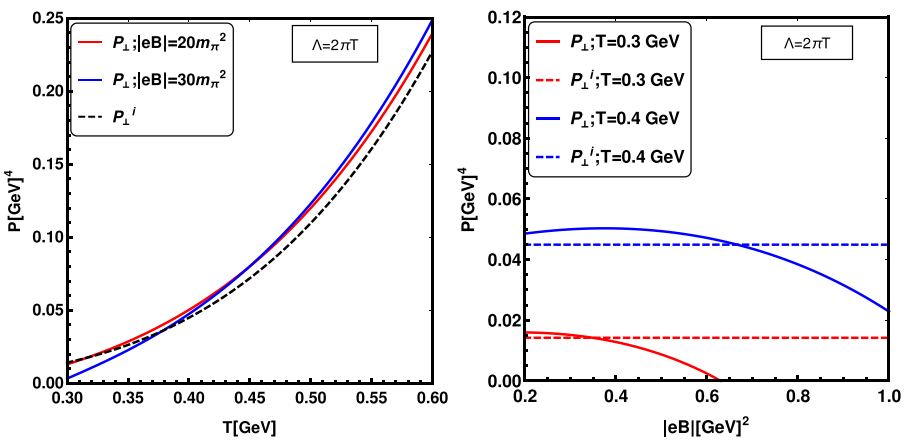

Fig. 28. Variation of the one-loop transverse pressure as a function of temperature for various magnetic fields (left panel) and as a function of magnetic field for different temperatures (right panel). Dashed curves represent ideal transverse pressure.

given high value of the magnetic field, the pressure starts with a lower value than that of ideal gas particularly at low T and then a crossing takes place.

This can also be understood from the right panel where the transverse pressure is displayed as a function of magnetic field for two different temperatures. Here also the dashed lines represent the ideal transverse pressure which is independent of magnetic field. The transverse pressure for interacting case is given in Eq. (52) as $P_\perp = P_z - eB \cdot M$. Now for a given temperature, its variation is very slow (or almost remain unaltered) with lower value of the magnetic field because there is a competition between P_z and eBM. Due to increase of the magnetization M with magnetic field, the transverse pressure $P_\perp$ tends to decrease, falls below ideal gas value and may even go to negative values for low T at large value of magnetic field. This is an indication that the system may shrink in the transverse direction.

Finally, we can conclude that due to the presence of strong background magnetic field, one gets different pressures in direction parallel and perpendicular to magnetic field. Both the pressures are calculated analytically by calculating the magnetization of the system. This anisotropic pressure can be useful for magnetohydrodynamics description of hot deconfined QCD. We have calculated one-loop HTL perturbation theory up to $\mathcal{O}(g^4)$; $\mathcal{O}(g^2)$ and $\mathcal{O}(g^4)$ are incomplete and this result can be improved by higher order loop calculation.

8. On the Microscopic Estimated Values of Transport Coefficients for Quark and Hadronic Matter

Sabyasachi Ghosh, Subhasis Samanta, Kinkar Saha, Snigdha Ghosh, Fernando E. Serna, Mahfuzur Rahaman, Aman Abhishek, Guruprasad Kadam, Pracheta Singha, Sudipa Upadhaya, Soumitra Maity, Sumana Bhattacharyya, Arghya Mukherjee, Payal Mohanty, Bhaswar Chatterjee

From a long list of microscopic calculations of transport coefficients of quark and hadronic matter, few selective references are chosen and their estimated values are tabulated. Through this catalog-type draft on microscopic calculations of transport coefficients, we have pointed out a particular investigation series, which has identified three possible sources — (1) resonance type interaction, (2) finite size effect and (3) effect of magnetic field, which might be responsible for (nearly) perfect fluid nature of RHIC/LHC matter.

8.1. *Introduction*

In 2002, researchers at Duke university discovered a super-cold lithium fluid having very small viscosity to entropy density ratio η/s (< 0.5), close to its quantum lower bound, $\frac{1}{4\pi}$, whereas, three years latter, Relativistic Heavy-Ion Collider (RHIC) experiment at BNL created a super-hot Quark–Gluon Plasma (QGP) with smallest η/s, almost equal to the lower bound. This nearly perfect fluid nature of many body systems at two extreme conditions (super-cold and super-hot) has attracted the attention of large band of theoretical communities from condense matter physics to

nuclear physics to string theory.[54] RHIC data indicated a strongly interacting sQGP medium instead of a weakly interacting gas, which is naturally expected from high temperature Quantum Chromo Dynamics (QCD),[55] due to the asymptotic freedom of QCD. To understand the dynamical origin of low η/s of RHIC matter, several microscopic calculations, based on effective QCD models[56–64] as well as hadronic models,[65–76] have been done in recent time. Present draft is intended to review briefly the estimated values of η/s and other transport coefficients, obtained from different microscopic calculations. Based on investigation series, given in Refs. [58, 61, 66, 67, 68, 69, 71, 72, 64], three possible sources — (1) resonance type interaction, (2) finite size effect and (3) effect of magnetic field are identified for getting low η/s in RHIC/LHC matter. Addressing a brief framework of transport coefficient in the next section, Sec. 8.3 has gone through the discussion on their estimated values, which are listed in tables and pointed out three possible sources for getting low η/s. Lastly, a brief summary is made in Sec. 8.4.

8.2. *Brief framework of transport coefficient*

Let us start with a brief framework of transport coefficients like shear viscosity (η), bulk viscosity (ζ) and electrical conductivity (σ). The macroscopic definition of ideal part of energy–momentum tensor,

$$T_0^{\mu\nu} = -g^{\mu\nu}P + (\epsilon + P)u^\mu u^\nu, \tag{53}$$

which can be connected to its microscopic (kinetic theory) definition,

$$T_0^{\mu\nu} = \int \frac{d^3p}{(2\pi)^3}\frac{p^\mu p^\nu}{E} f, \tag{54}$$

where pressure P, energy density ϵ, four velocity u^μ are macroscopic/fluid quantities but energy $E = \sqrt{\vec{p}^2 + m^2}$, thermal distribution function f are microscopic/particle quantities. For boson/fermion, f will be Bose–Einstein and Fermi–Dirac distribution function at temperature $T = 1/\beta$. Now if the medium is slightly deviated from equilibrium distribution function f to $f + \delta f$, then deviation δf will build a dissipative part of energy–momentum tensor $T_D^{\mu\nu}$, whose microscopic expressions,

$$T_D^{\mu\nu} = \int \frac{d^3p}{(2\pi)^3}\frac{p^\mu p^\nu}{E}\delta f \ , \tag{55}$$

again can be connected with its macroscopic expression,

$$T_D^{\mu\nu} = \eta \boldsymbol{U}_\eta^{\mu\nu} + \zeta \Delta^{\mu\nu}\partial_\rho u^\rho \ , \tag{56}$$

where

$$\boldsymbol{U}_\eta^{\mu\nu} = \left(D^\mu u^\nu + D^\nu u^\mu - \frac{2}{3}\Delta^{\mu\nu}\partial_\rho u^\rho\right),$$
$$\Delta^{\mu\nu} = g^{\mu\nu} - u^\mu u^\nu, D^\mu = \partial^\mu - u^\mu u^\sigma \partial_\sigma. \tag{57}$$

Similar to $T^{\mu\nu}_D$, dissipative part of electric current density J^μ_D will also have connection from macroscopic (Ohm's law) to microscopic expressions

$$\sigma^{\mu\nu}E_\nu = J^\mu_D = e\int \frac{d^3p}{(2\pi)^3}\frac{p^\mu}{E}\delta f. \tag{58}$$

Now, through relaxation time approximate (RTA) of Boltzmann equation, the δf can be expressed in terms of $\boldsymbol{U}^{\mu\nu}_\eta$, $\partial_\rho u^\rho$ and E^μ as

$$\delta f = \beta f(1\pm f)\frac{\tau_c}{E}\left[p_\mu p_\nu \boldsymbol{U}^{\mu\nu}_\eta + \left\{\left(\frac{1}{3}-c_s^2\right)\vec{p}^2 - c_s^2\frac{\partial}{\partial\beta^2}(\beta^2 m^2)\right\}^2 \partial_\rho u^\rho + ep_\mu E^\mu\right]. \tag{59}$$

Implementing Eq. (59) in Eqs. (55), (56) and (58), we get the final expressions of η, ζ and σ for boson/fermion:[60]

$$\begin{pmatrix}\eta\\ \zeta\\ \sigma\end{pmatrix} = \beta\int\frac{d^3\vec{p}}{(2\pi)^3}\tau_c\, f(1\pm f)\begin{pmatrix}\frac{1}{15}\left(\frac{\vec{p}^2}{E}\right)^2\\ \frac{1}{E^2}\left\{\left(\frac{1}{3}-c_s^2\right)\vec{p}^2 - c_s^2\frac{\partial}{\partial\beta^2}\left(\beta^2 m^2\right)\right\}^2\\ \frac{1}{3}\left(\frac{\vec{p}}{E}\right)^2\end{pmatrix}. \tag{60}$$

The degeneracy factor of medium constituents has to be multiplied in above equation and different species have to be summed with appropriate care. It will depend on our dealing system (like quark matter or pionic matter, etc.) or model (effective quark or hadronic model or hadron resonance gas model, etc.).

8.3. *Results and discussion*

8.3.1. *Shear viscosity of quark and hadronic matter*

In earlier section, we came to know the mathematical anatomy of transport coefficients expressions, which can grossly be identified as

$$\begin{aligned}\text{Transport coefficient} &= (\text{thermodynamical phase space})\\ &\quad\times(\text{Relaxation Time}),\end{aligned} \tag{61}$$

if we take momentum independent relaxation time or momentum averaged relaxation time. The thermodynamical phase-space part of η for massless boson or fermion is $\frac{4\pi^2}{450}T^4$ or $\frac{7\pi^2}{900}T^4$ like thermodynamical quantity — entropy density $s = \frac{4\pi^2}{90}T^3$ (boson) or $\frac{7\pi^2}{180}T^3$ (fermion). Hence, the dimensionless quantity η/s will be found as $\frac{\tau_c T}{5}$, which is monotonically increasing function of T if we consider a T-independent τ_c. Now, depending upon our dealing bosonic/fermionic system, different microscopic calculations can get different $\tau_c(T)$, which will ultimately provide the temperature profile of η/s.

Arnold *et al.*[55] have well-summarized η/s calculations, based on the perturbative approach of finite temperature QCD with re-summed version, popularly known as hard thermal loop (HTL). By using the leading order results of HTL calculation[55] for quark matter and chiral perturbation theory (ChPT) for hadronic matter,[37] Refs. 77 and 78 have interestingly shown a possibility of valley type profile of $\eta/s(T)$ like helium, nitrogen and water. However, their order of magnitude ($\frac{10}{4\pi} - \frac{20}{4\pi}$) is quite far from the expectation of experimental side,[79] interpreted through macroscopic hydrodynamical simulation.[80]

Extracted values of η/s by different hydro-groups are well sketched in Fig. 4 of Ref. 81, from where a rough order of magnitude, $\eta/s = \frac{1}{4\pi} - \frac{5}{4\pi}$, is expected for RHIC or LHC matter. Different alternatively models in quark sector like Nambu–Jona–Lasinio (NJL),[56–59] linear sigma model (LSM),[60] polyakov-loop quark meson (PQM)[61] model have estimated η/s of quark matter, while η/s of hadronic matter is estimated through different tools of hadronic phase like URQMD,[82] SMASH[83] codes, Unitarization methodology,[65] hadronic field theory (HFT),[66–70] hadron resonance gas (HRG) model,[71,72] etc. Their estimated values of η/s of hadronic and quark phases, located below and above transition temperature T_c, are listed in Table 1, which carry few selective works, whose results are quite close to KSS bound. The present draft will zoom in the message of Refs. 58, 61, 66, 67, 68, 69, 71, 72, 64, indicating about three possible sources for which η/s of RHIC or LHC matter is appeared to be very low (near to KSS bound). They are discussed below.

(1) Resonance type interaction:

Among the references, listed in Table 1, Refs. 58, 61, 66, 67, 68, 69 have gone through an effective quark-resonance[58,61] and hadron-resonance[66–69] type

Table 1. Order of magnitude of η/s from different model calculations (first column) with references at temperature range below (second column) and above (third column) transition temperature T_c.

Framework	$T \leq T_c$	$T \geq T_c$
HTL[55]	—	1.8
LQCD[86]	—	0.1
NJL[56]	1–0.3	0.3–0.08
NJL[57]	1–0.5	0.5–0.55
NJL[58]	—	0.5–0.12
NJL[59]	2–0.25	0.25–0.5
LSM[60]	0.87–0.55	0.55–0.62
PQM[61]	5–0.5	0.3–0.08
URQMD[82]	1	—
SMASH[83]	1	—
Unitarization[65]	0.8–0.3	—
HFT[66–69]	0.4–0.1	—
HFT[70]	0.8–0.25	—
HRG[71,72]	0.13–0.28	—

interaction, which might be considered as one of the reason for low η/s of quark and hadronic matter. In 1994, it was Quack and Klevansky,[84] who proposed about the quark propagation with quark–meson loop correction in NJL model, which was implemented by Refs. 85, 62 and 58 for viscosity calculations. Through this quark–pion and quark–sigma loop calculations, quark relaxation time (τ_c) is estimated from the imaginary part of quark self-energy (Π) by using the connection $\tau_c \sim 1/\mathrm{Im}\Pi$. Along with the NJL model,[58,62,85] PQM model[61] (through similar quark–meson loop calculations) also found very small τ_c and η/s, close to KSS bound but applicable for a narrow temperature domain near transition temperature. Alternative way to calculate quark relaxation time by using same quark-meson Lagrangian density[84] has been adopted by Refs. 56, 57 and 59. Similar to effective quark-resonance interaction, where π, σ are appeared as resonances of quark matter, effective hadron-resonance interaction has been considered in Refs. 66–70, where σ, ρ, K^*, ϕ mesons, N^*, Δ, Δ^* baryons are appeared as resonances of π, K and N medium. Refs. 66–69 have obtained pion relaxation time from $\pi\sigma$, $\pi\rho$ loops; kaon relaxation time from KK^*, $K\phi$ loops and nucleon relaxation time from πN^*, $\pi\Delta$, $\pi\Delta^*$ loops. On the other hand, Ref. 70 has estimated those relaxation times via resonance-scattering type diagram. Unlike to standard ChPT calculation, both HFT calculations[66–70] found very small η/s. Hence, the resonance type interaction in quark and hadronic matter might be one of the responsible factor for getting low η/s in RHIC or LHC matter.

(2) Finite size effect

Another possible source is finite size effect of medium.[71,72] Due to quantum effect of finite system size, thermodynamical phase space of Eq. (61) can be reduced because lower limit of integration in Eq. (60) can be transformed from 0 to $\vec{p}_{\min} = \pi/R$, where R is system size. On the other hand, relaxation time of hadrons can also face finite size effect by considering only those relaxation scales, which are lower than the system size. References 71 and 72 have shown elaborately how finite size of hadronic matter in HRG model can make impact on reducing the values of η/s. Finite size effect of η/s in effective QCD model is also studied in Ref. 87, which needs an extended investigation for finite size τ_c calculations, after which we can get a complete conclusive picture.

(3) Effect of magnetic field

Another possibility for getting low η/s is hinted from strong magnetic field, which might be produced in the noncentral heavy-ion collisions. Reference 64 has calculated shear viscosity of quark matter in presence of magnetic field, where η/s can be abruptly reduced because of lower effective relaxation time, build by particle relaxation time and synchrotron frequency. However, further investigations are necessary before getting the bold conclusion — magnetic field can be one of the source for getting lower η/s in RHIC/LHC matter.

Table 2. Same as Table 1 for ζ/s.

Framework	$T \leq T_c$	$T \geq T_c$
LQCD[88]	—	1–0
HTL[89]	—	0.002–0.001
NJL[56]	0.9–0.02	0.02–0.002
NJL[57]	1.7–0.13	0.13–0.005
NJL[58]	—	0.1–0.01
NJL[59]	0.61–0.11	0.11–0.004
LSM[60]	0.61–0.11	0.11–0.004
Unitarization[65]	0.04–0.027	—
HRG[73]	0.02–0.003	—
HRG[74]	0.15–0.025	—
HRG[75]	0.1–0.03	—

Table 3. Same as Table 1 for σ/T.

	m_σ	Γ_σ^0
LQCD[90]	—	0.33
LQCD[91]	0.002	0.005–0.015
NJL[56]	0.02–0.015	0.015–0.1
PHSD[63]	0.1–0.02	0.02–0.2
PQM[61]	0.03–0.02	0.01
Unitarization[65]	0.013–0.010	—
HFT[76]	0.004–0.001	—

8.3.2. *Bulk viscosity and electrical conductivity of quark and hadronic matter*

Similar to shear viscosity, other transport coefficients like bulk viscosity ζ and electrical conductivity σ are also rigorously investigated in recent times. List of references with their estimated values of ζ/s and σ/T are tabulated in Tables 2 and 3. Using same microscopic tools, which are able to estimate a very low η/s, one can found the order of other transport coefficients, which are necessary to know for complete dissipative hydrodynamical description. Based on the tabulated values, order of magnitude of transport coefficients of RHIC/LHC matter can be summarized by number: $\eta/s \approx 10^0$–10^{-1}, $\zeta/s \approx 10^0$–10^{-2}, $\sigma/T \approx 10^{-1}$–10^{-3}.

8.4. *Summary*

To synchronize with the expectation from experimental side with macroscopic hydrodynamical simulation, a long list of microscopic calculations are noticed in recent times. Present draft has covered few selective microscopic model calculations, which got a very low viscosity to entropy density ratio of quark/hadronic matter, close to KSS bound. By providing a tabulated format of estimated values for transport coefficients, present draft has attempt to make a catalog on microscopic calculations of transport coefficients. Based on investigation series, given in Refs. 58, 61, 64, 66, 67, 68, 69, 71 and 72, we have concluded that three possible sources — (1) resonance type interaction, (2) finite size effect and (3) effect of magnetic field, might be responsible for (nearly) perfect fluid nature of RHIC/LHC matter.

9. Chiral Transition in a Chirally Imbalanced Plasma in the Presence of Magnetic Field: A Wigner Function Approach

Arpan Das, Deepak Kumar, Hiranmaya Mishra

We discuss here the chiral transition and the associated chiral susceptibility for a chirally imbalanced plasma in the presence of a magnetic field (B) using the Wigner function approach within the framework of the Nambu–Jona–Lasinio model (NJL). As a regularization prescription, we use a medium separation regularization scheme (MSS) in the presence of magnetic field and chiral chemical potential (μ_5) to estimate the chiral condensate and chiral susceptibility. We found that chiral transition temperature increases with the magnetic field, while the transition temperature decreases with μ_5. For a strong magnetic field, we find that the chiral transition temperature as well as susceptibility for up and down type quarks can be nondegenerate.

9.1. *Introduction*

Relativistic heavy-ion collision experiments e.g., at RHIC and LHC, strongly indicate the formation of deconfined quark–gluon plasma (QGP) phase of quantum chromodynamics (QCD) in the initial stages of heavy- ion collision experiments as well as confined hadron phase in the subsequent evolution of QGP. Two very important characteristic features of QCD are color confinement and spontaneous breaking of chiral symmetry. At vanishing temperature and/or density ground state of QCD does not have chirally symmetry. The QCD vacuum undergoes a transition from a chiral symmetry broken phase to a chiral symmetric phase, with an increase in temperature and/or baryon density. Quark–antiquark scalar condensate is the order parameter of the chiral transition.

The study of fluctuations of conserved charges, e.g., net electric charge, baryon number, strangeness, etc., plays an important role to explore the QCD phase diagram.[92] In this investigation, we study chiral transition and the associated chiral susceptibility using the Wigner function approach. Wigner function is the quantum mechanical analog of the classical distribution function. It encodes quantum corrections in the transport equation.[93–95] The covariant Wigner function method for spin-1/2 fermions has been explored to study chiral magnetic effect (CME), dynamical generation of magnetic moment etc.[96–99] Chiral susceptibility which is the measure of the response of the chiral condensate to the variation of the current quark mass has been investigated earlier using lattice QCD (LQCD) simulations,[100] Nambu–Jona–Lasinio (NJL) model[101,102] etc.

A nonvanishing magnetic field of the order of several m_π^2 is expected to be generated in noncentral relativistic heavy-ion collision experiments at RHIC and LHC.[14,103] This apart nontrivial topological field configurations of gluons and Adler–Bell–Jackiw (ABJ) anomaly can give rise to an asymmetry between the number of left and right chiral quarks, i.e., finite chiral chemical potential (μ_5).[104] In this work, we investigate the chiral transition and chiral susceptibility in the

presence of magnetic field and chiral chemical potential (μ_5) in quantum kinetic theory framework using NJL model.[105] It is important to mention that in Ref. 106, it was observed that the chiral transition temperature decreases with μ_5. With a smooth cutoff for the three momentum, it was observed that with increasing μ_5, the chiral transition becomes a first-order transition.[106–108] Nonlocal NJL model analyzed in Ref. 109 shows that the chiral transition temperature increases with μ_5 and the chiral transition is second order. However, in Ref. 110, it has been observed that chiral transition temperature decreases with μ_5 with a smooth cutoff and shows a first-order transition at large μ_5. On the other hand NJL model with "medium separation scheme" (MSS) regularization, as investigated in Ref. 111 shows that the chiral transition temperature increases with μ_5 which is in accordance with some LQCD results.[112,113] In this work, we use a medium separation scheme in the presence of magnetic field and μ_5.[111,114,115] We find that chiral transition temperature decreases with μ_5 as in Refs. 106 and 110.

We organize the paper in the following manner. In Sec. 9.2, we introduce the Winger function in the presence of magnetic field as well as μ_5 and calculate the chiral condensate and chiral susceptibility for two-flavor NJL model. In Sec. 9.3, we present the results and discussions. Finally, in Sec. 9.4, we conclude our results with an outlook to it.

9.2. *Chiral condensate and chiral susceptibility in NJL model for nonvanishing magnetic field and chiral chemical potential*

Using the solutions of the Dirac equation in magnetic field and finite μ_5, the Wigner function has been explicitly written down in Ref. 99. Gauge invariant Wigner function in the presence of magnetic field as given in Ref. 99 is

$$W_{\alpha\beta}(X,p) = \int \frac{d^4X'}{(2\pi)^4} e^{(-ip_\mu X'^\mu - iqByx')} \left\langle \bar{\psi}_\beta \left(X + \frac{X'}{2}\right) \otimes \psi_\alpha \left(X - \frac{X'}{2}\right) \right\rangle, \quad (62)$$

where a specific gauge choice of the external magnetic field is $A^\mu(X) = (0, -By, 0, 0)$. q is the electric charge of the particle. One can express the scalar condensate in terms of the Wigner function as[116]

$$\langle \bar{\psi}\psi \rangle = \int d^4p F(X,p), \quad \text{where } F(X,p) = \mathrm{Tr} W(X,p). \quad (63)$$

For a system in global equilibrium with uniform temperature and chemical potential, as considered in this investigation, Wigner function is independent of space-time. Once the Wigner function is known, it is straight forward to calculate the scalar condensate using Eq. (63). For two-flavor NJL model with u and d quarks for nonvanishing magnetic field and chiral chemical potential as given by the following

Lagrangian[105,117]:

$$\begin{aligned}\mathcal{L} &= \bar{\psi}(i\not{\partial} - m + \mu_5\gamma^0\gamma^5)\psi + G_1\sum_{a=0}^{3}\left[(\bar{\psi}\tau^a\psi)^2 + (\bar{\psi}i\gamma_5\tau^a\psi)^2\right] \\ &\quad + G_2\left[(\bar{\psi}\psi)^2 - (\bar{\psi}\vec{\tau}\psi)^2 - (\bar{\psi}i\gamma_5\psi)^2 + (\bar{\psi}i\gamma_5\vec{\tau}\psi)^2\right], \qquad (64)\end{aligned}$$

where ψ is the $U(2)$ quark doublet $\psi = (\psi_u, \psi_d)^T$, the chiral condensate can be shown to be $\langle\bar{\psi}\psi\rangle_{B\neq 0}^{\mu_5\neq 0} = \sum_{f=u,d}\langle\bar{\psi}_f\psi_f\rangle_{B\neq 0}^{\mu_5\neq 0}$,[118] where

$$\begin{aligned}\langle\bar{\psi}_f\psi_f\rangle_{B\neq 0}^{\mu_5\neq 0} &= -\frac{N_c|q_f|B}{(2\pi)^2}\Bigg[\int dp_z\,\frac{M_f}{E_{p_z,f}^{(0)}}[1 - f_{FD}(E_{p_z,f}^{(0)} - \mu) - f_{FD}(E_{p_z,f}^{(0)} + \mu)] \\ &\quad + \sum_{n=1}^{\infty}\sum_s\int dp_z\frac{M_f}{E_{p_z,s,f}^{(n)}}[1 - f_{FD}(E_{p_z,s,f}^{(n)} - \mu) - f_{FD}(E_{p_z,s,f}^{(n)} + \mu)]\Bigg] \\ &= \langle\bar{\psi}_f\psi_f\rangle_{\text{vac},B\neq 0}^{\mu_5\neq 0} + \langle\bar{\psi}_f\psi_f\rangle_{\text{med},B\neq 0}^{\mu_5\neq 0}. \qquad (65)\end{aligned}$$

Here N_c is the number of colors, μ is the quark chemical potential, n denotes the Landau levels, $s = \pm$ denotes the spin states and f_{FD} is the Fermi-Dirac distribution function. The single particle energy of flavor f can be expressed as $E_{p_z,f}^{(0)} = \sqrt{M_f^2 + (p_z - \mu_5)^2}$ for $n = 0$, $E_{p_z,s,f}^{(n)} = \sqrt{M_f^2 + (\sqrt{p_z^2 + 2n|q_f|B} - s\mu_5)^2}$ for $n > 0$. The second term in Eq. (64) is the four Fermi interaction. $\tau^a, a = 0,\ldots,3$ are the $U(2)$ generators in the flavor space. Third term is the t-Hooft interaction terms which introduces flavor mixing. In the mean field approximation, the constituent quark masses for u and d quarks in terms of the chiral condensates can be given as, $M_u = m_u - 4G_1\langle\bar{\psi}_u\psi_u\rangle - 4G_2\langle\bar{\psi}_d\psi_d\rangle$, $M_d = m_d - 4G_1\langle\bar{\psi}_d\psi_d\rangle - 4G_2\langle\bar{\psi}_u\psi_u\rangle$, respectively. $\langle\bar{\psi}_f\psi_f\rangle_{\text{vac},B\neq 0}^{\mu_5\neq 0}$ which is the zero temperature and zero quark chemical potential (μ) part, contains divergent integral which has been regularized using medium Separation Scheme (MSS) outlined in Refs. 118 and 119.

The chiral susceptibility measures the response of the chiral condensate to the infinitesimal change of the current quark mass. Chiral susceptibility in two-flavor NJL model can be defined as, $\chi_c = \frac{\partial\langle\bar{\psi}\psi\rangle}{\partial m} = \frac{\partial\langle\bar{\psi}_u\psi_u\rangle}{\partial m} + \frac{\partial\langle\bar{\psi}_d\psi_d\rangle}{\partial m}$. To estimate chiral susceptibility, we have to estimate $\frac{\partial\langle\bar{\psi}_f\psi_f\rangle}{\partial M_f}$. Similar to chiral condensate, $\frac{\partial\langle\bar{\psi}_f\psi_f\rangle}{\partial M_f}$ also has divergent integrals which can be regularized using the medium separation regularization scheme.[118]

9.3. *Results*

NJL model as described by Eq. (64) has the following parameters, two couplings G_1, G_2, the three momentum cutoff Λ and the current quark masses m_u and m_d. To study the effects of flavor mixing, the couplings G_1 and G_2 are parametrized as $G_2 = \alpha g$, $G_1 = (1-\alpha)g$.[105,117] The extent of flavor mixing is controlled by α and it can be argued to have a value $0 \leq \alpha \leq 0.5$.[120] For phenomenological reason, we

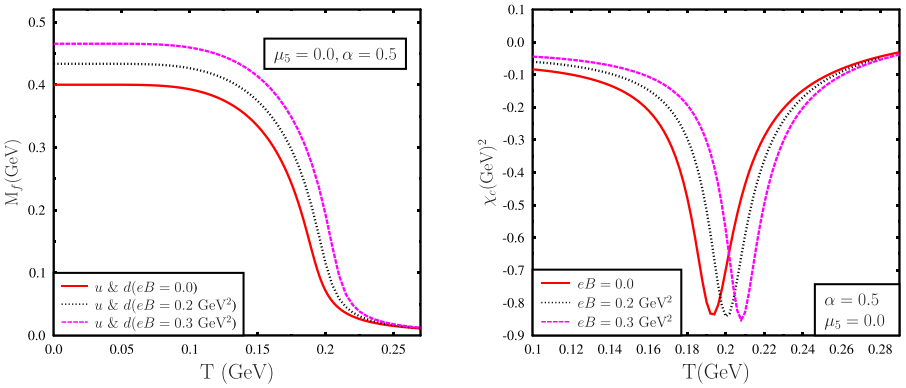

Fig. 29. Left plot: Variation of M_u and M_d, with temperature for $\mu_5 = 0$, but with different values of magnetic field for $\alpha = 0.5$. Right plot: Variation of χ_c with temperature (T) for $\mu_5 = 0$, but with different values of magnetic field for $\alpha = 0.5$.[118]

take the parameters $m_u = m_d = 6\,\text{MeV}$, $\Lambda = 590\,\text{MeV}$ and $g = 2.435/\Lambda^2$.[105] Next we show some of the important results of our study (for details see Ref. 118).

In Fig. 29, we show the variation of M_u and M_d and the chiral susceptibility (χ_c), with temperature for $\mu_5 = 0$ and with different values of magnetic field for $\alpha = 0.5$. Even in the presence of magnetic field $M_u = M_d$ for $\alpha = 0.5$. From the left and the right plot in Fig. 29, it is clear that constituent quark mass and chiral transition temperature increases with increasing magnetic field.

In Fig. 30, we show the variation of M_u and M_d and the associated total chiral susceptibility (χ_c), with temperature for $\mu_5 = 0$ and with different values of magnetic field for $\alpha = 0.0$. For $\alpha = 0.0$, there is no flavor mixing. From the left plot, it is clear that at finite magnetic field $M_u \neq M_d$. For nonvanishing magnetic field u and d, quark condensates are different and for $\alpha = 0.0$, M_u is independent of

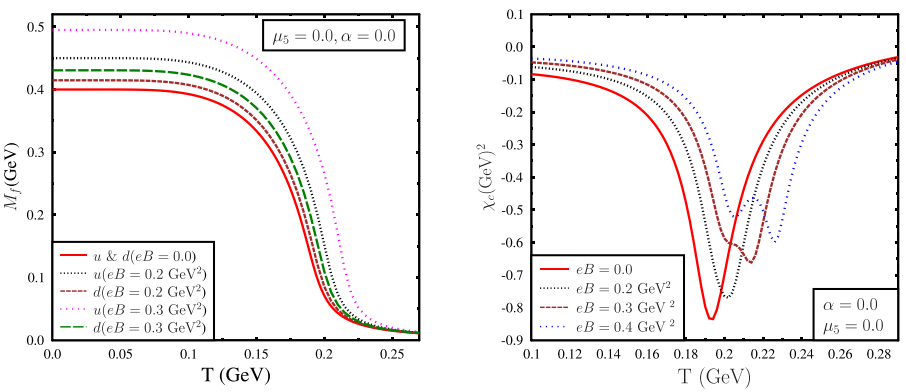

Fig. 30. Left plot: Variation of M_u and M_d, with temperature for $\mu_5 = 0$, but with different values of magnetic field for $\alpha = 0.0$. Right plot: Variation of χ_c with temperature (T) for $\mu_5 = 0$, but with different values of magnetic field for $\alpha = 0.0$.[118]

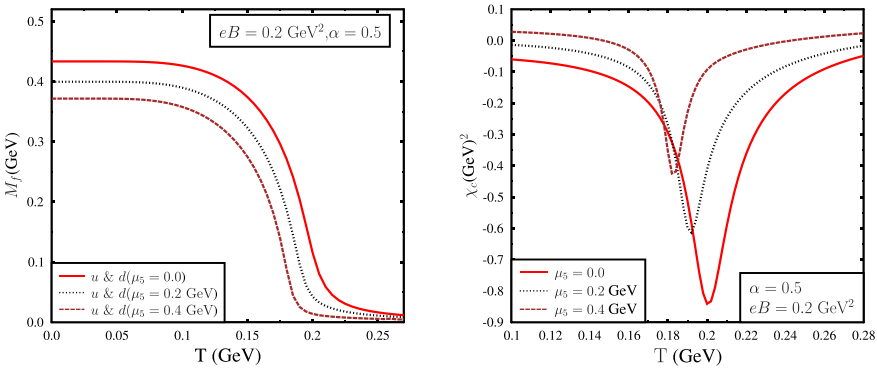

Fig. 31. Left plot: Variation of quark mass $M_u = M_d$, with temperature for finite B and μ_5. Right plot: Variation of χ_c with temperature for finite B and μ_5.[118]

$\langle\bar{\psi}_d\psi_d\rangle$. Similarly M_d does not depend on $\langle\bar{\psi}_u\psi_u\rangle$ for $\alpha = 0.0$. From the right plot in Fig. 30, it is clear that chiral transition temperature increases with increasing magnetic field. However, unlike the case when $\alpha = 0.5$, in this case susceptibility plot shows two distinct peaks for relatively large magnetic fields. These two peaks are associated with u and d quarks. In general, for $\alpha \neq 0.5$, chiral transition temperature associated with u and d type quarks are nondegenerate.

Finally, in Fig. 31, we show the variation of M_u and M_d and the associated susceptibilities (χ_c) with temperature for nonvanishing magnetic field and chiral chemical potential for $\alpha = 0.5$. From Fig. 31, it is clear that with μ_5 quark mass as well as transition temperature decreases.

9.4. *Conclusion*

In this investigation, we have studied chiral transition and the associated chiral susceptibility for nonvanishing magnetic field and μ_5 using Wigner function approach within the framework of two-flavor NJL model. We used a medium separation regularization scheme to regulate divergent integral. With increasing μ_5 constituent quark masses and the chiral transition temperature decreases. On the other hand, with increasing magnetic field, quark masses and chiral transition temperature increase. Further, in the absence of maximal flavor mixing, i.e., $\alpha \neq 0.5$, u quark mass is larger than d quark mass for nonvanishing magnetic field. Also chiral susceptibility shows two distinct peaks for high magnetic field associated with u and d quarks for $\alpha \neq 0.5$.

10. Electrical Conductivity and Hall Conductivity of Hot and Dense Hadron Gas in a Magnetic Field

Arpan Das, Hiranmaya Mishra, Ranjita K. Mohapatra

We estimate the electrical conductivity and the Hall conductivity of hot and dense hadron gas using the relaxation time approximation of the Boltzmann transport

equation in the presence of electromagnetic field. We have investigated the temperature and the baryon chemical potential dependence of these transport coefficients. We find that the electrical conductivity decreases in the presence of magnetic field. The Hall conductivity on the other hand shows a nonmonotonic behavior with respect to the dependence on magnetic field. We argue that for a pair plasma (particle-anti particle plasma) where $\mu_B = 0$, Hall conductivity vanishes. Only for nonvanishing baryon chemical potential, Hall conductivity has nonzero value. We also estimate the electrical conductivity and the Hall conductivity as a function of the center of mass energy along the freeze-out curve.

10.1. *Introduction*

Transport coefficients of strongly interacting matter created in the relativistic heavy-ion collision experiments are of great importance for a comprehensive understanding of the hot and dense QCD (quantum chromodynamics) medium produced in these experiments. In the dissipative relativistic hydrodynamical model of the hot and dense medium, transport coefficients, e.g., shear and bulk viscosity etc, play an important role. In fact, it has been shown that a small shear viscosity to entropy ratio (η/s) is necessary to explain the flow data. The bulk viscosity ζ also plays a significant role in the dissipative hydrodynamics describing the QGP evolution. The bulk viscosity encodes the conformal measure $(\epsilon - 3P)/T^4$ of the system and lattice QCD simulations show a nonmonotonic behavior of both η/s and ζ/s near the critical temperature T_c.

In case of noncentral heavy-ion collisions, due to the collision geometry, a large magnetic field is also expected to be produced. The magnitude of the produced magnetic field at the initial stages in these collisions are expected to be rather large, at least of the order of several m_π^2. Since the strength of the magnetic field is of hadronic scale, the effect of the magnetic field on the QCD medium can be significant.

In this work, we investigate the electrical and the Hall conductivity of the hot and dense hadron gas produced in the subsequent evolution of QGP.

10.2. *Boltzmann equation in relaxation time approximation*

The relativistic Boltzmann transport equation (RBTE) of a charged particle of single species in the presence of external electromagnetic field can be written as

$$p^\mu \partial_\mu f(x,p) + eF^{\mu\nu} p_\nu \frac{\partial f(x,p)}{\partial p^\mu} = \mathtt{C}[f], \tag{66}$$

$\mathtt{C}[f]$ is the collision integral. In the relaxation time approximation (RTA), the collision integral can be written as

$$\mathtt{C}[f] \simeq -\frac{p^\mu u_\mu}{\tau}(f - f_0) \equiv -\frac{p^\mu u_\mu}{\tau}\delta f, \tag{67}$$

Electric current is given by

$$j^i = e \int \frac{d^3p}{(2\pi)^3} v^i \delta f = \sigma^{ij} E_j = \sigma^{\rm el} \delta^{ij} E_j + \sigma^H \epsilon^{ij} E_j, \tag{68}$$

where ϵ_{ij} is the antisymmetric 2×2 unity tensor, with $\epsilon_{12} = -\epsilon_{21} = 1$. Then the electrical and the Hall conductivity can be identified as

$$\sigma^{\rm el} = \sum_i \frac{e_i^2 \tau_i}{3T} \int \frac{d^3p}{(2\pi)^3} \frac{p^2}{\epsilon_i^2} \frac{1}{1 + (\omega_{ci}\tau_i)^2} f_0, \tag{69}$$

$$\sigma^H = \sum_i \frac{e_i^2 \tau_i}{3T} \int \frac{d^3p}{(2\pi)^3} \frac{p^2}{\epsilon_i^2} \frac{\omega_{ci}\tau_i}{1 + (\omega_{ci}\tau_i)^2} f_0, \tag{70}$$

10.3. *Results and discussions*

We have considered a uniform radius of $r_h = 0.5$ fm for all the mesons and baryons we have estimated the electrical conductivity and the Hall conductivity using Eqs. 69 and 70.

It is clear from Fig. 32, left plot, $\sigma^{\rm el}/T$ decreases monotonically with temperature at $B = 0$. This can be associated with the increase of randomness of the system with larger collision rate leading to smaller relaxation time. We point out here that the dominant contribution to the electrical conductivity arises from the charged pions due to the small mass of the pions as compared to that of other hadrons. Thus, the monotonic decrease of $\sigma^{\rm el}/T$ is due to the decrease of relaxation time of pions with increasing temperature.

For nonvanishing magnetic field, the behavior of $\sigma^{\rm el}/T$ is very different as compared to $B = 0$ counterpart. First, it is observed that with increase in magnetic field strength, the electrical conductivity decreases. This decrease in electrical conductivity with the magnetic field can be understood physically. At zero magnetic

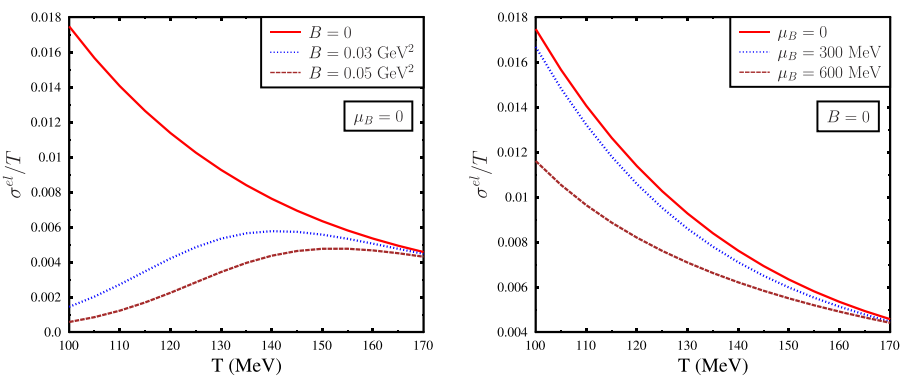

Fig. 32. Left plot: Variation of normalized electrical conductivity ($\sigma^{\rm el}/T$) with temperature (T) for different values of magnetic field (B) at zero baryon chemical potential. Right plot: Variation of $\sigma^{\rm el}/T$ with temperature T for different values of baryon chemical potential μ_B at zero magnetic field.

field, the electric current is along the direction of the electric field. However, at finite magnetic field, charges also diffuse transverse to both electric and magnetic field, due to the Lorentz force, giving rise to a reduced current along the direction of electric field. This is also reflected in the expression for electrical conductivity as in Eq. (69).

It is clear from Fig. 32 (right plot) that with increasing chemical potential (μ_B), electrical conductivity decreases. For the range of μ_B considered here, the contribution to the electrical conductivity from the charged hadrons is dominated by the charged pions similar to the case with vanishing chemical potential. At finite chemical potential, the pion relaxation time decreases with μ_B due to scattering with the baryons, mostly from the nucleons. One would have naively expected the nucleon contribution to the electrical conductivity to increase with μ_B, which will lead to an increase in the total electrical conductivity due to the μ_B-dependent distribution function in the expression of electrical conductivity. However, this increase of the baryonic contribution to the electrical conductivity is not enough to compensate the decreasing contribution arising from pions, at least for the chemical potential considered in the present investigation. This leads to a decrease of the total electrical conductivity with increase in baryon chemical potential at vanishing magnetic field.

Next, we discuss the variation $\sigma^{\rm el}/T$ with temperature (T) in presence of magnetic field and for different values of baryon chemical potential (μ_B). This is shown in Fig. 33. Unlike the vanishing magnetic field case, it is seen that $\sigma^{\rm el}/T$ increases with baryon chemical potential. This behavior can be understood as follows. At finite magnetic field, the contributions of the mesons to the electrical conductivity further decrease due to larger cyclotron frequency as compared to baryons, apart from the decrease in the relaxation time with increase in μ_B.

Next, we discuss Hall conductivity in hadronic gas within HRG model. In Fig. 34 (left plot), we show the variation of Hall conductivity with temperature (T) for

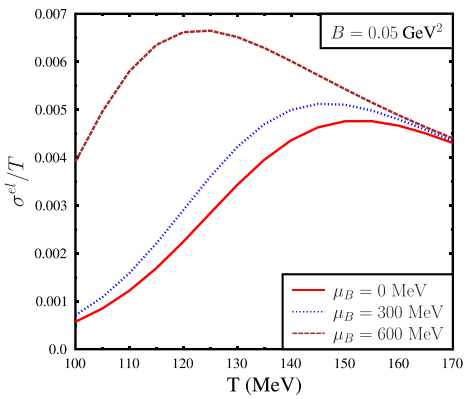

Fig. 33. Variation of normalized electrical conductivity $\sigma^{\rm el}/T$ with temperature for different values of baryon chemical potential μ_B at $B = 0.05$ GeV^2.

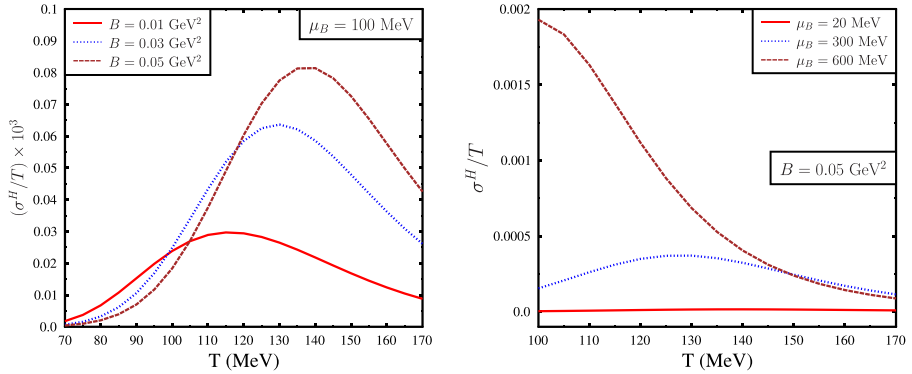

Fig. 34. Left plot: Variation of normalized Hall conductivity σ^H/T with temperature for various values of magnetic field at $\mu_B = 100$ MeV. Right plot: Variation of normalized Hall conductivity σ^H/T with temperature for various values of baryon chemical potential at $B = 0.05$ GeV^2.

different values of the magnetic field at finite baryon chemical potential $\mu_B = 100$ MeV. Let us note that due to the opposite gyration of the particles and the antiparticles in a magnetic field, the mesonic contribution to the Hall conductivity gets exactly cancelled out. Hence, it is only the baryons which contribute to the Hall conductivity at finite baryon chemical potential. It may be observed in Fig. 34 that for the small temperature, the Hall conductivity decreases with increase in magnetic field, while for larger temperature the Hall conductivity increases with magnetic field. At low temperature, since the relaxation time is smaller then the Hall conductivity the integrand $\sim \frac{1}{\omega_c \tau}$ ($\omega_c = \frac{eB}{\epsilon}$), which explains the suppression of Hall conductivity with increasing magnetic field. On the other hand, at large temperature with smaller relaxation time the integrand $\sim \omega_c \tau$ which explains the increase in the Hall conductivity with increasing magnetic field.

In Fig. 34 (right plot), we plotted the variation of the normalized Hall conductivity σ^H/T with temperature for different values of baryon chemical potential at $B = 0.05\,\text{GeV}^2$. As may be noted from this figure for smaller chemical potential, the Hall conductivity is smaller. This is due to the fact that for finite Hall conductivity, the imbalance between the number of particles and antiparticles is required. With increase in baryon chemical potential, the number density of particles is significantly larger than that of antiparticles leading to a nonvanishing Hall current. Again the nonmonotonic behavior of normalized Hall conductivity with temperature for a specific value of the magnetic field is similar to Fig. 34 (left plot)

In Fig. 35, we have considered values of the magnetic field ranging from $B = 0.001\,\text{GeV}^2$ to $B = 0.04\,\text{GeV}^2$ for different center-of-mass energy. Let us note that for RHIC, the center-of-mass energy 200 GeV and the estimated maximum magnetic field are of the order of $B = 0.04\,\text{GeV}^2$. For this value of the magnetic field and the collision energy, we get that the value of normalized Hall conductivity σ^H/T for RHIC is of the order of 10^{-5} and the value of normalized electrical conductivity is of the order of 10^{-3}. On the other hand, for relatively low energy collisions,

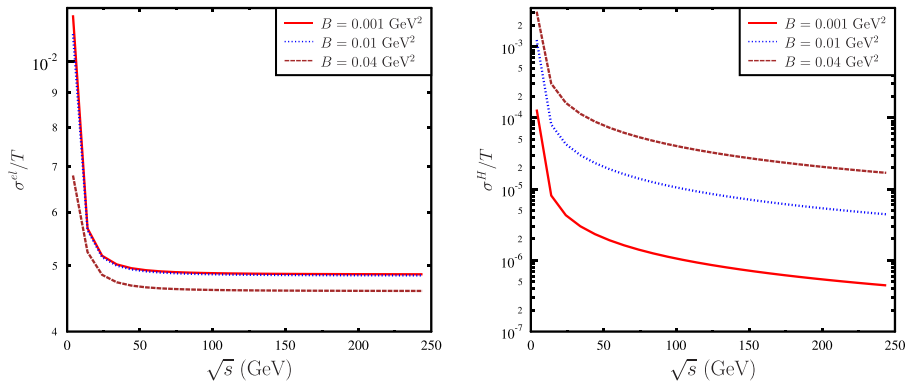

Fig. 35. Left plot: Variation of normalized electrical conductivity $\sigma^{\rm el}/T$ with center-of-mass energy for difference values of magnetic fields, Right plot: Variation of normalized Hall conductivity σ^{H}/T with center-of-mass energy $(\sqrt{s})$ for different values of magnetic field. With increasing magnetic field, $\sigma^{\rm el}/T$ decreases and σ^{H}/T increases.

e.g., FAIR, the collision energy E_{lab} $10AGeV$ and the estimated maximum value of the magnetic field are of the order of $B = 0.001\,\text{GeV}^2$. For this value of the magnetic field and the collision energy relevant for FAIR, the value of normalized Hall conductivity is of the order of 10^{-4} and the normalized electrical conductivity is of the order of 10^{-2}.

10.4. *Summary and conclusions*

In this investigation, we have estimated the electrical $(\sigma^{\rm el})$ and the Hall conductivity (σ^{H}) of the hot and dense hadron gas in the presence of an external magnetic field. We have not considered the Landau quantization of the charged particles as well as magnetic-field-dependent dispersion relation due to relatively smaller magnetic field.

11. Effect of Dynamical Chiral Symmetry Breaking on the Electrical Resistivity of Magnetized Quark Matter

Jayanta Dey, Sabyasachi Ghosh, Aritra Bandyopadhyay, Ricardo L. S. Farias, Gastão Krein

We studied the effects of dynamical chiral symmetry breaking (DCSB) on the resistivity of quark matter in the presence of magnetic field. For massless quarks, we obtained the expected dissipation-less transverse Hall resistivity along with a longitudinal Drude's resistivity; while the former is independent of magnetic field, the latter is proportional to the magnetic field. At low temperatures and large magnetic fields, quarks become massive due to DCSB. We found that DCSB leads to a nontrivial temperature and field dependence for both longitudinal and transverse resistivity components.

11.1. *Introduction*

Strong magnetic fields are expected to be produced in relativistic heavy-ion collision (HIC) experiments.[14,121] Different physical properties of the quark matter created in these experiments can be affected by the magnetic field. In the present communication, we present results on the effect of dynamical chiral symmetry breaking (DCSB) on the resistivity of magnetized quark matter. We first revisit the standard resistivity expression derived by connecting the macroscopic Ohm's law and the microscopic Drude's approach. This leads to the well-known inverse relation between electrical resistivity and electrical conductivity. In the presence of a magnetic field, along with the normal, longitudinal resistivity, there appears a Hall resistivity, transverse to the magnetic field. We study the temperature and magnetic field dependencies of these resistivity components. We considered the case of massless quarks and massive quarks, with the masses being temperature and magnetic field dependent. The masses are generated through the mechanism of DCSB. We use the Nambu–Jona–Lasinio model to obtain the quark masses.

11.2. *Formalism*

11.2.1. *Resistivity without magnetic field*

Let us assume an electric field applied along the x-axis, $\vec{E} = \hat{x}E_x$; then, a current density $\vec{J_x} = \hat{x}J_x$ along the same direction is generated. The potential $V = \int E_x dx$ and current $I = \int J_x dydz$ follow the macroscopic Ohm's law, $V = RI$, where R is the resistance of the medium. The vector form of Ohm's law can be written as

$$E_x\hat{x} = \rho_{xx}J_x\hat{x} \quad \text{or} \quad \sigma_{xx}E_x\hat{x} = J_x\hat{x}, \tag{71}$$

where the resistivity, $\rho_{xx} = 1/\sigma_{xx}$ (σ_{xx} is conductivity), is a more appropriate dissipative quantity than R. By this definition, the dimensions of ρ and R are related by $[\rho] = [R] \times \text{Area/Length}$. A microscopic derivation of the resistivity can be obtained using Drude's assumption that an external electric field E_x accelerates a charge particle from rest to a finite momentum mv_x within a relaxation time τ_c. Therefore, a given quark with flavor f and electric charge e_f and mass m_f experiences the force:

$$e_f E_x = \frac{m_f v_x}{\tau_c}, \tag{72}$$

and hence, the current density can be expressed as

$$J_x = e_f n_f v_x = e_f n_f \left(\frac{e_f \tau_c E_x}{m_f}\right) = \left[\frac{e_f^2 n_f \tau_c}{m_f}\right] E_x, \tag{73}$$

where n_f is the electric charge number density in the medium. Comparing Eqs. (71) and (73), one can get Drude's expression of conductivity or resistivity

$$\sigma_{xx} = \frac{1}{\rho_{xx}} = \sigma_D^{\text{NR}} = \frac{e_f^2 n_f \tau_c}{m_f}. \tag{74}$$

The NR in $\sigma_D^{\rm NR}$ denotes the nonrelativistic nature of this expression; it can in principle be applied to quark matter with massive constituent quarks, where different flavor charges (e.g., $e_u = +\frac{2}{3}e$, $e_d = -\frac{1}{3}e$) with their spin, color and particle–antiparticle degeneracy factors have to be taken into account.

A relativistic expression can be obtained using the energy–momentum relation $E = \sqrt{p^2 + m^2}$ and Boltzmann's equation for the quark distribution in medium:

$$\frac{\partial f}{\partial t} + \frac{\partial x}{\partial t}\frac{\partial f}{\partial x} + e_f E_x \frac{\partial f}{\partial p_x} = \left(\frac{\partial f}{\partial t}\right)_{\rm coll}. \tag{75}$$

Writing $f = f_0 + \delta f$, where f_0 is the equilibrium distribution $f_0 = 1/(e^{\beta E} + 1)$ and δf the deviation of f from f_0 within a time scale τ_c, and using the relaxation-time approximation, in which $(\partial f/\partial t)_{\rm coll} = -\delta f/\tau_c$, Eq. (75) is solved by

$$e_f E_x \frac{p_x}{E}\beta f_0(1 - f_0) = \frac{\delta f}{\tau_c}. \tag{76}$$

This leads to

$$\begin{aligned} J_x &= e_f \int \frac{d^3p}{(2\pi)^3}\left(\frac{p_x}{E}\right)\delta f \\ &= \left[e_f^2 \int \frac{d^3p}{(2\pi)^3}\left(\frac{p_x}{E}\right)^2 \tau_c \beta f_0(1 - f_0)\right] E_x, \end{aligned} \tag{77}$$

and so

$$\begin{aligned} \sigma_{xx} = \sigma_D^R = 1/\rho_{xx} &= e_f^2 \int \frac{d^3p}{(2\pi)^3}\left(\frac{p_x}{E}\right)^2 \tau_c \beta f_0(1 - f_0) \\ &= \frac{e_f^2}{3} \int \frac{d^3p}{(2\pi)^3}\left(\frac{p}{E}\right)^2 \tau_c \beta f_0(1 - f_0). \end{aligned} \tag{78}$$

11.2.2. *Resistivity in the presence of a magnetic field*

In presence of a magnetic field along the z-axis, $\vec{B} = \hat{z}B$, the charge particle is subjected to a Lorentz force which in turn generates a current density perpendicular to $\vec{B}$; the components J_x and J_y can be expressed in matrix form as[122]

$$\begin{aligned} \begin{pmatrix} J_x \\ J_y \end{pmatrix} &= \begin{pmatrix} \sigma_{xx} & \sigma_{xy} \\ \sigma_{yx} & \sigma_{yy} \end{pmatrix} \begin{pmatrix} E_x \\ 0 \end{pmatrix} \\ \begin{pmatrix} \rho_{xx} & \rho_{xy} \\ \rho_{yx} & \rho_{yy} \end{pmatrix} \begin{pmatrix} J_x \\ J_y \end{pmatrix} &= \begin{pmatrix} E_x \\ 0 \end{pmatrix}, \end{aligned} \tag{79}$$

where

$$\sigma_{xx} = \sigma_{yy} = \sigma_D \frac{1}{1 + (\tau_c/\tau_B)^2},$$

$$\sigma_{yx} = -\sigma_{xy} = \sigma_D \frac{\tau_c/\tau_B}{1 + (\tau_c/\tau_B)^2},$$

$$\rho_{xx} = \rho_{yy} = \frac{1}{\sigma_D},$$
$$\rho_{xy} = -\rho_{yx} = \frac{\tau_c}{\tau_B \sigma_D}, \tag{80}$$

where τ_B is another times scale along with collisional relaxation time τ_c, with $\tau_B = m_f/(eB)$ in a nonrelativistic treatment or $\tau_B = E_{av}/(eB)$ in a relativistic treatment, where E_{av} is the average value

$$E_{av} = \frac{\int \frac{d^3p}{(2\pi)^3} E f_0}{\int \frac{d^3p}{(2\pi)^3} f_0}. \tag{81}$$

In addition, in Eq. (80), we consider the Drude conductivities $\sigma_D = \sigma_D^{\mathrm{NR}/R}$ for the nonrelativistic or relativistic treatments.

11.2.3. *NJL model in presence of magnetic field*

Magnetized quark matter is described within a quasi-particle model within the Nambu–Jona–Lasinio (NJL) model framework. In the NJL model, the constituent quark mass $M = M(T, B)$, which is a function of the temperature T and magnetic field B, is obtained by solving the gap equation:

$$M = m - 2G \sum_{f=u,d} \langle \bar{\psi}_f \psi_f \rangle, \tag{82}$$

where $\langle \bar{\psi}_f \psi_f \rangle$ is the quark condensate, given by:

$$\langle \bar{\psi}_f \psi_f \rangle = \langle \bar{\psi}_f \psi_f \rangle^{\mathrm{vac}} + \langle \bar{\psi}_f \psi_f \rangle^{B} + \langle \bar{\psi}_f \psi_f \rangle^{T,B}. \tag{83}$$

The expressions for the different contributions can be found in Ref. 123.

11.3. *Numerical results and discussion*

Resistivity without magnetic field for massless fluid follows the simple analytic expression

$$\rho_{xx} = \frac{36}{e_f^2 \tau_c T^2}, \tag{84}$$

which remains the same in the presence of magnetic field. However, the Hall resistivity resistivity becomes a function of the magnetic field, namely:

$$\rho_{xy} = \left(\frac{36}{e_f^2 \tau_c T^2}\right)\left(\frac{\tau_c}{\tau_B}\right) = \left(\frac{36}{e_f^2 T^2}\right)\left(\frac{eB}{E_{av}}\right). \tag{85}$$

While $\rho_{xy} \propto B$, ρ_{xx} is independent of B. The average energy, given in Eq. (81), will be $E_{av} = \frac{7\zeta(4)}{2\zeta(3)} T \propto T$. Hence, $\rho_{xx} \propto \frac{1}{\tau_c T^2}$ and $\rho_{xy} \propto \frac{1}{T^3}$, which indicates the dissipation-free nature of Hall resistivity.

Figure 36 displays $u-$quark ρ_{xx} and ρ_{xy} resistivity components (multiplied by $\tau_c T^2$) as a function of T, for $eB = 0.2$ GeV^2. For massless quarks (blue-solid and dashed-green curves), while the xy component follows a $1/T$ dependence, the xx component is independent of T. For quarks with a mass $M(T, eB = 0.2 \text{ GeV}^2)$ obtained from the NJL model (blue-dotted and red-dash-dotted curves), ρ_{xx} and ρ_{xy} have a similar T-dependence. For T large, they approach the massless limits, as expected. However, at low temperatures, when there is substantial dynamical chiral symmetry breaking, the resistivity components are enhanced.

Figure 37 displays the magnetic field dependence of ρ_{xx} and ρ_{xy} for $T = 0.17$ GeV, again for u quarks only. For massless quarks (black-dashed and red-dotted

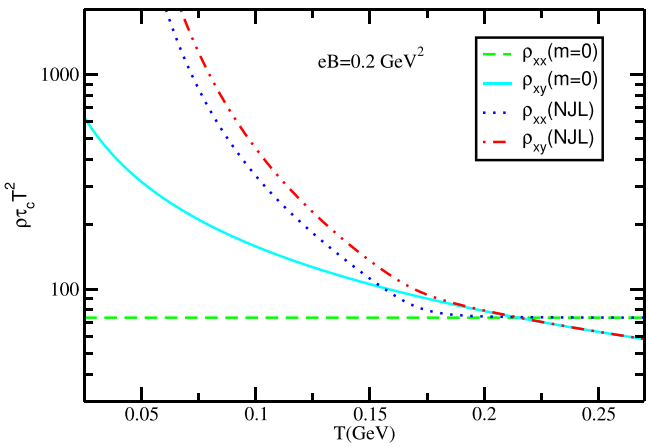

Fig. 36. Temperature dependence of normalized values of ρ_{xx}, ρ_{xy} for massless case and in NJL model.

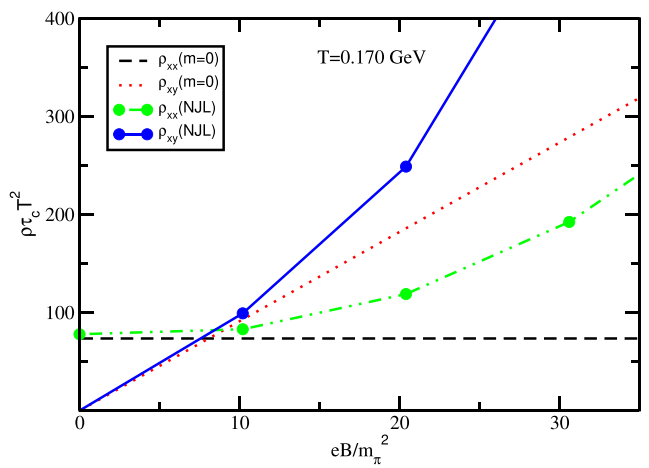

Fig. 37. Magnetic field dependence of normalized values of ρ_{xx}, ρ_{xy} for massless case and in NJL model.

lines), while ρ_{xx} is B-independent, $\rho_{xy} \propto B$. This is well understandable from the massless relations, given in Eqs. (84) and (85). Now when we use T- and B-dependent constituent quark mass, both ρ_{xx} and ρ_{xy} increase with B. The deviations from the massless cases become more prominent at large values of B.

Figures 36 and 37 reveal the expected behavior of the normal (ρ_{xx}) and Hall (ρ_{xy}) resistivity components at low-B and high-T values, whereas the effect of a finite quark condensate, signaling dynamical chiral symmetry breaking, is clearly noticeable.

11.4. *Summary*

In summary, we have studied the resistivity of quark matter in the presence of a magnetic field along the z-direction. We obtained the normal Drude's resistivity along the x-axis, ρ_{xx}, and also the Hall resistivity, ρ_{xy}, transverse to a magnetic field. We considered massless quarks and T- and B-dependent massive quarks, with the masses obtained with NJL model. We have shown that the results for both components of the resistivity are drastically different in the massless and massive cases, particularly at low temperature and high magnetic field, for which dynamical chiral symmetry breaking is realized.

12. Nonconformal Solution of Viscous Landau Hydrodynamics

Deeptak Biswas, Kishan Deka, Amaresh Jaiswal, Sutanu Roy

We have solved viscous landau hydrodynamics for a nonconformal fluid with a constant speed of sound in the 1+1 dimension. The analytic solution has been obtained considering relativistic Navier–Stokes form of the dissipative hydrodynamic equation. The nonconformal Landau flow has a better agreement with the experimental data than the conformal Landau flow solution with a fitted value of the speed of sound (c_S^2).

12.1. *Introduction*

The phase structure of strongly interacting matter can be studied from the medium created in the collision of two highly relativistic nuclei.[124–126] The created medium expands very fast due to the high-pressure gradient. This space-time evolution can be addressed using relativistic dissipative hydrodynamic simulations.[80,81,127–133] In 1953, Landau first studied this hydrodynamical evolution for an ideal conformal fluid[134] which gave rise to a gaussian rapidity distribution of produced particles which has better agreement[135–140] with p_T integrated yield over whole rapidity range. In Landau's model, a fast longitudinal expansion is followed by a slower expansion in the transverse plane. Freezeout happens when the transverse displacement becomes larger than the initial transverse dimension. The final rapidity distribution of particles is therefore given by the rapidity distribution at the freeze-out time.[135–151] Here we solve viscous landau hydrodynamics for a nonconformal equation of state in the Navier–Stokes limit and employ the obtained solution to fit

rapidity spectrum of observed pions in $\sqrt{s_{\rm NN}}$ = 200, 17.3, 12.3, 8.76, 7.62, 6.27, 4.29, 3.83, 3.28 and 2.63 GeV collision energies. We find that the Landau flow with a nonconformal equation of state leads to a better agreement with the experimental data compared to the conformal Landau flow solution for a fitted value of c_S^2. The value of the squared speed of sound shows a monotonic decrease with decreasing collision energies.

12.2. *Viscous Landau flow*

The energy–momentum tensor of a relativistic fluid in the Navier–Stokes limit is[152]

$$T^{\mu\nu} = \epsilon\, u^\mu u^\nu - (P - \zeta\theta)\,\Delta^{\mu\nu} + 2\eta\sigma^{\mu\nu}, \tag{86}$$

where ϵ is the local energy density, P is the thermodynamic pressure, u^μ is the fluid four-velocity and, η and ζ are the coefficients of shear and bulk viscosity, respectively. Here, $\Delta^{\mu\nu} \equiv g^{\mu\nu} - u^\mu u^\nu$, $\theta \equiv \partial_\mu u^\mu$ and $\nabla^\mu \equiv \Delta^{\mu\nu}\partial_\nu$. The metric convention is $g^{\mu\nu} = {\rm diag}(1, -1, -1, -1)$. Using these definitions, the shear tensor can be written as $\sigma^{\mu\nu} \equiv \frac{1}{2}(\nabla^\mu u^\nu + \nabla^\nu u^\mu) - \frac{1}{3}\Delta^{\mu\nu}\nabla_\alpha u^\alpha$. Here we have used the nonconformal equation of state, $P = c_s^2\epsilon$, where the speed of sound c_s^2 will be assumed to be constant for simplicity.

Following Ref. 134, the hydrodynamic equation for longitudinal expansion along z-direction can be written, $\partial_\mu T^{\mu\nu} = 0$, leads to[134,140]

$$\frac{\partial T^{00}}{\partial t} + \frac{\partial T^{03}}{\partial z} = 0, \quad \frac{\partial T^{03}}{\partial t} + \frac{\partial T^{33}}{\partial z} = 0, \tag{87}$$

here, $(t, x, y, z) \equiv (x^0, x^1, x^2, x^3)$. The nonzero velocity fields can be written in terms of longitudinal fluid rapidity, y as $u^0 = \cosh y$ and $u^3 = \sinh y$. Changing our set of co-ordinates following Ref. 140 from (t, z) to light-cone variables, $t_\pm \equiv t \pm z$, Equation (87) becomes

$$\frac{\partial}{\partial t_+}[c_+\epsilon - \xi\,\nabla u]e^{2y} + \frac{\partial}{\partial t_-}[c_-\epsilon + \xi\,\nabla u] = 0, \tag{88}$$

$$\frac{\partial}{\partial t_+}[c_-\epsilon + \xi\,\nabla u] + \frac{\partial}{\partial t_-}[c_+\epsilon - \xi\,\nabla u]e^{-2y} = 0, \tag{89}$$

where $c_\pm \equiv 1 \pm c_s^2$ and $\nabla u \equiv \partial u^0/\partial t + \partial u^3/\partial z = e^y\,\partial y/\partial t_+ - e^{-y}\,\partial y/\partial t_-$ is defined to simplify notations and $\xi \equiv \zeta + 4\eta/3$.

For a nonboost-invariant flow, the fluid rapidity y can be related to space-time rapidity as[134]

$$e^{2y} = f\, e^{2\eta_s} = f\,\frac{t_+}{t_-}, \tag{90}$$

where f is a slowly varying function of t_+ and t_-.[134,140] Again we redefine our co-ordinate system in terms of, $y_\pm \equiv \ln(t_\pm/\Delta)$. First. we solve for the ideal case

with this velocity profile, i.e., putting $\xi = 0$ in Eqs. (88) and (89). The evolution of energy density in the case of ideal hydrodynamics is

$$\epsilon_{id} = \epsilon_0 \exp\left[-\frac{c_+^2}{4\,c_s^2}\,(y_+ + y_-) + \frac{c_+ c_-}{2\,c_s^2}\sqrt{y_+\,y_-}\right]. \tag{91}$$

Changing evolution variables to $y_\pm$, we see that Eqs. (88) and (89) lead to

$$f\,\frac{\partial \epsilon}{\partial y_+} + \frac{\partial \epsilon}{\partial y_-} + \frac{1+f}{2}\left[c_+\epsilon - \frac{\xi}{\Delta}\,e^{-(y_+ + y_-)/2}\right] = 0. \tag{92}$$

Here we have assumed that the form of f does not vary from that one obtains following Landau's prescription in the ideal case i.e., $f = \sqrt{y_+/y_-}$. The evolution equations should have an even parity i.e., invariant under $y_+ \leftrightarrow y_-$ interchange due to symmetry of the colliding system which is there in Eq. (92). Therefore, the other combination (Eqs. (88) and (89)) has been neglected. Hence, the solution of Eq. (92) should lead to the evolution of energy density for viscous Landau flow in symmetric nucleus–nucleus collisions.

We assume the ratio ξ/s to be a constant where s is the entropy density. While this is a valid assumption in conformal case, it is not be strictly true for a nonconformal system. Therefore, for the case of constant ξ/s, one can write $\xi = \alpha\,\epsilon^{1/(1+c_s^2)} = \alpha\,\epsilon^{1/c_+}$, where α is a constant. Substituting in Eq. (92) and rearranging, we get

$$f\frac{\partial \epsilon}{\partial y_+} + \frac{\partial \epsilon}{\partial y_-} = \frac{1+f}{2}\left[\frac{\alpha}{\Delta}\epsilon^{\frac{1}{c_+}} e^{-\frac{1}{2}(y_+ + y_-)} - c_+\epsilon\right]. \tag{93}$$

Using method of characteristics, we get

$$\frac{dy_+}{f} = \frac{dy_-}{1} = \frac{2\,d\epsilon}{(1+f)\left[\frac{\alpha}{\Delta}\epsilon^{\frac{1}{c_+}} e^{-\frac{1}{2}(y_+ + y_-)} - c_+\epsilon\right]}. \tag{94}$$

The above equations can be solved analytically to obtain the final form of ϵ,[153]

$$\epsilon = \left[g(\alpha)\,\epsilon_{id}^{c_s^2/c_+} - \frac{c_s^2\,\alpha}{c_+ c_- \Delta}\,e^{-(y_+ + y_-)/2}\right]^{\frac{c_+}{c_s^2}}, \tag{95}$$

where $g(\alpha)$ is an arbitrary function of α such that $g(0) = 1$. It is easy to see that the above form of energy density indeed satisfies Eq. (92).

12.3. *Rapidity distribution*

In Landau's model, a fast longitudinal expansion is followed by a slower expansion with constant acceleration in the transverse direction.[134,140] In this picture, the transverse expansion does not get any correction from viscosity so as the freeze-out time. Following Landau's freeze-out criteria[134,140] and considering the transverse

expansion using the nonconformal equation of state, the constant time freeze-out time is given by

$$t_{\rm FO} = a\sqrt{\frac{1+c_s^2}{c_s^2}}\cosh y. \tag{96}$$

At the freeze-out hypersurface, y takes the form $y_\pm = y_b' \pm y$, where $y_b' \equiv \frac{1}{2}\ln[c_+/(4c_s^2)] + y_b$ and $y_b \equiv \ln(\sqrt{s_{\rm NN}}/m_p)$ is the beam rapidity and m_p is mass of the proton.[140] One can neglect the term proportional to α in Eq. (95) at freeze-out in the first approximation because this term is exponentially suppressed by large rapidity value at freeze-out.

The ratio of entropy density to number density, s/n, is a conserved quantity in ideal evolution. As entropy density does not get any direct correction from dissipative term in the relativistic Navier–Stokes equation, i.e., $s \sim \epsilon^{1/c_+}$, s/n is approximately conserved for viscous evolution. Neglecting the viscous correction to energy density, the final expression for rapidity distribution turns out to be proportional to entropy density which is given by

$$\frac{dN}{dy} \sim \exp\left(\frac{c_-}{2c_s^2}\sqrt{{y_b'}^2 - y^2}\right). \tag{97}$$

By setting $c_s^2 = 1/3$, the ideal rapidity spectrum for conformal system can be recovered.[134,140] We note that $g(\alpha)$ contributes as an overall multiplicative factor and can be absorbed in the volume factor for calculation of the spectra. Therefore, $g(\alpha)$ does not appear as an additional fitting parameter.

12.4. *Results and discussion*

In Fig. 38, we show rapidity spectrum of pions fitted using Eq. (97) for $\sqrt{s_{\rm NN}} = 200$, 12.3 and 3.83 GeV. The fitting is performed by keeping the overall normalization and c_s^2 as free parameters in a minimization routine. We see that a better fit is obtained using the nonconformal solutions for these collision energies. We have also fitted the rapidity spectrum of pions for $\sqrt{s_{\rm NN}} = 17.3$, 8.76, 7.62, 6.27, 4.29, 3.28 and 2.63 GeV and found that there is an overall better fit with solutions from nonconformal equation of state.

We note that in Fig. 38, the conformal case is above the nonconformal one for small y and below that at large y for $\sqrt{s_{\rm NN}} = 200$ GeV. However, as one moves to smaller energies an opposite trend is observed. This is due to the fact that an unconstrained fit at $\sqrt{s_{\rm NN}} = 200$ GeV leads to $c_s^2 > 1/3$ which is not reasonable. At such high energy, boost-invariance is a good symmetry and therefore, Landau model with broken boost invariance is unable to reproduce the data with reasonable parameter values. In such cases, one should perform a constrained fit such that $c_s^2 \leq 1/3$ for all fitting range.

In Fig. 39, we show a plot of squared speed of sound, extracted by fitting the pion rapidity spectra using Eq. (97), over various collision energies (red solid line).

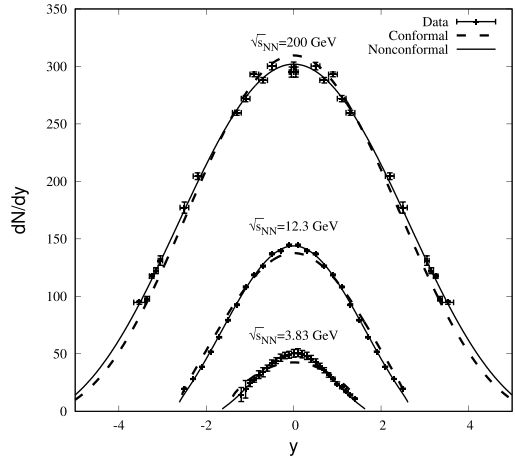

Fig. 38. Rapidity spectrum of pions fitted using Eq. (97) (solid curves) for three representative collision energies: $\sqrt{s_{\rm NN}} = 200$, 12.3 and 3.83 GeV. Also shown are the fit result using conformal solution of Landau hydrodynamics[140] (dashed curves) and the experimental results (with error bars). Experimental data are from Refs. 154, 155, 156, 136.

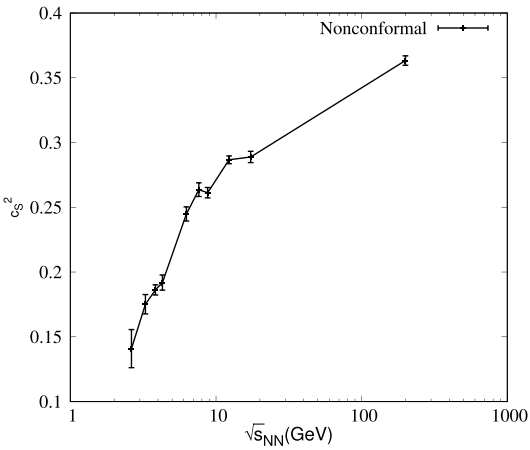

Fig. 39. Squared speed of sound, extracted by fitting the pion rapidity spectra using the rapidity distribution obtained using nonconformal solution given in Eq. (97). The error bars correspond to those obtained from chi-square fit on the fit parameters.

We see that at $\sqrt{s_{\rm NN}} = 200\,\text{GeV}$, the fitted value of c_s^2 is slightly larger than 1/3 which has also been observed in Refs. 157 and 158. On the other hand, with lower collision energies, we find a monotonic decrease in the extracted value of c_s^2. For lower collision energies, rapidity spectra will provide a testing ground for determination of the correct value of c_s^2 and hence the equation of state.

For high-energy heavy-ion collisions, such as those at RHIC and LHC, one expects the boost-invariance to be a good symmetry for evolution. This is the reason why Bjorken's boost invariant symmetry is extensively applied to model relativistic

heavy-ion collisions. However, as one goes to lower collisions energies, Bjorken symmetry is broken and one has to consider evolution which is dependent on space-time rapidity. Landau model provides an analytical framework to study the dynamics at low collision energies. Here, we have derived the evolution of the fireball with broken conformal symmetry as well as in presence of viscosity. Using the present analytical solution, one can directly extract the value of c_s^2 of QCD medium formed in heavy-ion collisions by analyzing the rapidity spectrum of produced particles. We claim that the rapidity spectra will be important for determination of the correct equation of state.

13. Viscous Corrections to the Coalescence Model for Hadron Production in Relativistic Heavy-Ion Collisions

Sumana Bhattacharyya, Amaresh Jaiswal

We incorporate viscous corrections to the coalescence model for hadron production from a dissipative quark–gluon plasma. We use this viscous coalescence model to fit the spectra and elliptic flow of hadrons for 2.76 TeV Pb–Pb collisions at LHC.

13.1. *Introduction*

Recombination models, along with fragmentation processes, have been used quite successfully to describe hadronization in heavy-ion collisions. Coalescence model in heavy-ion collision is mainly based on an instantaneous projection of thermalized quark states, those are close to each other both in space and in momentum space, onto hadron states.[159] This model characterize numerous salient features of hadronization in heavy-ion collisions, including baryon enhancement[160] and the robust scaling of the elliptic flow with the number of valence quarks.[161] It has been argued that the flow anisotropy originates in the partonic phase and it obeys a simple valence quark scaling for low transverse momentum, that naturally arises from a recombination model.[162,163] However, it is assumed in this model that densely populated phase-space distribution of partons do not change with hadronization, there are no dynamical thermal gluons in the medium and QCD plays a background part. Under these assumptions, temperature merely plays any part than scale the momentum. Quark numbers do not change with temperature. Here we modify the coalescence model to incorporate viscous corrections in the distribution function. We subsequently use this viscous coalescence model for hadron production from a dissipative quark–gluon plasma and to fit the spectra and elliptic flow of hadrons for 2.76 TeV Pb–Pb collisions at LHC.

13.2. *Formalism*

In order to consider a boost invariant framework, it is easier to work in the Milne co-ordinate system where

$$\tau = \sqrt{t^2 - z^2}, \quad \eta_s = \tanh^{-1}(z/t), \quad r = \sqrt{x^2 + y^2}, \quad \varphi = \text{atan2}(y, x). \quad (98)$$

The metric tensor for this co-ordinate system is $g_{\mu\nu} = \mathrm{diag}(1, -\tau^2, -1, -r^2)$. Boost invariance and rotational invariance implies $u^{\varphi} = u^{\eta_s} = 0$. In this model, we further assume that the particle freeze-out happens at a proper time τ_f having a constant temperature T_f and uniform matter distribution, in the transverse plane. In summary, the hydrodynamic fields are parametrized as

$$T = T_f, \quad u^r = \gamma_T \beta_T, \quad u^{\varphi} = u^{\eta_s} = 0, \quad u^{\tau} = \gamma_T, \tag{99}$$

where R is the transverse radius of the fireball at freeze-out, $\gamma_T = 1/\sqrt{1-\beta_T^2}$ is the Lorentz factor in the transverse direction and β_T is the transverse expansion velocity.

For central collisions, a power-law relation for transverse velocity flow profile leads to

$$\beta_T = \beta_0 \left(\frac{r}{R}\right)^m, \tag{100}$$

where β_0 is the maximum transverse velocity. For noncentral collisions, the transverse fluid velocity profile can be parametrized as

$$\beta_T = \beta_0 \left(\frac{r}{R}\right)^m \left[1 + 2\sum_{n=1}^{\infty} \beta_n \cos[n(\varphi - \psi_n)]\right], \tag{101}$$

where β_n are the strength of flow anisotropies in the transverse direction and ψ_n are the angles between the x-axis and the major axis of the participant distribution. However, in the present calculation, we can only consider elliptic flow and treat β_2 as a parameter.

13.3. *Viscous correction*

The distribution function with viscous correction is written as $f = f_0 + \delta f$. The equilibrium distribution function is given by

$$f_0 = \frac{1}{\exp(u_\mu p^\mu / T) + a}, \tag{102}$$

where $a = +1$ for baryons and $a = -1$ mesons.

Approximating the shear stress tensor with its first-order relativistic Navier–Stokes expression, $\pi_{\alpha\beta} = 2\eta \nabla_{\langle\alpha} u_{\beta\rangle}$, the expression for the Grad's 14-moment approximation reduces to[164,165]

$$\delta f_G^{(1)} = \frac{f_0 \tilde{f}_0}{T^3} \left(\frac{\eta}{s}\right) p^\alpha p^\beta \nabla_{\langle\alpha} u_{\beta\rangle}, \tag{103}$$

whereas that due to the Chapman–Enskog method leads to[166,167]

$$\delta f_{CE}^{(1)} = \frac{5 f_0 \tilde{f}_0}{T^2 (u \cdot p)} \left(\frac{\eta}{s}\right) p^\alpha p^\beta \nabla_{\langle\alpha} u_{\beta\rangle}. \tag{104}$$

Here η is the coefficient of shear viscosity, $s = (\epsilon + P)/T$ is the entropy density and the angular brackets denote traceless symmetric projection orthogonal to the fluid four-velocity.

For a particle at the space-time point $(\tau, \eta_s, r, \varphi)$ with the four momentum $p^\mu = (m_T \cosh y,\, p_T \cos\varphi_p,\, p_T \sin\varphi_p,\, m_T \sinh y)$, we get

$$p_\tau = m_T \cosh(y - \eta_s), \quad p_{\eta_s} = -\tau m_T \sinh(y - \eta_s), \tag{105}$$

$$p_r = -p_T \cos(\varphi_p - \varphi), \quad p_\varphi = -r p_T \sin(\varphi_p - \varphi). \tag{106}$$

Next step is to obtain $\nabla_{\langle\alpha} u_{\beta\rangle}$. We work in Milne co-ordinate system with the metric tensor $g_{\mu\nu} = \mathrm{diag}(1, -\tau^2, -1, -r^2)$. Therefore, the inverse metric tensor is $g^{\mu\nu} = \mathrm{diag}(1, -1/\tau^2, -1, -1/r^2)$, its determinant g is $\sqrt{-g} = \tau r$ and the nonvanishing Christoffel symbols are $\Gamma^\tau_{\eta_s\eta_s} = \tau$, $\Gamma^{\eta_s}_{\tau\eta_s} = 1/\tau$, $\Gamma^r_{\varphi\varphi} = -r$, and $\Gamma^\varphi_{r\varphi} = 1/r$. Using the parametrization of the fluid velocity given in Eq. (101), we get

$$\Delta^{r\varphi} = 0, \quad \Delta^{\varphi\varphi} = -\frac{1}{r^2}, \quad \Delta^{rr} = -1 - (u^r)^2, \tag{107}$$

where $\Delta^{\mu\nu} \equiv g^{\mu\nu} - u^\mu u^\nu$ is the projection operator orthogonal to the fluid four-velocity. For the derivatives of the velocity, we get

$$\partial_r u^r = \frac{m\, u^r\, (u^\tau)^2}{r}, \quad \partial_\varphi u^r = -2\,(u^\tau)^3\, \beta_0 \left(\frac{r}{R}\right)^m \sum_{n=1}^{\infty} n\, \beta_n \sin[n(\varphi - \psi_n)]. \tag{108}$$

To fix the time derivatives of the fluid velocity, we assume that if the particles are freezing-out, they are free streaming, which means that $Du^\mu = 0$. Here $D \equiv u^\mu d_\mu$ is the co-moving derivative and d_μ is the covariant derivative. With this prescription, we have

$$\partial_\tau u^\varphi = 0, \quad \partial_\tau u^r = -\beta_T\, \partial_r u^r = -m\, \frac{(u^r)^2\, (u^\tau)^2}{r\, u^\tau}, \quad \partial_\tau u^\tau = \beta_T\, \partial_\tau u^r = -m\, \frac{(u^r)^3}{r}, \tag{109}$$

where $\beta_T = u^r/u^\tau$ is the radial velocity in the transverse plane. The expansion scalar is

$$\frac{1}{\sqrt{-g}} \partial_\mu (\sqrt{-g} u^\mu) = \frac{u^\tau}{\tau} + \frac{u^r}{r} + \partial_\varphi u^\varphi + \partial_r u^r + \partial_\tau u^\tau = \frac{u^\tau}{\tau} + (m+1)\frac{u^r}{r}. \tag{110}$$

Assuming boost invariance, the spatial components of the viscous tensor are given by

$$\begin{aligned} r\nabla^{\langle r} u^{\varphi\rangle} &= -\frac{r}{2}\partial_r u^\varphi - \frac{1}{2r}\partial_\varphi u^r - \frac{r}{2} u^r Du^\varphi - \frac{r}{2} u^\varphi Du^r - \frac{1}{3} r \Delta^{r\varphi} \frac{1}{\sqrt{-g}} \partial_\mu (\sqrt{-g} u^\mu) \\ &= (u^\tau)^3\, \frac{\beta_0}{r} \left(\frac{r}{R}\right)^m \sum_{n=1}^{\infty} n\, \beta_n \sin[n(\varphi - \psi_n)], \end{aligned} \tag{111}$$

$$\begin{aligned} r^2 \nabla^{\langle\varphi} u^{\varphi\rangle} &= -\partial_\varphi u^\varphi - \frac{u^r}{r} - r^2 u^\varphi Du^\varphi - \frac{1}{3} r^2 \Delta^{\varphi\varphi} \frac{1}{\sqrt{-g}} \partial_\mu (\sqrt{-g} u^\mu) \\ &= \frac{1}{3}\left[\frac{u^\tau}{\tau} + (m-2)\frac{u^r}{r}\right], \end{aligned} \tag{112}$$

$$\nabla^{\langle r}u^{r\rangle} = -\partial_r u^r - u^r Du^r - \frac{1}{3}\Delta^{rr}\frac{1}{\sqrt{-g}}\partial_\mu(\sqrt{-g}u^\mu)$$
$$= \frac{(u^\tau)^2}{3}\left[\frac{u^\tau}{\tau} + (1-2m)\frac{u^r}{r}\right], \tag{113}$$

where we have used the fact that $(u^\tau)^2 = 1 + (u^r)^2$. Therefore,

$$\tau^2\nabla^{\langle\eta_s}u^{\eta_s\rangle} = -\frac{u^\tau}{\tau} + \frac{1}{3}\frac{1}{\sqrt{-g}}\partial_\mu(\sqrt{-g}u^\mu) = \frac{1}{3}\left[(m+1)\frac{u^r}{r} - 2\frac{u^\tau}{\tau}\right], \tag{114}$$

$$\nabla^{\langle r}u^{\eta_s\rangle} = \nabla^{\langle\varphi}u^{\eta_s\rangle} = 0. \tag{115}$$

To obtain the temporal components of the viscous stress energy tensor, we use the Landau frame condition, $\nabla^{\langle\alpha}u^{\beta\rangle}u_\beta = 0$.

$$\nabla^{\langle\tau}u^{\tau\rangle}u_\tau + \nabla^{\langle\tau}u^{r\rangle}u_r = 0 \Rightarrow \nabla^{\langle\tau}u^{\tau\rangle} = \beta_T\nabla^{\langle\tau}u^{r\rangle}, \tag{116}$$

$$\nabla^{\langle\eta_s}u^{\tau\rangle}u_\tau + \nabla^{\langle\eta_s}u^{r\rangle}u_r = 0 \Rightarrow \nabla^{\langle\tau}u^{\eta_s\rangle} = 0, \tag{117}$$

$$\nabla^{\langle r}u^{\tau\rangle}u_\tau + \nabla^{\langle r}u^{r\rangle}u_r = 0 \Rightarrow \nabla^{\langle\tau}u^{r\rangle} = \beta_T\nabla^{\langle r}u^{r\rangle}, \tag{118}$$

$$\nabla^{\langle\varphi}u^{\tau\rangle}u_\tau + \nabla^{\langle\varphi}u^{r\rangle}u_r = 0 \Rightarrow \nabla^{\langle\tau}u^{\varphi\rangle} = \beta_T\nabla^{\langle r}u^{\varphi\rangle}. \tag{119}$$

Therefore, from Eqs. (116) and (118), we see that

$$\nabla^{\langle\tau}u^{\tau\rangle} = \beta_T\nabla^{\langle\tau}u^{r\rangle} = \beta_T^2\nabla^{\langle r}u^{r\rangle} = \frac{(u^r)^2}{3}\left[\frac{u^\tau}{\tau} + (1-2m)\frac{u^r}{r}\right]. \tag{120}$$

Next, in order to verify our algebra, we confirm that the viscous stress tensor is traceless, i.e., $g_{\mu\nu}\nabla^{\langle\mu}u^{\nu\rangle} = 0$. Using Eqs. (112), (113), (114) and (120)

$$g_{\mu\nu}\nabla^{\langle\mu}u^{\nu\rangle} = \nabla^{\langle\tau}u^{\tau\rangle} - \tau^2\nabla^{\langle\eta_s}u^{\eta_s\rangle} - \nabla^{\langle r}u^{r\rangle} - r^2\nabla^{\langle\varphi}u^{\varphi\rangle} = 0 \tag{121}$$

The components of viscous tensor are collected below for quick reference,

$$\nabla^{\langle\tau}u^{\tau\rangle} = \frac{(u^r)^2}{3}\left[\frac{u^\tau}{\tau} + (1-2m)\frac{u^r}{r}\right],$$

$$\nabla^{\langle\eta_s}u^{\eta_s\rangle} = \frac{1}{3\tau^2}\left[(m+1)\frac{u^r}{r} - 2\frac{u^\tau}{\tau}\right],$$

$$\nabla^{\langle r}u^{r\rangle} = \frac{(u^\tau)^2}{3}\left[\frac{u^\tau}{\tau} + (1-2m)\frac{u^r}{r}\right],$$

$$\nabla^{\langle\varphi}u^{\varphi\rangle} = \frac{1}{3r^2}\left[\frac{u^\tau}{\tau} + (m-2)\frac{u^r}{r}\right],$$

$$\nabla^{\langle\tau}u^{r\rangle} = \beta_T\nabla^{\langle r}u^{r\rangle},$$

$$\nabla^{\langle r}u^{\varphi\rangle} = (u^\tau)^3\frac{\beta_0}{r^2}\left(\frac{r}{R}\right)^m\sum_{n=1}^{\infty}n\,\beta_n\sin[n(\varphi-\psi_n)],$$

$$\nabla^{\langle\tau}u^{\varphi\rangle} = \beta_T\nabla^{\langle r}u^{\varphi\rangle}.$$

In the above equations, τ is the freeze-out time which we will now denote as τ_f.

13.4. *Results and discussions*

The parameters that need to be fit are T_f, β_0, m, τ_f, R, β_n and η/s. Out of these, T_f, β_0 and m are sensitive to the slope of the transverse momentum spectra. The magnitude of the spectra is sensitive to τ_f and R. However, since we are considering viscous corrections, τ_f might also affect the anisotropic flow v_n. The key parameters that are actually needed to fit v_n are β_n and η/s.

The freeze-out hyper-surface is $d\Sigma_\mu = (\tau d\eta_s\, r dr\, d\varphi,\, 0,\, 0,\, 0)$, and therefore, the integration measure is given by

$$p^\mu d\Sigma_\mu = m_T \cosh(y - \eta_s)\tau d\eta_s\, r dr\, d\varphi. \tag{122}$$

Momentum distribution of number density is given by

$$\frac{d^2N}{d^2p_T dy} = \frac{1}{(2\pi)^3}\int_0^R r dr \int_0^{2\pi} d\varphi \int_{-\infty}^{\infty} \tau d\eta_s m_T \cosh(y - \eta_s)(f_0 + \delta f). \tag{123}$$

For Coalescence Model distribution, functions are modified as, $f(u, E, \vec{p}) \rightarrow$

$$\begin{cases} f\left(u, E, \dfrac{\vec{p}}{2}\right) f\left(u, E, \dfrac{\vec{p}}{2}\right) & \text{meson,} \\ f\left(u, E, \dfrac{\vec{p}}{3}\right) f\left(u, E, \dfrac{\vec{p}}{3}\right) f\left(u, E, \dfrac{\vec{p}}{3}\right) & \text{baryon.} \end{cases} \tag{124}$$

The anisotropy flow is given by

$$v_n(p_T) = \frac{\displaystyle\int_{-\pi}^{\pi} d\varphi_p \cos[n(\varphi_p - \psi_n)] \frac{dN}{dy p_T dp_T d\varphi_p}}{\displaystyle\int_{-\pi}^{\pi} \frac{dN}{dy p_T dp_T d\varphi_p}}, \tag{125}$$

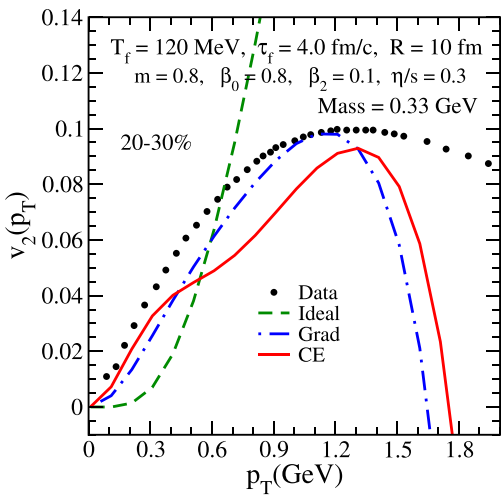

Fig. 40. Elliptic flow v_2 as a function of the transverse momentum p_T of pions at LHC for 20–30% centrality.

where ψ_n is the event plane angle. To calculate elliptic flow parameter $v_2(p_T)$, we use (123) in the above equation and perform the integral numerically.

Figure 40 shows our results obtained for elliptic flow as a function of transverse momentum at LHC for 20–30% centrality class. We see that a reasonable agreement is obtained by including viscous correction in the coalescence model. The fit parameters, we get from this analysis, are in reasonable agreement with the literature.[132,168]

14. Shear Viscosity and Chemical Equilibration in QGP

V. Sreekanth

By using various temperature-dependent η/s prescriptions, we study the chemical equilibration of the hot quark–gluon matter created in the early stages of heavy-ion collisions using causal second-order viscous hydrodynamics. Chemical equilibration is studied by introducing fugacity parameters in parton distribution functions. Solving the rate equations, energy and viscous evolution equations within scale invariant Björken hydrodynamics, we show that the equilibration gets delayed because of slower cooling rate of the fireball in presence of viscosity. Furthermore, we studied shear-induced cavitation–negative pressure scenarios during expansion, in presence of chemical nonequilibrium. It has been observed that cavitation sets in early times for the shear viscosity prescriptions used, invalidating the hydrodynamical modeling.

14.1. *Introduction*

Properties of the quark–gluon plasma (QGP) formed in the early stages of relativistic heavy-ion collisions are under intense investigation. Hydrodynamical models explaining the expansion of the strongly coupled QGP has been met with great success. Several nonequilibrium effects are studied in this context.[169] Particularly of our interest is that of chemical equilibration of the QGP produced. It is a matter of investigation whether the QGP produced achieves thermal, mechanical and chemical equilibration. Assuming thermal and mechanical equilibration, we study chemical equilibration of the fireball. In doing so we follow Ref. 170, where the nonequilibrium measure is prescribed through the introduction of fugacities in the particle distribution functions. Essentially, one studies the evolution of quark (antiquark) and gluon fugacities (λ_i) by means of relativistic fluid dynamical equations coupled to the rate equations; once the initial time, temperature and species number densities are provided.

Shear viscosity of QGP formed in RHIC created huge interest in the scientific community due to its extreme small value (to be precise $\eta/s \sim 1/4\pi$). In order to understand the equilibration dynamics of viscous quark–gluon matter, one needs to use the causal dissipative hydrodynamics instead of familiar first-order Navier–Stoke's equations to avoid acausal issues.[165–167,171–173] The study of evolution of

chemically equilibrating QGP with constant shear viscosity within causal second-order viscous hydrodynamics has shown distinct properties with possible bearings on signals.[174] While considering higher energy collisions, temperature-dependent shear viscosity prescriptions are considered, due to the fact that in general physical systems show strong temperature dependence for η/s. On the other hand, certain temperature-dependent shear viscosity prescriptions result in negative pressure scenarios known as cavitation in the early stages of the fluid dynamical evolution itself.[175] Cavitation in such situations is problematic and even questions the validity of hydrodynamical modeling used and is known to affect the signals.[176–178] We attempt to study these temperature-dependent shear viscosity-induced cavitation scenarios under chemical nonequilibrium for an expanding quark–gluon matter.

14.2. *Model*

We denote the single-particle distribution function of parton gas with momentum isotropy as[170]

$$f_i \simeq \lambda_i (e^{\beta\cdot p} \pm 1)^{-1}, \tag{126}$$

where $\beta \cdot p = \beta^\mu p_\mu = T^{-1} u^\mu p_\mu$, with u^μ being the four-velocity in the comoving frame. Note that the fugacities lie between the values zero and one, with latter denoting complete chemical equilibration. Using the above definition of distribution functions, number (n) and energy (ε) densities and pressure (P) of the system with quarks (q), anti-quarks ($\bar{q}$) and gluons (g) can be calculated as[170]

$$\begin{aligned} n &= (a_1 \lambda_g + b_1[\lambda_q + \lambda_{\bar{q}}])\, T^3, \\ \varepsilon &= 3P = (a_2 \lambda_g + b_2[\lambda_q + \lambda_{\bar{q}}]) T^4, \end{aligned} \tag{127}$$

where $a_1 = \frac{16\zeta(3)}{\pi^2}, b_1 = \frac{9\zeta(3) N_f}{2\pi^2}, a_2 = \frac{8\pi^2}{15}, b_2 = \frac{7\pi^2 N_f}{40}$ with N_f being the number of dynamical quark flavors. Note that for the baryonless QGP under consideration, we have $\lambda_q = \lambda_{\bar{q}}$.

There are several formulations of second-order hydrodynamics and it is an active field of ongoing research.[81] In this causal theory, shear stress $\pi^{\mu\nu}$ dynamically evolves with a characteristic relaxation time τ_π. We use the equation for shear evolution and relaxation time $\tau_\pi = \frac{3\eta}{sT}$ from Ref. 179. For a longitudinal boost invariant Björken flow, the energy equation and shear pressure $\Phi = \pi^{00} - \pi^{zz}$ evolution becomes[170,174]

$$\frac{\dot{T}}{T} + \frac{1}{3\tau} + \frac{1}{4} \frac{a_2 \dot{\lambda}_g + 2 b_2 \dot{\lambda}_q}{a_2 \lambda_g + 2 b_2 \lambda_q} = \frac{\Phi}{4\tau} \frac{1}{(a_2 \lambda_g + 2 b_2 \lambda_q) T^4} \tag{128}$$

$$\dot{\Phi} + \frac{\Phi}{\tau_\pi} = \frac{8}{27\tau} (a_2 \lambda_g + 2 b_2 \lambda_q) T^4. \tag{129}$$

In all the equations, proper time derivative is denoted by the dot. There are several temperature-dependent shear viscosity prescriptions available[175] and we use the one used in Ref. 179: $(\eta/s)_1 = 0.2 + 0.3 \frac{T - T_{\rm chem}}{T_{\rm chem}}$ (with $T_{\rm chem} = 0.165\,{\rm GeV}$) which

is known to result in cavitation, in the equilibrium case within one-dimensional Bjorken flow, at early times itself.[175]

Under chemical nonequilibrium, above set of equations have to be solved together with the parton density evolution equations prescribed through master equations. By considering the relevant reactions, $gg \longleftrightarrow ggg$ and $gg \longleftrightarrow q\bar{q}$, in the context of baryonless QGP, rate equations for the fugacities can be written in Björken flow as[170,174]

$$\frac{\dot{\lambda_g}}{\lambda_g} + 3\frac{\dot{T}}{T} + \frac{1}{\tau} = R_{gg\to ggg}\,(1-\lambda_g) - 2R_{g\to q}\left(1 - \frac{\lambda_q^2}{\lambda_g^2}\right), \tag{130}$$

$$\frac{\dot{\lambda_q}}{\lambda_q} + 3\frac{\dot{T}}{T} + \frac{1}{\tau} = R_{g\to q}\frac{a_1}{b_1}\left(\frac{\lambda_g}{\lambda_q} - \frac{\lambda_q}{\lambda_g}\right). \tag{131}$$

Here the rates are given as $R_{gg\to ggg} = 2.1\alpha_s^2 T(2\lambda_g - \lambda_g^2)^{1/2}$ and $R_{g\to q} = 0.24N_f\alpha_s^2\lambda_g T\,ln(5.5/\lambda_g)$, with α_s being the strong coupling constant.[170]

Now Eqs. (128)–(131) describe the longitudinally expanding chemically equilibrating viscous hot QGP[174] and it can be solved numerically once all the initial conditions are given. While evolving the hydrodynamical code, one needs to make sure that the effective pressures — which has contributions from viscosities remain positive. This effective pressure of the expanding fireball in the longitudinal direction is given by[175]

$$P_z = P - \Phi, \tag{132}$$

which denotes the deviation from equilibrium pressure due to dissipative effects. The cavitation condition is then given as $P_z = 0$, which in our case readily translates to

$$[a_2\lambda_g(\tau) + 2b_2\lambda_q(\tau)]T(\tau)^4 - 3\Phi(\tau) = 0. \tag{133}$$

14.3. *Results and discussions*

With the initial conditions relevant for LHC energies, we evolve the system, while monitoring the effective longitudinal pressure. The initial values taken are $\lambda_g^0 = 0.08$, $\lambda_q^0 = 0.02$, $T_0 = 0.570\,\text{GeV}$ and $\tau_0 = 0.7\,\text{fm/c}$.[170] We evolve the system till its temperature drops to $T_c = .180\,\text{GeV}$. Also we set minimum value of shear stress at the beginning: $\Phi(\tau_0) = 0$.

First, we plot the evolution of quark and gluon fugacities in the case of temperature-dependent η/s in Fig. 41. It is observed that the equilibration process is delayed in the presence of viscosity. Now we plot the longitudinal pressure in Fig. 42. It can be seen that in the early times itself, system reaches cavitation triggered by the peak in shear stress value. It needs to be noted that such initial temperature and time had resulted in cavitations in chemically equilibrated case too.[175] Finally, we look into possible combinations of initial times and temperatures for which, under the considered chemical nonequilibrium scenario, cavitations

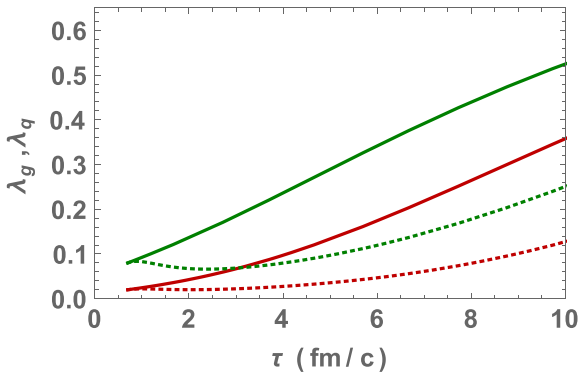

Fig. 41. (Color online) Evolution of fugacities in the presence of temperature-dependent shear viscosity. Green (red) line denotes gluon (quark) fugacity. Dotted lines denote the case with viscosity while thick lines correspond to zero viscosity.

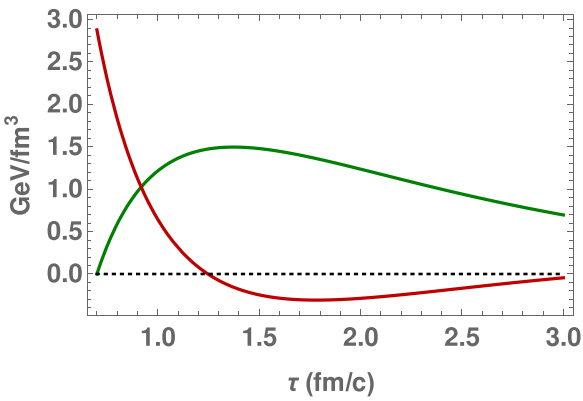

Fig. 42. (Color online) Evolution of longitudinal pressure P_z (red curve) and shear stress Φ (green curve). One can see $Pz = 0$ at early times itself.

occur. It is clear from Fig. 43 that in order to avoid negative effective pressure scenarios, one needs to go for large initial time and relatively low initial temperatures. This might not be compatible with the usual early times and high temperatures associated with the chemical equilibration studies. It must also be noted that the occurrence of cavitation in early times will force us to look for alternate ways to understand the evolution of the system and freezeout. On the other hand, the successful statistical hadronization models predict a chemical freezeout in the vicinity of T_c; thus such an early time cavitation observed here, perhaps, point toward nonapplicability of such high valued viscosity prescriptions used in the literature.

14.4. *Summary and conclusions*

In conclusion, we have studied the effect of temperature-dependent η/s in the chemical equilibration of hot baryonless QGP produced in high energy heavy-ion

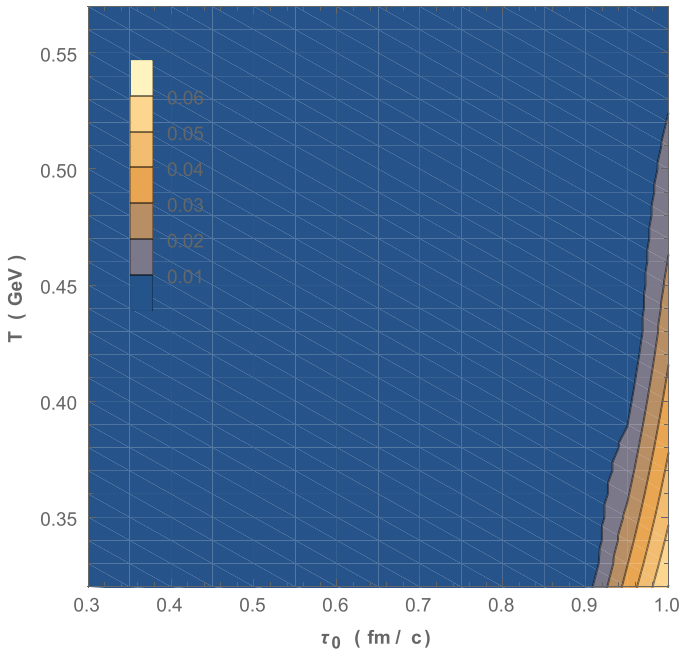

Fig. 43. Cavitation scenarios for various initial conditions. Darkest region denotes the existence of $P_z = 0$.

collisions. It has observed that equilibration gets delayed because of slower cooling rate of the fireball in presence of viscosity. Further, it was seen that cavitations set in rather early time itself making the hydrodynamical evolution model into trouble. It is interesting to note that cavitation scenarios are not getting washed away with the introduction of chemical nonequilibration in the problem. One can also think of giving a bound to shear viscosity by assuming that the cavitations do not occur. This work is in progress and will be reported elsewhere.[180]

15. First-Order Dissipative Hydrodynamics from an Effective Covariant Kinetic Theory

Samapan Bhadury, Manu Kurian, Vinod Chandra, Amaresh Jaiswal

Relativistic Dissipative Hydrodynamics has been used successfully as a tool to describe the space-time evolution of hot QCD matter created in high energy heavy-ion collisions. We will describe how the hot QCD medium can be modeled using a quasiparticle picture that is consistent with the equation of state of the system, estimated from Lattice QCD. In this model, we investigate evolution equation for the shear stress tensor, the bulk viscous pressure and the charge current under first-order dissipative relativistic hydrodynamic. This shows some modification in the behavior of the transport coefficients.

15.1. *Introduction*

Collision of two heavy nuclei with ultra-relativistic velocities at RHIC and LHC produces a hot QCD medium commonly known as Quark–Gluon–Plasma (QGP). The relativistic dissipative hydrodynamics serves as an efficient theoretical approach to describe the space-time evolution of the created QGP. In this contribution, we study the first-order dissipative evolution equation of the QGP for a nonzero baryon chemical potential and quark mass following a recently proposed effective covariant kinetic theory.[181] We utilize the effective fugacity quasiparticle model (EQPM)[182] to encode the effects of hot QCD equation of state (EoS) in terms of temperature-dependent fugacity parameter. By employing the iterative Chapman–Enskog-like expansion, we solve the relativistic transport equation in presence of an EQPM mean field term under the relaxation time approximation (RTA).[183] We study the ratios of the dissipative quantities with mean field correction at finite baryon chemical potential.

15.2. *Effective covariant kinetic theory*

Under the RTA, the relativistic Boltzmann equation, which describes the change of momentum distribution function of each particle species k, is given by,[181]

$$\tilde{p}_k^\mu \, \partial_\mu f_k(x,\tilde{p}_k) + F_k^\mu (u\cdot\tilde{p}_k)\partial_\mu^{(p)} f_k = -(u\cdot\tilde{p}_k)\frac{\delta f_k}{\tau_R}, \tag{134}$$

where τ_R is the thermal relaxation time and u_μ is the fluid velocity. The mean field force term $F_k^\mu = -\partial_\nu(\delta\omega_k u^\nu u^\mu)$ can be realized from the conservation laws.[181] The covariant form of EQPM distribution function for quarks, antiquarks and gluons at nonzero baryon chemical potential μ_q can be written as

$$f_q^0 = \frac{z_q \exp\left[-\beta(u\cdot p_q - \mu_q)\right]}{1 + z_q \exp\left[-\beta(u\cdot p_q - \mu_q)\right]}, \tag{135}$$

$$f_{\bar{q}}^0 = \frac{z_{\bar{q}} \exp\left[-\beta(u\cdot p_{\bar{q}} + \mu_q)\right]}{1 + z_{\bar{q}} \exp\left[-\beta(u\cdot p_{\bar{q}} + \mu_q)\right]}, \tag{136}$$

$$f_g^0 = \frac{z_g \exp\left[-\beta\, u\cdot p_g\right]}{1 - z_g \exp\left[-\beta\, u\cdot p_g\right]}, \tag{137}$$

where z_q and z_g are the temperature-dependent effective fugacity parameter for quarks and gluons, respectively. It is to be noted that the fugacity parameters z_k that encode the thermal medium effects are same for quarks and antiquarks, *i.e.*, $z_q = z_{\bar{q}}$, in the present context. The dispersion relation relates the dressed (quasiparticle) four-momenta $\tilde{p}_k^\mu$ and the bare particle four-momenta p_k^μ as

$$\tilde{p_k}^\mu = p_k^\mu + \delta\omega_k\, u^\mu, \quad \delta\omega_k = T^2\, \partial_T \ln(z_k), \tag{138}$$

which implies zeroth component of the four-momenta is given by $\tilde{p_k}^0 \equiv \omega_k = E_k + \delta\omega_k$. We assume the system to be near local equilibrium i.e., $f_k = f_k^0 + \delta f_k$

and solve the relativistic Boltzmann equation, employing an iterative Chapman–Enskog like expansion, where $\delta f_k/f_k^0 \ll 1$ and δf_k have the forms,

$$\delta f_q = \tau_R \left[\tilde{p}_q^\gamma \partial_\gamma \beta + \frac{\tilde{p}_q^\gamma}{u\cdot\tilde{p}_q}(\beta\, \tilde{p}_q^\phi \partial_\gamma u_\phi - \partial_\gamma \alpha) - \beta\theta\, \delta\omega_q \right] f_q \tilde{f}_q, \tag{139}$$

$$\delta f_{\bar{q}} = \tau_R \left[\tilde{p}_{\bar{q}}^\gamma \partial_\gamma \beta + \frac{\tilde{p}_{\bar{q}}^\gamma}{u\cdot\tilde{p}_{\bar{q}}}(\beta\, \tilde{p}_{\bar{q}}^\phi \partial_\gamma u_\phi + \partial_\gamma \alpha) - \beta\theta\, \delta\omega_{\bar{q}} \right] f_{\bar{q}} \tilde{f}_{\bar{q}}, \tag{140}$$

$$\delta f_g = \tau_R \left(\tilde{p}_g^\gamma \partial_\gamma \beta + \frac{\beta\, \tilde{p}_g^\gamma\, \tilde{p}_g^\phi}{u\cdot\tilde{p}_g} \partial_\gamma u_\phi - \beta\theta\, \delta\omega_g \right) f_g \tilde{f}_g, \tag{141}$$

where $\theta \equiv \partial_\mu u^\mu$ is the expansion scalar and $\alpha = \beta\mu_q$. The thermal relaxation time τ_R is assumed to be independent of particle four-momenta.

15.3. *Dissipative evolution equation*

Shear stress tensor is defined in terms of the nonequilibrium part of the distribution function δf_k within EQPM as

$$\pi^{\mu\nu} = \sum_k g_k \Delta^{\mu\nu}_{\alpha\beta} \int d\tilde{P}_k \tilde{p}_k^\alpha\, \tilde{p}_k^\beta\, \delta f_k + \sum_k g_k \delta\omega_k \Delta^{\mu\nu}_{\alpha\beta} \int d\tilde{P}_k \tilde{p}_k^\alpha\, \tilde{p}_k^\beta \frac{1}{E_k} \delta f_k, \tag{142}$$

where g_k is the degeneracy factor and $d\tilde{P}_k \equiv \frac{d^3|\vec{\tilde{p}}_k|}{(2\pi)^3\omega_k}$ is the momentum integral factor. We use the two index projection operator $\Delta^{\mu\nu} \equiv g^{\mu\nu} - u^\mu u^\nu$ and a four-index tensor $\Delta^{\mu\nu}_{\alpha\beta} \equiv \frac{1}{2}(\Delta^\mu_\alpha \Delta^\nu_\beta + \Delta^\mu_\beta \Delta^\nu_\alpha) - \frac{1}{3}\Delta^{\mu\nu}\Delta_{\alpha\beta}$ which is a traceless symmetric projection operator orthogonal to the fluid velocity. The bulk viscous pressure Π and the particle diffusion current n^μ can be defined respectively as

$$\Pi = -\frac{1}{3}\sum_k g_k \Delta_{\alpha\beta} \int d\tilde{P}_k\, \tilde{p}_k^\alpha\, \tilde{p}_k^\beta\, \delta f_k - \frac{1}{3}\sum_k g_k\, \delta\omega_k\, \Delta_{\alpha\beta} \int d\tilde{P}_k\, \tilde{p}_k^\alpha\, \tilde{p}_k^\beta \frac{1}{E_k} \delta f_k, \tag{143}$$

$$n^\mu = g_q \Delta^\mu_\alpha \int d\tilde{P}_q\, \tilde{p}_q^\alpha\, (\delta f_q - \delta f_{\bar{q}}) - \delta\omega_q g_q \Delta^\mu_\alpha \int d\tilde{P}_q \tilde{p}_q^\alpha \frac{1}{E_q}(\delta f_q - \delta f_{\bar{q}}). \tag{144}$$

We replace δf_k from Eqs. (139)–(141) and keep terms up to first order in gradients to obtain the Naiver–Stokes like equation as follows:

$$\pi^{\mu\nu} = 2\tau_R \beta_\pi \sigma^{\mu\nu}, \Pi = -\tau_R \beta_\Pi \theta, n^\mu = \tau_R \beta_n \nabla^\mu \alpha, \tag{145}$$

with $\sigma^{\mu\nu} \equiv \Delta^{\mu\nu}_{\alpha\beta}\nabla^\alpha u^\beta$. The dissipative coefficients β_π, β_Π and β_n are expressed in terms of thermodynamic integrals for massive and massless case in Ref. 185.

15.4. *Results and discussions*

The temperature dependence of the ratio of the coefficient of the bulk viscous tensor to that of the shear tensor (β_Π/β_π) at $\mu_q = 0.1$ GeV is shown in Fig. 44. Under RTA, the ratio becomes $\beta_\Pi/\beta_\pi = \zeta/\eta$, where ζ and η are the bulk and shear viscosities of medium. The ratio deceases with the increasing temperature. There

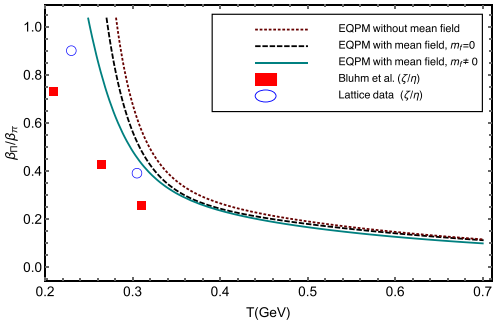

Fig. 44. Evolution of (β_Π/β_π) with temperature and comparison with results in Refs. 184, 86, 88.

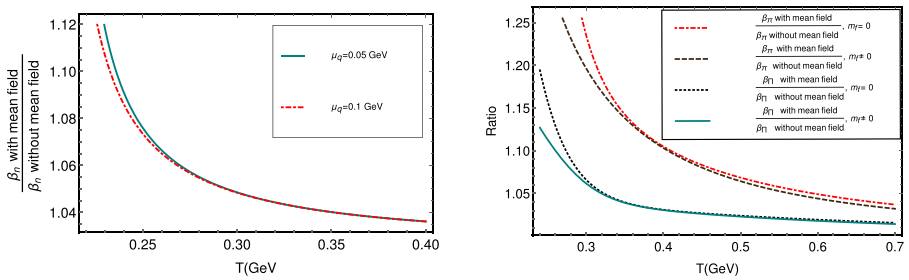

Fig. 45. (Left panel) Temperature dependence of the mean field contribution to the particle diffusion for different quark chemical potentials. (Right panel) The effect of mean field contributions to the coefficients of bulk viscous pressure, shear tensor at $\mu = 0.1$ GeV with and without quark mass correction.

are substantial affects due to quark mass correction and mean field corrections in the low temperature regime close to the transition temperature. In Fig. 45 (left panel), the mean field effects to the first-order coefficient of particle diffusion are shown for different quark chemical potential μ_q. In the low temperature regimes, the effects of quark mass and chemical potential are visible whereas in the higher temperature regimes the mean field contributions are almost independent on m_q and μ_q. This may be attributed to the fact that in low temperature regime when the temperature is of the same order of magnitude as quark mass and chemical potential, the effect of slight changes in these quantities becomes noticeable. On the other hand, at high temperature, there is a separation of scale the effect due to changes in quark mass and chemical potential are not significant. The mean field correction to the transport parameters with binary, elastic collisions at $m_q = 0$ and $\mu_q = 0$ is described in Ref. 181. In Fig. 45 (right panel), the contributions to first-order coefficients of the shear tensor and bulk viscous pressure due to mean field at quark chemical potential $\mu_q = 0.1$ GeV are depicted. Since the mean field corrections at high temperature regimes are negligible, the ratio asymptotically tends to unity. At this juncture, we note that the first-order viscous hydrodynamics theory has issues with causality

due to parabolic nature of the evolution equations. Deriving second-order causal hydrodynamic theory, within the present EQPM framework, is left for future work.

16. Hydrodynamics with Spin and Its Application to Heavy-Ion Collisions

Avdhesh Kumar

We briefly discuss, recently introduced equilibrium Wigner functions for spin 1/2 particles that are used in the semiclassical kinetic equations. In the case of local thermodynamic equilibrium, we outline a procedure to formulate hydrodynamic framework for particles with spin 1/2 based on the semiclassical expansion of Wigner functions. For the case of a boost-invariant and transversely homogeneous expansion of the fireball produced in the heavy-ion collision, we show that this formulation can be used to determine the space-time evolution of the spin polarization and physical observables related to the spin polarization.

16.1. *Introduction*

In the noncentral heavy-ion collisions, nuclei colliding at ultra-relativistic energies carry a very large orbital angular momentum. After the collision, a significant portion of this orbital angular momentum can be retained in the interaction region which can be further transformed from the initial purely orbital form into the spin part. The latter can be reflected in the spin polarization of the emitted particles. Indeed, recently global spin polarization of Λ and $\bar{\Lambda}$ hyperons emitted from the fireball created in the noncentral heavy-ion collisions has been measured by the STAR collaboration.[186,187] This result can be successfully explained by relativistic hydrodynamics (ideal or viscous).[188]

Hydrodynamic models that are used to describe the global spin polarization of Λ and $\bar{\Lambda}$-hyperons make use of the fact that spin polarization effects are governed by thermal vorticity $\varpi_{\mu\nu}$ which is defined by the expression $\varpi_{\mu\nu} = -\frac{1}{2}(\partial_\mu\beta_\nu - \partial_\nu\beta_\mu)$, where β_μ is the ratio of the fluid flow vector U_μ and the local temperature T, i.e., $\beta_\mu = U_\mu/T$.[188–190] There remains, however, a puzzle known as sign problem i.e., the oscillations of the longitudinal polarization of Λ as a function of the azimuthal angle observed by the STAR experiment has an opposite sign with respect to the results obtained using hydrodynamic calculations.[191]

On general thermodynamic grounds, the spin polarization effects are expected to be governed by the tensor $\omega_{\mu\nu}$ namely spin polarization tensor[192] which can be independent of the thermal vorticity $\varpi_{\mu\nu}$. This suggests a new hydrodynamic approach (known as hydrodynamics with spin), which allow the spin polarization tensor to be treated as an independent dynamical variable. Initial steps in this direction have been made in Refs. 193, 194, 192, see also follow-up Refs. 195 and 196 and other related work.[96] In this contribution, we briefly report on our recent works[197–199] where we discuss Wigner function approach to formulate hydrodynamics with spin, for the case of the de Groot, van Leeuwen, and van Weert (GLW)[95] formalism to

study the space-time evolution of spin polarization and related physical observables for the boost invariant Bjorken flow.

16.2. *Equilibrium Wigner functions*

Our starting point are the relativistic distribution functions $f^{\pm}_{rs}(x,p)$ for particles $(+)$ and antiparticles $(-)$ with spin 1/2 at local thermodynamical equilibrium as introduced in Ref. [200]

$$f^{+}_{rs}(x,p) = \frac{1}{2m}\bar{u}_r(p)X^{+}u_s(p), f^{-}_{rs}(x,p) = -\frac{1}{2m}\bar{v}_s(p)X^{-}v_r(p),$$

where m is the (anti-)particle mass, r and s are the spin indices running from 1 to 2 and $u_r(p)$, and $v_r(p)$ are Dirac bispinors. The objects $X^{\pm}$ are the four-by-four matrices defined by the formula

$$X^{\pm} = \exp\left[\pm\xi(x) - \beta_\mu(x)p^\mu \pm \frac{1}{2}\omega_{\mu\nu}\Sigma^{\mu\nu}\right],$$

where $\xi = \frac{\mu}{T}$, with μ and T being the chemical potential and temperature. The quantity $\omega_{\mu\nu}$ is spin polarization tensor while $\Sigma^{\mu\nu} = (i/4)[\gamma^\mu, \gamma^\nu]$ is known as the Dirac spin operator.

By assuming that the spin polarization tensor $\omega_{\mu\nu}$ satisfies the conditions, $\omega_{\mu\nu}\omega^{\mu\nu} \geq 0$ and $\omega_{\mu\nu}\tilde{\omega}^{\mu\nu} = 0$,[194] where $\tilde{\omega}^{\mu\nu} = \frac{1}{2}\epsilon_{\mu\nu\alpha\beta}\omega^{\alpha\beta}$ is the dual spin polarization tensor, we can introduce a new quantity $\zeta = \frac{1}{2}\sqrt{\frac{1}{2}\omega_{\mu\nu}\omega^{\mu\nu}}$ which can be interpreted as the ratio of spin chemical potential Ω and temperature T.[193]

The equilibrium Wigner functions can be constructed by taking the above expressions for $f^{+}_{rs}(x,p)$ and $f^{-}_{rs}(x,p)$ as an input[95]

$$\boldsymbol{W}^{+}_{\rm eq}(x,k) = \frac{1}{2}\sum_{r,s=1}^{2}\int dP\,\delta^{(4)}(k-p)u^r(p)\bar{u}^s(p)f^{+}_{rs}(x,p),$$

$$\boldsymbol{W}^{-}_{\rm eq}(x,k) = -\frac{1}{2}\sum_{r,s=1}^{2}\int dP\,\delta^{(4)}(k+p)v^s(p)\bar{v}^r(p)f^{-}_{rs}(x,p),$$

where dP $= \frac{d^3p}{(2\pi)^3 E_p}$ is the Lorentz invariant measure with $E_p = \sqrt{m^2+\boldsymbol{p}^2}$ being the on-mass-shell particle energy. Four momentum $k^\mu = (k^0, \boldsymbol{k})$ in the Wigner functions is not necessarily on the mass shell.

Being 4×4 matrices that satisfy the relation $\boldsymbol{W}^{\pm}_{\rm eq}(x,k) = \gamma_0\boldsymbol{W}^{\pm}_{\rm eq}(x,k)^\dagger\gamma_0$, equilibrium Wigner functions can always be expressed as combinations of the 16 independent generators of the Clifford algebra[93,201]

$$\begin{aligned}\boldsymbol{W}^{\pm}_{\rm eq}(x,k) = \frac{1}{4}[&\boldsymbol{F}^{\pm}_{\rm eq}(x,k) + i\gamma_5\boldsymbol{P}^{\pm}_{\rm eq}(x,k) + \gamma^\mu\boldsymbol{V}^{\pm}_{{\rm eq},\mu}(x,k)\\ &+ \gamma_5\gamma^\mu\boldsymbol{A}^{\pm}_{{\rm eq},\mu}(x,k) + \Sigma^{\mu\nu}\boldsymbol{S}^{\pm}_{{\rm eq},\mu\nu}(x,k)].\end{aligned} \tag{146}$$

Note that the coefficient functions appearing in the above decomposition can be obtained by contracting $\boldsymbol{W}^{\pm}_{\rm eq}(x,k)$ with appropriate gamma matrices and then taking the trace.[197] The total Wigner function is the sum of the particle and antiparticle contributions $\boldsymbol{W}_{\rm eq}(x,k) = \boldsymbol{W}^{+}_{\rm eq}(x,k) + \boldsymbol{W}^{-}_{\rm eq}(x,k)$.

16.3. *Semi-classical equation and formulation of hydrodynamics with spin*

A similar decomposition to Eq. (146) can be done for any arbitrary Wigner function $\boldsymbol{W}(x,k)$. In absence of any mean fields, $\boldsymbol{W}(x,k)$ satisfies the following equation:[201]

$$(\gamma_\mu K^\mu - m)\boldsymbol{W}(x,k) = C[\boldsymbol{W}(x,k)]; K^\mu = k^\mu + \frac{i\hbar}{2}\partial^\mu, \tag{147}$$

where $C[\boldsymbol{W}(x,k)]$ is the collision term. In global or local equilibrium, the collision term vanishes. In this situation, solution of above equation can be written in the form of a series in $\hbar$,

$$\boldsymbol{X} = \boldsymbol{X}^{(0)} + \hbar\boldsymbol{X}^{(1)} + \hbar^2\boldsymbol{X}^{(2)} + \cdots; \boldsymbol{X} \in \{\boldsymbol{F}, \boldsymbol{P}, \boldsymbol{V}_\mu, \boldsymbol{A}_\mu, \boldsymbol{S}_{\nu\mu}\}.$$

Keeping the zeroth- and first-order terms in $\hbar$ expansion, the following equations for the coefficient functions $\boldsymbol{F}_{(0)}(x,k)$ and $\boldsymbol{A}^{\nu}_{(0)}(x,k)$ can be obtained,

$$k^\mu\partial_\mu\boldsymbol{F}_{(0)}(x,k) = 0, \quad k^\mu\partial_\mu\boldsymbol{A}^{\nu}_{(0)}(x,k) = 0, \quad k_\nu\,\boldsymbol{A}^{\nu}_{(0)}(x,k) = 0.$$

We note here that only two functions $\boldsymbol{F}^{(0)}$ and $\boldsymbol{A}^{(0)}_\mu$ are basic independent ones; others can be easily expressed by using these two. It can also be shown easily that the algebraic structure of the zeroth-order equations obtained from the semi-classical expansion of the Wigner function is consistent with the equilibrium coefficient functions. Therefore, we can replace $\boldsymbol{X}^{(0)}$ by $\boldsymbol{X}_{\rm eq}$. In this way, we can get the following Boltzmann-like kinetic equations for the equilibrium coefficient functions

$$k^\mu\partial_\mu\boldsymbol{F}_{\rm eq}(x,k) = 0, \quad k^\mu\partial_\mu\,\boldsymbol{A}^{\nu}_{\rm eq}(x,k) = 0, \quad k_\nu\,\boldsymbol{A}^{\nu}_{\rm eq}(x,k) = 0.$$

These equations represent the case of global equilibrium and are exactly fulfilled if $\partial_\mu\beta^\nu - \partial_\nu\beta^\mu = 0$, $\xi = $ const. and spin polarization tensor $\omega_{\mu\nu} = $ const.. The equation for β_μ field is known as the Killing equation; its solution can be written as $\beta_\mu = b^0_\mu + \varpi_{\mu\nu}x^\nu$ with thermal vorticity $\varpi_{\mu\nu}$ being constant, Thus, we see that both spin polarization tensor $\omega_{\mu\nu}$ and thermal vorticity $\varpi_{\mu\nu}$ are constant but no conclusion can be drawn whether two are equal in global equilibrium.

In the local equilibrium, only certain moments of above kinetic equations can be set equal to zero; this point has been discussed in great detail in Ref. 197. It was shown in Ref. 197 that the following equations for the conservation laws for charge and energy–momentum and spin tensor can be obtained

$$\partial_\mu N^\mu(x) = 0, \quad \partial_\mu T^{\mu\nu}_{\rm GLW}((x) = 0, \quad \partial_\lambda S^{\lambda,\mu\nu}_{\rm GLW}(x) = 0. \tag{148}$$

Exact expressions for charge current $N^\mu(x)$, energy–momentum $T^{\mu\nu}_{\rm GLW}$, and spin tensor $S^{\lambda,\mu\nu}_{\rm GLW}$ are given in Ref. 197. As this formulation does not allow for arbitrary large values of the polarization tensor, we restrict ourself to the leading-order

expressions in the $\omega_{\mu\nu}$.[198] In this case, the expressions for charge current $N^\mu(x)$ and energy momentum tensor $T^{\mu\nu}_{\rm GLW}(x)$ are given by

$$N^\alpha = nU^\alpha, \quad T^{\alpha\beta}_{\rm GLW} = (\varepsilon + P)U^\alpha U^\beta - Pg^{\alpha\beta}. \tag{149}$$

In Eq. (149), n is the number density which is given by the expression,

$$n = 4\sinh(\xi) n_{(0)}(T), \tag{150}$$

where the factor $4\sinh(\xi) = 2(e^\xi - e^{-\xi})$ accounts for spin degeneracy and presence of both particles and antiparticles and $n_{(0)}(T) = \langle p\cdot U\rangle_0$ is the number density of spinless and neutral massive Boltzmann particles, with $\langle\cdots\rangle_0$ denoting a thermal average as defined in Ref. 199.

In Eq. (149), ε and P are the energy density and pressure which are given by following expressions:

$$\varepsilon = 4\cosh(\xi)\varepsilon_{(0)}(T), \quad P = 4\cosh(\xi)P_{(0)}(T); \tag{151}$$

similar to $n_{(0)}(T)$, the auxiliary quantities $\varepsilon_{(0)}(T)$ and $P_{(0)}(T)$ are expressed as $\varepsilon_{(0)}(T) = \langle (p\cdot U)^2\rangle_0$ and $P_{(0)}(T) = -(1/3)\langle p\cdot p - (p\cdot U)^2\rangle_0$.

In the leading order in $\omega_{\mu\nu}$, the expression for the spin tensor $S^{\alpha,\beta\gamma}_{\rm GLW}$ is given by

$$S^{\alpha,\beta\gamma}_{\rm GLW} = \cosh(\xi)(n_{(0)}(T)U^\alpha\omega^{\beta\gamma} + S^{\alpha,\beta\gamma}_{\Delta\rm GLW}), \tag{152}$$

In the above expression, the auxiliary tensor $S^{\alpha,\beta\gamma}_{\Delta\rm GLW}$ is defined as[194]

$$\begin{aligned} S^{\alpha,\beta\gamma}_{\Delta\rm GLW} &= \mathcal{A}_{(0)}\, U^\alpha U^\delta U^{[\beta}\omega^{\gamma]}_{\ \ \delta} \\ &\quad + \mathcal{B}_{(0)}(U^{[\beta}\Delta^{\alpha\delta}\omega^{\gamma]}_{\ \ \delta} + U^\alpha\Delta^{\delta[\beta}\omega^{\gamma]}_{\ \ \delta} + U^\delta\Delta^{\alpha[\beta}\omega^{\gamma]}_{\ \ \delta}), \end{aligned} \tag{153}$$

where

$$\mathcal{B}_{(0)} = -\frac{2}{\hat{m}^2}\frac{\varepsilon_{(0)}(T) + P_{(0)}(T)}{T}, \quad \mathcal{A}_{(0)} = -3\mathcal{B}_{(0)} + 2n_{(0)}(T).$$

16.4. *Application of hydrodynamics with spin to heavy-ion collsions*

We consider the case of transversely homogeneous and boost-invariant expansion of the fireball produced in the heavy-ion collisions. Such a case can be described by the following four boost invariant basis:

$$\begin{aligned} U^\alpha &= \frac{1}{\tau}(t,0,0,z) = (\cosh(\eta),0,0,\sinh(\eta)), \\ X^\alpha &= (0,1,0,0), \\ Y^\alpha &= (0,0,1,0), \\ Z^\alpha &= \frac{1}{\tau}(z,0,0,t) = (\sinh(\eta),0,0,\cosh(\eta)) \end{aligned} \tag{154}$$

where $\tau = \sqrt{t^2 - z^2}$ is the longitudinal proper time, while $\eta = \ln((t+z)/(t-z))/2$ is the space-time rapidity. The four-vector U^α is normalized to unity and a time-like

vector while four-vectors X^α, Y^α and Z^α are space-like and orthogonal to U^α as well as to each other.

Using the basis (154), the following representation of the spin polarization tensor $\omega_{\mu\nu}$ can be introduced (for details, see Ref. 199):

$$\begin{aligned}\omega_{\mu\nu} = {} & C_{\kappa Z}(Z_\mu U_\nu - Z_\nu U_\mu) + C_{\kappa X}(X_\mu U_\nu - X_\nu U_\mu) \\ & + C_{\kappa Y}(Y_\mu U_\nu - Y_\nu U_\mu) \\ & + \epsilon_{\mu\nu\alpha\beta}U^\alpha(C_{\omega Z}Z^\beta + C_{\omega X}X^\beta + C_{\omega Y}Y^\beta).\end{aligned} \tag{155}$$

Here we note that due to boost invariant notion, the scalar coefficients $C's$ are functions of the proper time τ only. Knowing the boost boost-invariant decomposition of $\omega_{\mu\nu}$, a boost-invariant expression for the spin tensor $S^{\alpha,\beta\gamma}_{\rm GLW}$ can also be obtained and finally, the boost invariant form of conservation laws (given in Eq. (148)) can respectively be written as follows:

$$\dot{n} + \frac{n}{\tau} = 0, \tag{156}$$

$$\dot{\varepsilon} + \frac{(\varepsilon + P)}{\tau} = 0, \tag{157}$$

$$\begin{bmatrix} \boldsymbol{L}(\tau) & 0 & 0 & 0 & 0 & 0 \\ 0 & \boldsymbol{L}(\tau) & 0 & 0 & 0 & 0 \\ 0 & 0 & \boldsymbol{L}(\tau) & 0 & 0 & 0 \\ 0 & 0 & 0 & \boldsymbol{P}(\tau) & 0 & 0 \\ 0 & 0 & 0 & 0 & \boldsymbol{P}(\tau) & 0 \\ 0 & 0 & 0 & 0 & 0 & \boldsymbol{P}(\tau) \end{bmatrix} \begin{bmatrix} \dot{C}_{\kappa X} \\ \dot{C}_{\kappa Y} \\ \dot{C}_{\kappa Z} \\ \dot{C}_{\omega X} \\ \dot{C}_{\omega Y} \\ \dot{C}_{\omega Z} \end{bmatrix}$$

$$= \begin{bmatrix} \boldsymbol{Q}_1(\tau) & 0 & 0 & 0 & 0 & 0 \\ 0 & \boldsymbol{Q}_1(\tau) & 0 & 0 & 0 & 0 \\ 0 & 0 & \boldsymbol{Q}_2(\tau) & 0 & 0 & 0 \\ 0 & 0 & 0 & \boldsymbol{R}_1(\tau) & 0 & 0 \\ 0 & 0 & 0 & 0 & \boldsymbol{R}_1(\tau) & 0 \\ 0 & 0 & 0 & 0 & 0 & \boldsymbol{R}_2(\tau) \end{bmatrix} \begin{bmatrix} C_{\kappa X} \\ C_{\kappa Y} \\ C_{\kappa Z} \\ C_{\omega X} \\ C_{\omega Y} \\ C_{\omega Z} \end{bmatrix}, \tag{158}$$

where $\boldsymbol{L}(\tau) = \boldsymbol{A}_1 - \frac{1}{2}\boldsymbol{A}_2 - \boldsymbol{A}_3$,
$\boldsymbol{P}(\tau) = \boldsymbol{A}_1$,
$\boldsymbol{Q}_1(\tau) = -[\dot{\boldsymbol{L}} + \frac{1}{\tau}(\boldsymbol{L} + \frac{1}{2}\boldsymbol{A}_3)]$, $\boldsymbol{Q}_2(\tau) = -(\dot{\boldsymbol{L}} + \frac{\boldsymbol{L}}{\tau})$,
$\boldsymbol{R}_1(\tau) = -[\dot{\boldsymbol{P}} + \frac{1}{\tau}(\boldsymbol{P} - \frac{1}{2}\boldsymbol{A}_3)]$, and $\boldsymbol{R}_2(\tau) = -(\dot{\boldsymbol{P}} + \frac{\boldsymbol{P}}{\tau})$ with $\boldsymbol{A}_1$, $\boldsymbol{A}_2$, and $\boldsymbol{A}_3$ given by $\boldsymbol{A}_1 = \boldsymbol{C}\left(n_{(0)} - \boldsymbol{B}_{(0)}\right)$, $\boldsymbol{A}_2 = \boldsymbol{C}\left(\boldsymbol{A}_{(0)} - 3\boldsymbol{B}_{(0)}\right)$, and $\boldsymbol{A}_3 = \boldsymbol{C}\,\boldsymbol{B}_{(0)}$.

One can be seen that all the C coefficients evolve independently. Moreover, due to the rotational invariance in the transverse plane coefficients, $C_{\kappa X}$ and $C_{\kappa Y}$ (also $C_{\omega X}$ and $C_{\omega Y}$) obey the same differential equations. The system of Eqs. (156), (157) and (158) can be easily solved numerically. We first solve Eqs. (156) and (157) to find the proper-time dependence of the temperature T and chemical potential μ.

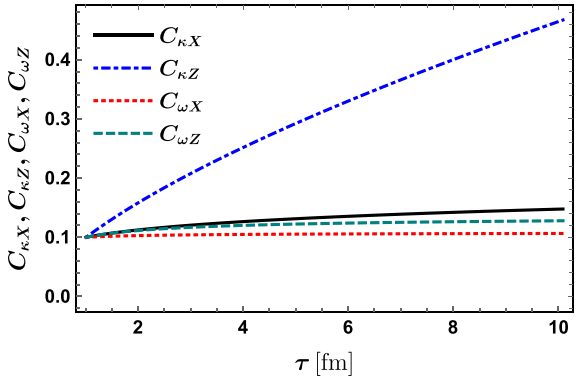

Fig. 46. Proper-time evolution of the coefficients $C_{\kappa X}$, $C_{\kappa Z}$, $C_{\omega X}$ and $C_{\omega Z}$.

Once the functions $T(\tau)$ and $\mu(\tau)$ are known, we can easily determine the functions $\boldsymbol{L}$, $\boldsymbol{P}$, $\boldsymbol{Q}$ and $\boldsymbol{R}$ in (158) and finally the proper-time dependence of C coefficients.

In order to study situations similar to experiments, we consider matter with the initial baryon chemical potential $\mu_0 = 800\,\text{MeV}$ and the initial temperature $T_0 = 155\,\text{MeV}$. We take particle mass to be equal to the mass of Λ-hyperon, $m = 1116\,\text{MeV}$ and continue the hydrodynamic evolution from $\tau_0 = 1$ fm, till the final time $\tau_f = 10$ fm. In this scenario, the proper-time dependence of the coefficients $C_{\kappa X}$, $C_{\kappa Z}$, $C_{\omega X}$ and $C_{\omega Z}$ is shown in Fig. 46 for the same initial values (0.1) of all the C coefficients. We have omitted $C_{\kappa Y}$ and $C_{\omega Y}$ because they fulfill the same equations as $C_{\kappa X}$ and $C_{\omega X}$). It can see that the coefficient $C_{\kappa Z}$ has the strongest time dependence as it increases by about 0.1 within 1 fm.

16.5. *Physical observable*

In this section, we demonstrate how hydrodynamics with spin can be used to obtain the information about the spin polarization of particles at freeze-out. The spin polarization of particles can be determined by the average Pauli–Lubański vector $\langle \pi_\mu(p) \rangle$ in the rest frame of the particles. The average Pauli–Lubański vector $\langle \pi_\mu(p) \rangle$ of particles with momentum p emitted from a given the freeze-out hypersurface is obtained by the expression[197]

$$\langle \pi_\mu \rangle = \frac{E_p \dfrac{d\Pi_\mu(p)}{d^3p}}{E_p \dfrac{d\boldsymbol{N}(p)}{d^3p}}, \tag{159}$$

where

$$E_p \frac{d\Pi_\mu(p)}{d^3p} = -\frac{\cosh(\xi)}{(2\pi)^3 m} \int \Delta\Sigma_\lambda p^\lambda \, e^{-\beta\cdot p} \, \tilde{\omega}_{\mu\beta} p^\beta. \tag{160}$$

$$E_p \frac{d\boldsymbol{N}(p)}{d^3p} = \frac{4\cosh(\xi)}{(2\pi)^3} \int \Delta\Sigma_\lambda p^\lambda \, e^{-\beta\cdot p}. \tag{161}$$

In the above expressions, $\Delta\Sigma_\lambda$ is the element of freeze-out hypersurface and p^λ is the particle four momentum. The above integrations can be carried out very easily by parametrizing p^λ in terms of transverse mass m_T and rapidity y_p as $p^\lambda = (m_T \cosh(y_p), p_x, p_y, m_T \sinh(y_p))$ and assuming that freeze-out takes place at a constant value of the proper time ($\Delta\Sigma_\lambda = U_\lambda dxdy\,\tau d\eta$). To compare the final result with experimental data, we have to boost the average Pauli–Lubański vector to the rest frame of the particles. Note that since most of the experimental measurements of the spin polarization are done at midrapidity, therefore we can consider particles with $y_p = 0$. Moreover, since the mass of the Λ is much larger, then the values of temperature considered by us, we may take $m_T \gg 1$. In this case, the spin polarization obtained in the particle rest frame can be cast to much simpler formula as follows:

$$\langle \boldsymbol{\pi}^* \rangle = -\frac{1}{4m}\left[E_p \boldsymbol{C}_\omega - \boldsymbol{p} \times \boldsymbol{C}_\kappa - \frac{\boldsymbol{p}\cdot\boldsymbol{C}_\omega}{E_p + m}\boldsymbol{p}\right], \tag{162}$$

where $\boldsymbol{p} = (p_x, p_y, 0)$. From the above formula, one can see that for particles with small transverse momenta, the polarization is directly determined by the coefficients $\boldsymbol{C}_\omega$ whose value can be obtained using hydrodynamic equations as discussed above.

16.6. *Summary and conclusions*

In this contribution, using the relativistic distribution functions for particles and antiparticles with spin 1/2 at local thermodynamical equilibrium as introduced in Ref. 200, we have constructed the equilibrium Wigner functions. Using the kinetic equation for Wigner function and its semiclassical expansion, we have formulated hydrodynamics with spin. For the transversely homogeneous and boost invariant expansion of heavy-ion collision fireball, we have shown that hydrodynamics with spin can be used to determine the space-time evolution of the spin polarization tensor and finally spin polarization of the particles.

17. Solutions and Attractors of Causal Dissipative Hydrodynamics for Bjorken Flow

Sunil Jaiswal, Chandrodoy Chattopadhyay, Amaresh Jaiswal, Subrata Pal, Ulrich Heinz

Causal higher-order theories of relativistic viscous hydrodynamics in the limit of one-dimensional boost-invariant expansion is considered. Evolution equations for the inverse Reynolds number as a function of Knudsen number is obtained for three different choices of time dependence of the shear relaxation rate. It is shown that solutions of these equations exhibit attractor behavior. These dynamical attractors are characterized and uniquely determined by studying the analytical solutions at both small and large Knudsen numbers.

17.1. *Introduction*

Relativistic viscous hydrodynamics has been very successful in explaining a wide range of collective phenomena observed in heavy-ion collisions. Based on the paradigm that hydrodynamics requires local thermodynamic equilibrium to be applicable,[202] this successful hydrodynamic description led to the belief that these collisions create a nearly thermalized medium close to local thermal equilibrium.[203] However, the advent of numerical dissipative relativistic fluid dynamics provides evidence of large deviations from local thermal equilibrium. This "unreasonable effectiveness" of hydrodynamics has generated much recent interest in the very foundations of fluid dynamics, culminating in the formulation of a new "far-from-local-equilibrium fluid dynamics" paradigm.[169,204]

The simplest relativistic dissipative theory, relativistic Navier–Stokes (NS) theory, imposes instantaneous constitutive relations between the dissipative flows and their generating forces. This approach was found to be plagued by acausality and intrinsic instability.[205] The phenomenological second-order theory developed by Müller, Israel, and Stewart (MIS)[206,207] cures these problems by introducing a relaxation type equation for the dissipative flows and thus turning them into independent dynamical fields. As discussed in,[169] even the minimal causal Maxwell–Cattaneo theory[208] resolves the causality issue, but introduces new "nonhydrodynamic modes" that were absent in NS theory. These nonhydrodynamic modes are now known to play an important role in the approach to the regime of applicability of hydrodynamics, also known as the "hydrodynamization" process.[202] In this study, we will focus on yet another feature that appears in causal theories of relativistic dissipative hydrodynamics, "the hydrodynamic attractor".[209]

17.2. *Attractor in "minimal causal theory"*

The energy–momentum tensor for a conformal system in the Landau frame has the form

$$T^{\mu\nu} = \epsilon u^\mu u^\nu - P\Delta^{\mu\nu} + \pi^{\mu\nu}, \tag{163}$$

where ϵ and P are the local energy density and pressure. Conformal symmetry implies an equation of state (EoS) $\epsilon = 3P$ and zero bulk viscous pressure, $\Pi = 0$. We define $\Delta^{\mu\nu} \equiv g^{\mu\nu} - u^\mu u^\nu$ which serves as a projection operator to the space orthogonal to u^μ. Notations used: the metric convention used here is $g^{\mu\nu} = \mathrm{diag}(+---)$. We use $\sigma_{\mu\nu} \equiv \frac{1}{2}(\nabla_\mu u_\nu + \nabla_\nu u_\mu) - \frac{1}{3}\theta\Delta_{\mu\nu}$ for the velocity shear tensor, $\nabla^\alpha \equiv \Delta^{\mu\alpha} D_\mu$ for space-like derivative, D_μ for the covariant derivative and $\theta \equiv D_\mu u^\mu$ for the expansion scalar.

The shear stress tensor, $\pi^{\mu\nu}$, is traceless and orthogonal to u^μ. The simplest form of $\pi^{\mu\nu}$ is the Navier–Stokes form, which is first order in velocity gradients, $\pi^{\mu\nu}_{\rm NS} = 2\eta\sigma^{\mu\nu}$ where η is the shear viscosity coefficient. However, relativistic Navier–Stokes theory imposes instantaneous constitutive relations between the dissipative flows and their generating forces which results to superluminal signal propagation.

The simplest way to restore causality is by introducing a dynamic relaxation-type equation for $\pi^{\mu\nu}$. This prescription, also known as the "Maxwell–Cattaneo theory", requires that the dissipative forces relax to their Navier–Stokes values in some finite relaxation time, i.e.,

$$\tau_\pi \dot{\pi}^{\langle\mu\nu\rangle} + \pi^{\mu\nu} = 2\eta\sigma^{\mu\nu}, \tag{164}$$

where τ_π is the shear relaxation time. We will now demonstrate the hydrodynamic attractor which appears in this minimal causal theory for Bjorken flow. We use the notation $\dot{A} \equiv u^\mu D_\mu A$ for the co-moving time derivative. Angular brackets around pairs of Lorentz indices indicate projection of the tensor onto its traceless and locally spatial part, e.g., $\dot{\pi}^{\langle\mu\nu\rangle} \equiv \Delta^{\mu\nu}_{\alpha\beta}\dot{\pi}^{\alpha\beta}$, where $\Delta^{\mu\nu}_{\alpha\beta} \equiv \frac{1}{2}(\Delta^\mu_\alpha\Delta^\nu_\beta + \Delta^\mu_\beta\Delta^\nu_\alpha) - \frac{1}{3}\Delta^{\mu\nu}\Delta_{\alpha\beta}$.

Bjorken Flow — We will now simplify evolution equations for ϵ and u^μ obtained from energy–momentum conservation, $D_\mu T^{\mu\nu} = 0$, and Eq. (164) for Bjorken flow. For transversally homogeneous and longitudinally boost-invariant systems expressed in Milne coordinates $x^\mu = (\tau, x, y, \eta_s)$ (with $\tau = \sqrt{t^2 - z^2}$ and $\eta_s = \tanh^{-1}(z/t)$), the shear tensor is diagonal and space-like leaving only one independent component which we take to be the $\eta_s\eta_s$ component: $\pi^{xx} = \pi^{yy} = -\tau^2\pi^{\eta_s\eta_s}/2 \equiv \pi/2$.

Maxwell–Cattaneo Theory — Energy conservation and shear evolution equations for Maxwell–Cattaneo (164) reduce to a set of coupled ordinary differential equations (ODEs) in τ:

$$\frac{d\epsilon}{d\tau} = -\frac{1}{\tau}\left(\frac{4}{3}\epsilon - \pi\right), \quad \frac{d\pi}{d\tau} = -\frac{\pi}{\tau_\pi} + \frac{4}{3}\frac{\beta_\pi}{\tau}. \tag{165}$$

Since $\beta_\pi \equiv \eta/\tau_\pi = 4\epsilon/15$, Eq. (165) is mutually coupled. The equation for shear stress can be decoupled by rewriting it in terms of dimensionless quantities, normalized shear stress (inverse Reynolds number) $\bar{\pi} = \pi/(\epsilon + P) = \pi/(4P)$, and rescaled time variable $\bar{\tau} \equiv \tau/\tau_\pi$ (which is the inverse Knudsen number for Bjorken flow). Maxwell–Cattaneo evolution (Eq. (165)) takes the form:

$$\frac{d\bar{\tau}}{d\tau} = \left(\frac{\bar{\pi} + 2}{3}\right)\frac{\bar{\tau}}{\tau}, \tag{166}$$

$$\left(\frac{\bar{\pi} + 2}{3}\right)\frac{d\bar{\pi}}{d\bar{\tau}} = -\bar{\pi} + \frac{1}{\bar{\tau}}\left(\frac{4}{15} + \frac{4}{3}\bar{\pi} - \frac{4}{3}\bar{\pi}^2\right). \tag{167}$$

Here we also used that for a conformal system $\epsilon \propto T^4$ and $T\tau_\pi = 5\bar{\eta} = \text{const.}$ where $\bar{\eta} \equiv \eta/s$ is the specific shear viscosity. Equation (167) is a first-order nonlinear ODE for the inverse Reynolds number that is completely decoupled from the evolution of the energy density.

We obtain the numerical attractor for Maxwell–Cattaneo from Eq. (164) following the prescription outlined in Ref. 209. Figure 47 shows the evolution of pressure anisotropy, which is related to normalized shear through the equation

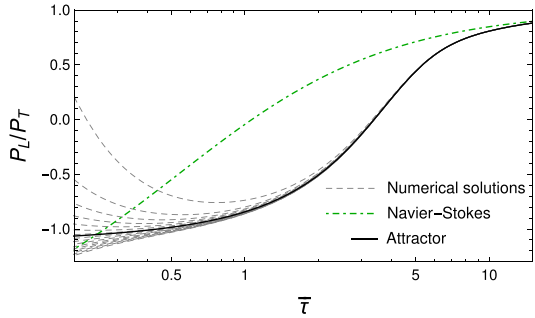

Fig. 47. (Color online) Gray dashed lines are numerical solutions of Eq. (167) for different initial conditions and solid black line represents the numerically determined attractor. Navier–Stokes is represented by dash-dotted green line.

$\frac{P_L}{P_T} = \frac{P-\pi}{P+\pi/2} = \frac{1-4\bar{\pi}}{1+2\bar{\pi}}$, for various initial conditions. One sees that numerical solutions for a broad range of initial conditions join the attractor at $\bar{\tau} \sim 2$, but that start to agree with the NS solution only for $\bar{\tau} \gtrsim 20$.

17.3. *Higher-order theories*

We will now look at higher order hydrodynamic theories. For minimal causal conformally symmetric systems, one more term must be added in the evolution of shear stress to the Maxwell–Cattaneo theory:

$$\tau_\pi \dot{\pi}^{\langle\mu\nu\rangle} + \pi^{\mu\nu} = 2\eta\sigma^{\mu\nu} - \frac{4}{3}\tau_\pi \pi^{\mu\nu}\theta. \tag{168}$$

This equation is a close variant[210] of the one first derived by Müller, Israel and Stewart,[206,207] and we will therefore refer to it as the "MIS" theory.

A systematic derivation of second-order ("transient") relativistic fluid dynamics from kinetic theory was performed in Ref. 211. For conformal systems and an RTA collision term, the result obtained in the 14-moment approximation differs from Eq. (168) by two additional terms:

$$\dot{\pi}^{\langle\mu\nu\rangle} + \frac{\pi^{\mu\nu}}{\tau_\pi} = 2\beta_\pi\sigma^{\mu\nu} + 2\pi_\gamma^{\langle\mu}\omega^{\nu\rangle\gamma} - \frac{10}{7}\pi_\gamma^{\langle\mu}\sigma^{\nu\rangle\gamma} - \frac{4}{3}\pi^{\mu\nu}\theta. \tag{169}$$

Here $\omega^{\mu\nu} \equiv \frac{1}{2}(\nabla^\mu u^\nu - \nabla^\nu u^\mu)$ is the vorticity tensor. This "DNMR" theory[211] can also be derived from a Chapman–Enskog like iterative solution of the RTA Boltzmann equation.[166]

Carrying the Chapman–Enskog expansion to one additional order, a third-order evolution equation for the shear stress was derived for the same system in 167 which we will refer as the "third-order" theory.

For Bjorken flow, the energy density and shear evolution equations for the above mentioned three theories can be brought into the following generic form:

$$\frac{d\epsilon}{d\tau} = -\frac{1}{\tau}\left(\frac{4}{3}\epsilon - \pi\right), \tag{170}$$

$$\frac{d\pi}{d\tau} = -\frac{\pi}{\tau_\pi} + \frac{1}{\tau}\left[\frac{4}{3}\beta_\pi - \left(\lambda + \frac{4}{3}\right)\pi - \chi\frac{\pi^2}{\beta_\pi}\right]. \tag{171}$$

The coefficients β_π, a, λ, χ, and γ appearing in Eq. (171) above and in Eq. (172) are tabulated in Table 4 for these three theories.

The shear evolution equation can be decoupled from the energy density evolution equation following similar procedure as mentioned in Sec. 17.2:

$$\left(\frac{\bar{\pi}+2}{3}\right)\frac{d\bar{\pi}}{d\bar{\tau}} = -\bar{\pi} + \frac{1}{\bar{\tau}}(a - \lambda\,\bar{\pi} - \gamma\,\bar{\pi}^2), \tag{172}$$

which has the same form as Eq. (167). Note that Eqs. (167) and (172) has the form of an Abel differential equation of the second kind for which, to the best of our knowledge, an analytical solution does not exist. The three hydrodynamic theories can be selected by choosing for λ and γ the appropriate combinations of constants given in Table 4.

17.4. *Analytical solutions*

We will now derive analytical solutions for the evolution of $\bar{\pi}$ for Bjorken flow, at the expense of not being able to ensure the conformal relation $T\tau_\pi = \text{const.}$ consistently with the evolution of the energy density. Instead, we find three separate classes of analytical solutions, corresponding to three different approximations of τ_π as a function of time.

Starting from Eqs. (170) and (171), we decouple them as before by rewriting them in terms of the inverse Reynolds number $\bar{\pi}$ but without rescaling the proper time:

$$\frac{1}{\epsilon\tau^{4/3}}\frac{d(\epsilon\tau^{4/3})}{d\tau} = \frac{4}{3}\frac{\bar{\pi}}{\tau}, \tag{173}$$

$$\frac{d\bar{\pi}}{d\tau} = -\frac{\bar{\pi}}{\tau_\pi} + \frac{1}{\tau}(a - \lambda\bar{\pi} - \gamma\bar{\pi}^2). \tag{174}$$

In the following, we find analytical solutions of Eq. (174), using different approximations for the form of shear relaxation time τ_π.[212]

Table 4. Coefficients for the causal viscous hydrodynamic evolution of the shear stress in Bjorken flow for the three theories studied in this work.

	β_π	a	λ	χ	γ
MIS	$4P/5$	4/15	0	0	4/3
DNMR	$4P/5$	4/15	10/21	0	4/3
Third-order	$4P/5$	4/15	10/21	72/245	412/147

1. Constant relaxation time — In this approximation,[213] the scaling of τ_π with temperature was ignored by simply setting it constant. This constitutes a rather drastic violation of conformal symmetry by introducing, in addition to the inverse temperature $1/T$, a second, independent length scale τ_π. In the following two approximations, we will successively improve on this.

Introducing again the rescaled time $\bar{\tau} = \tau/\tau_\pi$, for constant τ_π, Eq. (174) turns directly into

$$\frac{d\bar{\pi}}{d\bar{\tau}} = -\bar{\pi} + \frac{1}{\bar{\tau}}(a - \lambda\bar{\pi} - \gamma\bar{\pi}^2), \tag{175}$$

which is similar to Eq. (172) but without the nonlinearity on the left-hand side (l.h.s). As will be discussed in Sec. 17.5, this difference has important consequences for the attractor solutions and Lyapunov exponents.

2. Relaxation time from ideal hydrodynamics — A better approximation to Eq. (172) can be obtained by setting $T\tau_\pi = \text{const.}$ by approximating the time-dependence of T at late times with the ideal fluid law

$$T_{\rm id}(\tau) = T_0 \left(\frac{\tau_0}{\tau}\right)^{1/3}, \tag{176}$$

where T_0 is the temperature at initial time τ_0. For $T\tau_\pi = 5\bar{\eta}$, this yields $\tau_\pi(\tau) = b\,\tau^{1/3}$, with $b = \frac{5\bar{\eta}}{T_0\tau_0^{1/3}}$. Using this to define the scaled time variable $\bar{\tau} \equiv \tau/\tau_\pi$, Eq. (174) turns into

$$\frac{2}{3}\frac{d\bar{\pi}}{d\bar{\tau}} = -\bar{\pi} + \frac{1}{\bar{\tau}}(a - \lambda\bar{\pi} - \gamma\bar{\pi}^2), \tag{177}$$

independent of b. This equation again misses the nonlinear term on the l.h.s. of Eq. (172) and has the same structure as Eq. (175).

3. Relaxation time from Navier–Stokes evolution — We can further improve our approximation by accounting for first-order gradient effects in the evolution of the temperature, by replacing the ideal fluid law (176) by the Navier–Stokes result[171,210]

$$T_{\rm NS} = T_0 \left(\frac{\tau_0}{\tau}\right)^{1/3} \left[1 + \frac{2\bar{\eta}}{3\tau_0 T_0}\left\{1 - \left(\frac{\tau_0}{\tau}\right)^{2/3}\right\}\right]. \tag{178}$$

Substituting this into $T\tau_\pi = 5\bar{\eta}$, we find

$$\tau_\pi = \frac{\tau^{1/3}}{d - \frac{2}{15}\tau^{-2/3}}, \quad d \equiv \left(\frac{T_0\tau_0}{5\bar{\eta}} + \frac{2}{15}\right)\tau_0^{-2/3}. \tag{179}$$

Using this relation, Eq. (174) in terms of scaled time variable $\bar{\tau} \equiv \tau/\tau_\pi$:

$$\left(\frac{a/\bar{\tau} + 2}{3}\right)\frac{d\bar{\pi}}{d\bar{\tau}} = -\bar{\pi} + \frac{1}{\bar{\tau}}\left(a - \lambda\bar{\pi} - \gamma\bar{\pi}^2\right), \tag{180}$$

independent of the constant d. This shares with Eq. (177) the same factor $2/3$ on the l.h.s..

Table 5. Arguments and parameters of Eq. (181) for the analytic approximations studied.

$T(\tau)$	w	Λ	k	m
Const.	$\bar{\tau}$	-1	$-\frac{1}{2}(\lambda+1)$	$\frac{1}{2}\sqrt{4a\gamma+\lambda^2}$
Ideal	$\frac{3}{2}\bar{\tau}$	$-\frac{3}{2}$	$-\frac{3\lambda+2}{4}$	$\frac{3}{4}\sqrt{4a\gamma+\lambda^2}$
NS	$\frac{3}{2}(\bar{\tau}+\frac{a}{2})$	$-\frac{3}{2}$	$-\frac{6\lambda+4-3a}{8}$	$\frac{3}{8}\sqrt{16a\gamma+a^2-4a\lambda+4\lambda^2}$

Equations (175), (177) and (180) are the first-order nonlinear ODE of Riccati type whose solutions can be given in the generic form[212]

$$\bar{\pi}(w) = \frac{\left(k+m+\frac{1}{2}\right) M_{k+1,m}(w) - \alpha W_{k+1,m}(w)}{\gamma|\Lambda|[M_{k,m}(w) + \alpha W_{k,m}(w)]}. \tag{181}$$

The arguments and parameters appearing in the above equations are given in Table 5. Here ϵ_0 is the initial energy density at time $\bar{\tau}_0$, and the constant α encodes the initial normalized shear stress $\bar{\pi}_0$. Note that α can only take values for which the energy density is positive-definite for $\bar{\tau} > 0$.

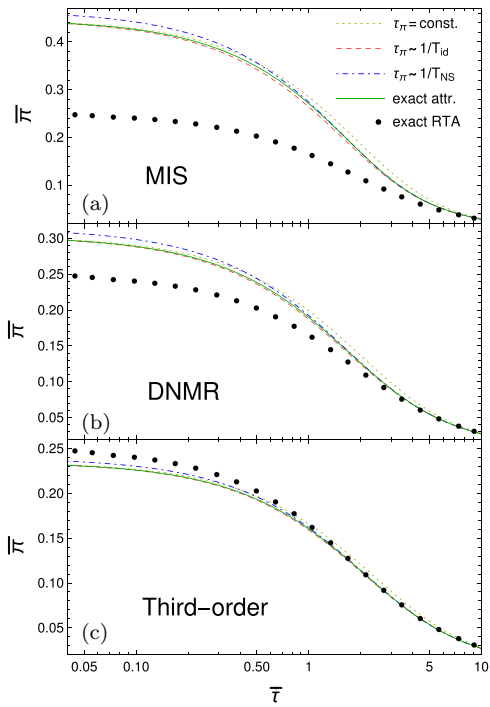

Fig. 48. (Color online) Approximate analytical attractors for different theories compared with their exact numerical attractors (solid green lines) and the exact analytical attractor for the RTA Boltzmann equation (black dots).

17.5. *Analytical attractors and Lyapunov exponent*

In this section, we determine the hydrodynamic attractors and obtain the Lyapunov exponent (Λ) from the analytic solutions. We introduce the following procedure for identifying the hydrodynamic attractor:[212,214] In terms of the parameter α encoding the initial condition for $\bar{\pi}$, we search for the value α_0 at which the quantity

$$\psi(\alpha_0) \equiv \lim_{\bar{\tau}\to\bar{\tau}_0} \frac{\partial\bar{\pi}}{\partial\alpha}\bigg|_{\alpha=\alpha_0} \tag{182}$$

diverges at the scaled time $\bar{\tau}_0$ where the two fixed points of the evolution trajectories are located. Using this prescription, we obtain the attractor solutions from Eq. (181) by setting the initial condition parameter $\alpha = 0$:

$$\bar{\pi}_{\rm attr}(w) = \frac{k+m+\frac{1}{2}}{\gamma|\Lambda|}\frac{M_{k+1,m}(w)}{M_{k,m}(w)}. \tag{183}$$

The attractors are shown in Fig. 48 for the three different hydrodynamic theories discussed in this paper (MIS (a), DNMR (b), and third-order (c)) and compared with the corresponding exact numerical attractors (obtained from Eq. (172) following the prescription outlined in Ref. 209) as well as with the attractor for the exact analytical solution of the RTA Boltzmann equation.[215]

To obtain the Lyapunov exponents (Λ) from the approximate analytic solutions, we use the formula[212]

$$\Lambda = \lim_{\bar{\tau}\to\infty} \frac{\partial}{\partial\bar{\tau}}\left[\ln\left(\frac{\partial\bar{\pi}}{\partial\alpha}\right)\right]. \tag{184}$$

We find that the constant temperature approximation corresponds to a Lyapunov exponent of $\Lambda = -1$. This obviously differs from $\Lambda = -\frac{3}{2}$[212,216] for the conformally invariant theories described by Eq. (172); the difference is a direct consequence of the breaking of conformal symmetry by setting τ_π constant instead of $\propto 1/T$. However, we recover the same Lyapunov exponent $\Lambda = -\frac{3}{2}$ as for the conformally invariant theories from the approximate solutions obtained when temperature dependence is approximated from ideal and Navier–Stokes evolution.

While the ODE describing the evolution of the inverse Reynolds number for Bjorken flow can be solved numerically, the analytic approximations studied here are surprisingly accurate, and they yield valuable insights into the details of initial state memory loss[212,217] and the approach to attractor dynamics in Bjorken flow.

18. Nonperturbative Dynamics of QCD and Its Phase Structure: An Overview

Deependra Singh Rawat, H. C. Chandola, Dinesh Yadav, H. C. Pandey

Keeping in view the dominance of nonperturbative phenomena in low energy regime of QCD, an infrared effective dual QCD based on topologically viable homogeneous fiber bundle approach, has been analyzed for exploring the dynamics of quark confinement in its dynamically broken phase which has been shown to lead to a unique multi-flux tube configuration and a typical glueball spectrum. The dynamics of confinement–deconfinement phase transition has been discussed by computing the critical parameters of phase transition and their possible implications to QGP formation and QCD phase structure has also been discussed. The intimate connection of chromoelectric field with the color confining features has been discussed to establish the validity of present dual QCD model in the infrared sector of QCD.

18.1. *Introduction*

QCD is the leading theoretical formulation of the strong interactions[218,219] which turns out to lead the outstanding description of the dynamics of quarks and gluons inside the hadrons. The phenomena associated with the high energy regimes of QCD where quarks and gluons are weakly interacting on account of asymptotic freedom[218] are rather well described by employing the perturbative mathematical techniques. However, its low energy limit where color isocharges become strongly coupled is still lack of precise understanding due to the appearance of several nonpertervative peculiarities like confinement, chirally asymmetric behavior and dielectric nature of QCD vacuum, the hadron mass spectrum, etc. In particular, the color confinement which is typically characterized by the absence of the asymptotic states of colored particles is one of the outstanding conjecture that direly needed a fundamental explanation using the first principle in the domain of hadron physics. To sort out the puzzling confining structure of QCD vacuum, the first proposal was made by Nambu[220] and others, which asserts that the magnetic condensation could provide the confinement of color electric flux carried by the quarks through the dual Meissner effect. The physical realization of the magnetic condensation of QCD vacuum or introduction of QCD monopoles in the theory requires an analytical field theoretical investigation that may essentially incorporate the topological properties of the associated gauge group. In this direction, 't Hooft's[221] proposal of Abelian dominance made a remarkable significance where fixing the gauge degrees of freedom reduces the QCD to the Abelian theory with the appearance of color magnetic monopoles as a topological excitation of the theory. The effective interaction of these colored monopoles brings the QCD vacuum in the state of color superconductivity and develops the confining features in the theory. Despite its ordered mathematical description, the Abelian projection technique suffers from the serious problem of gauge dependency to project out the Abelian dominance which is in the violation of the fact that all the natural processes must be gauge invariant. Keeping in view the gauge independent confining structure of QCD vacuum, we have recently[222–225] analyzed a dual version of color gauge theory by imposing an additional magnetic

isometry as an effective theory of the nonperturbative QCD. In such a dual formulation, the flux tube solution may be interpreted as the excitation corresponding to the topological degrees of freedom and develops two characteristic mass scales (vector and scalar mass mode).

In this study, we further focus on discussing the gauge invariant color confining structure of dual QCD vacuum and its implications in the study of QCD phase transition under the extreme conditions of temperature and density.

18.2. *Color confinement in dual QCD*

The magnetic symmetry[226–228] defined as an additional isometry of the internal fiber space is introduced with the non-Abelian formulation of a gauge theory in the $(4+n)$ multidimensional unified space. For an arbitrary gauge group (G), the associated magnetic symmetry structure is introduced by Killing vector fields ($\hat{m}$). The Killing condition along the magnetic vector may be imposed by insisting that the gauge potential ($\mathbf{W}_\mu$) must satisfy the gauge covariant magnetic symmetry condition[226,227] that keeps intact the gauge symmetry and for G $\equiv$ SU(2) is given by, $D_\mu \hat{m} = (\partial_\mu + g\mathbf{W}_\mu \times)\hat{m} = 0$ (where $\hat{m}$ belongs to the adjoint representation of gauge group) leading to the decomposition of the gauge potential ($\mathbf{W}_\mu$) in the following form:

$$\mathbf{W}_\mu = A_\mu \hat{m} - g^{-1}(\hat{m} \times \partial_\mu \hat{m}), \tag{185}$$

where $\hat{m}.\mathbf{W}_\mu \equiv A_\mu$ is the color electric potential unrestricted by magnetic symmetry and is Abelian in nature. The second term retains the topological characteristics resulting from the imposition of magnetic symmetry. The isolated singularities of the multiplet $\hat{m}$ may then be viewed to define the homotopy of the mapping $\Pi_2(S^2)$ on $\hat{m} : S^2_R \to S^2 = \mathrm{SU}(2)/U(1)$ which ensures the appearance of chromomagnetic monopoles in the theory. It clearly shows that the imposition of magnetic symmetry on the gauge potential brings the topological structure into the dynamics explicitly. The duality between color isocharges and topological charges becomes more evident when the gauge fields and the associated gauge potential Eq. (185) are expressed in terms of magnetic gauge (or Dirac gauge) obtained by rotating $\hat{m}$ to a prefixed space-time independent direction in isospace using a gauge transformation (U) as $\hat{m} \longrightarrow \hat{\zeta}_3 = (0,0,1)^T$ which leads to the field decomposition as $\mathbf{G}_{\mu\nu} = \mathbf{W}_{\nu,\mu} - \mathbf{W}_{\mu,\nu} + g\mathbf{W}_\mu \times \mathbf{W}_\nu \equiv (F_{\mu\nu} + B^{(d)}_{\mu\nu})\hat{m}$ with $F_{\mu\nu} = A_{\nu,\mu} - A_{\mu\nu}$ and $B^{(d)}_{\mu\nu} = B_{\nu,\mu} - B_{\mu,\nu} = g^{-1}\hat{m}.(\partial_\mu \hat{m} \times \partial_\nu \hat{m})$. The dynamics of the resulting dual QCD vacuum and its implications on color confinement then follows from the SU(2) Lagrangian with a quark doublet source $\psi(x)$, as given by

$$\mathcal{L} = -\frac{1}{4}G^2_{\mu\nu} + \bar{\psi}(x)i\gamma^\mu D_\mu \psi(x) - m_0\bar{\psi}(x)\psi(x). \tag{186}$$

However, in order to avoid the problems of the singular behavior of the potential associated with monopoles and its point-like source, we use the electric gauge in which the magnetic potential becomes regular dual magnetic potential $B^{(d)}_\mu$ and

coupled with its point like magnetic source represented by a complex scalar field $\phi(x)$. Taking this consideration into the account, the modified form of the dual QCD Lagrangian (Eq. (186)) in quenched approximation is given as follows:

$$\boldsymbol{L}_m^{(d)} = -\frac{1}{4}B_{\mu\nu}^2 + \left|\left[\partial_\mu + i\frac{4\pi}{g}B_\mu^{(d)}\right]\phi\right|^2 - 3\lambda\alpha_s^{-2}(\phi^*\phi - \phi_0^2)^2. \tag{187}$$

The quadratic effective renormalized potential is appropriate for inducing the dynamical breaking of magnetic symmetry that forces the magnetic condensation resulting in dual Meisner effect with the QCD vacuum in a state of magnetic superconductor which, with the formation of flux tubes, confines the color isocharges.

The nature of magnetically condensed vacuum and the associated flux tube structure may be analyzed using the field equations resulting from the Lagrangian (Eq. (187)) into the following form:

$$\begin{aligned} \boldsymbol{D}^\mu\boldsymbol{D}_\mu\phi + 6\lambda\alpha_s^{-2}(\phi^*\phi - \phi_0^2)\phi = 0, \\ \partial^\nu B_{\mu\nu} - i\frac{4\pi}{g}(\phi^* \overleftrightarrow{\partial}_\mu \phi) - 8\pi\alpha_s^{-1}B_\mu^{(d)}\phi\phi^* = 0, \end{aligned} \tag{188}$$

with $\boldsymbol{D}_\mu = \partial_\mu + i4\pi g^{-1}B_\mu^{(d)}$. The close agreement of these field equations with the Neilsen and Olesen[229] interpretation of vortex-like solutions indicates the flux-tube like configurations inside the QCD vacuum. It leads to the possibility of the existence of the monopole pairs inside the superconducting vacuum in the form of thin flux tubes that may be responsible for the confinement of any colored fluxes. Under cylindrical symmetry (ρ, φ, z) and the field ansatz $B_\varphi^{(d)}(x) = B(\rho)$, $B_0^{(d)} = B_\rho^{(d)} = B_z^{(d)} = 0$ and $\phi(x) = \exp(in\varphi)\chi(\rho)$ $(n = 0, \pm1, \pm2, --)$, the field equations given by Eq. 188 are transformed to the following form:

$$\begin{aligned} \frac{1}{\rho}\frac{d}{d\rho}\left(\rho\frac{d\chi}{d\rho}\right) - \left[\left(\frac{n}{\rho} + (4\pi\alpha_s^{-1})^{\frac{1}{2}}B(\rho)\right)^2 - 6\lambda\alpha_s^{-2}(\chi^2 - \phi_0^2)\right]\chi(\rho) = 0, \\ \frac{d}{d\rho}\left[\rho^{-1}\frac{d}{d\rho}(\rho B(\rho))\right] + 8\pi g^{-1}\left(\frac{n}{\rho} - 4\pi g^{-1}B(\rho)\right)\chi^2(\rho) = 0. \end{aligned} \tag{189}$$

Further, with these considerations, the form of the color electric field in the z-direction is given by

$$E_m(\rho) = -\frac{1}{\rho}\frac{d}{d\rho}(\rho B(\rho)). \tag{190}$$

Equation (189) is desired field equations that govern the dynamics of dual QCD vacuum and coincides exactly with those of the ordinary single vortex solution in cylindrical framework. The highly nonlinear coupled structure of these differential equations does not allow us to go through their exact solutions. Hence, their asymptotic solution using the boundary conditions $\phi \to \phi_0$ as $\rho \to \infty$ leading to the appropriate asymptotic solution for the dual gauge potential that ensures the

formation of color flux tubes is given by

$$B(\rho) = -ng(4\pi\rho)^{-1}[1 + F(\rho)] \quad \text{and} \quad F(\rho) \overset{\rho\to\infty}{\longrightarrow} C\rho^{\frac{1}{2}}\exp(-m_B\rho), \tag{191}$$

where C is a constant and $m_B(= 4\pi g^{-1}\sqrt{2}\phi_0)$ is the glueball mass. In dual QCD scenario, the dynamical breaking of magnetic symmetry sets two characteristic mass scales, The vector mass mode m_B determines the magnitude of dual Meissner effect whereas the scalar mass mode m_ϕ tells the rate of magnetic condensation. The ratio of these two mass scales reflects the nature of dual QCD vacuum in terms of dual Ginzberg–Landau parameter[222–224] which in the relatively weak coupling limit (for $\alpha_s = 0.12$ and 0.24) exhibit the type-II superconducting behavior ($K^d_{QCD} > 1$) with multi-flux tube configurations. Thus, the gauge invariant field decomposition formulation (based on magnetic symmetry) by utilizing its topological structure gives a viable explanation of the mysterious confining behavior of QCD at the fundamental level.

18.3. *Quark–hadron phase transition in dual QCD*

The color confining features of QCD vacuum as a result of the formation of color flux tubes can be visualized more effectively by evaluating the energy per unit length of the flux tube structure in cylindrical system[225] as

$$k = 2\pi \int_0^\infty \rho\, d\rho \left[\frac{n^2 g^2 \rho^{-2}}{32\pi^2} F'^2 + \frac{n^2}{\rho^2} F^2(\rho)\chi^2(\rho) + \chi'^2 + \frac{48\pi^2}{g^4}(\chi^2(\rho) - \phi_0^2)^2\right]. \tag{192}$$

It, in turn, plays an important role in the phase structure of QCD vacuum if we take the multi-flux tube system on an S^2-sphere with periodically distributed flux tubes and introduce a new variable R on S^2 and express it as $\rho = R\sin\theta$. As a result, a number of flux tubes considered inside a hadronic sphere of radius R pass through the two poles of the hadronic sphere. Under such prescription, the flux tube solution governed by Eq. (191) corresponds to the case of large R limit ($R \to \infty$) such that $R \gg \rho$ and $\theta \to 0$. With these considerations, the finite energy expression given by above Eq. (192) may be re-expressed as

$$k = \varepsilon_C + \varepsilon_D + \varepsilon_0 \quad \text{with } \varepsilon_C = k_C R^2, \quad \varepsilon_D = k_D R^{-2}, \quad \varepsilon_0 = k_0, \tag{193}$$

where the functions k_C, k_D and k_0 are given by

$$k_C = \frac{96\pi^3}{g^4} \int_0^\pi [\chi^2(\theta) - \phi_0^2]^2 \sin\theta\, d\theta, \tag{194}$$

$$k_D = \frac{n^2 g^2}{16\pi^2} \int_0^\pi \frac{1}{\sin\theta} \left(\frac{\partial F}{\partial \theta}\right)^2 d\theta, \tag{195}$$

$$k_0 = 2\pi \int_0^\pi \left[\frac{n^2 F^2(\theta)\chi^2(\theta)}{\sin\theta} + \sin\theta \left(\frac{\partial \chi}{\partial \theta}\right)^2\right] d\theta. \tag{196}$$

The energy expression (Eq. (193)) provides a straightforward description of the behavior of QCD vacuum at different energy scales. At large distance scale, the first term (ε_C) in Eq. (193) dominates which increases at increasing hadronic distances and gets minimized when the monopole field acquires its vacuum expectation value (ϕ_0) which incidentally acts as an order parameter and will dynamically break the magnetic symmetry of the system. The resulting magnetic condensation then forces the color electric field to transform into the form of the thin flux tubes extending from $\theta = 0$ to $\theta = \pi$ and the QCD vacuum is ultimately pushed to the confining phase. For the computation of associated critical parameters, we proceed by evaluating the functions associated with the expression (Eq. (193)) in the following way:[225]

$$k_C = \frac{6\pi}{\alpha_s^2} \int_0^\pi [\chi^2(\theta) - \phi_0^2]^2 \sin\theta \, d\theta \Rightarrow k_C = \frac{3m_B^4}{16\pi}, \tag{197}$$

which shows the direct dependency of confining energy on the vector glueball mass of the magnetically condensed vacuum. On the other hand, the dominating component of energy expression in short distance limit (ε_D) may also be evaluated in the following form:

$$k_D = \pi R^4 \int_0^\pi E_m^2(\theta) \sin\theta d\theta \quad \text{where } E_m(\theta) = \frac{ng}{4\pi R^2 \sin\theta} \frac{\partial F}{\partial \theta}. \tag{198}$$

Using Eqs. (191) and (195) along with the flux quantization condition given by

$$\int \rho \; E_m(\rho) d\rho = \frac{ng}{4\pi} \tag{199}$$

then leads to

$$k_D = \frac{n^2 g^2}{8\pi} = \frac{1}{2} n^2 \alpha_s. \tag{200}$$

For the confinement–deconfinement phase transition, we have $\varepsilon_D/\varepsilon_C = 1$ and $R = R_c$ which leads to the critical radius and density of phase transition in the following form:

$$R_c = \left(\frac{2}{3} n^2 g^2\right)^{\frac{1}{4}} m_B^{-1} \quad \text{and} \quad d_c = \frac{1}{2\pi R_c^2} = \left(\frac{8}{3}\pi^2 n^2 g^2\right)^{-\frac{1}{2}} m_B^2. \tag{201}$$

Equation (201) exhibits that the critical radius and critical density of phase transition are clearly expressible in terms of free parameters of the QCD vacuum. In view of the running nature of QCD coupling constant, we can estimate these critical factors associated with the QCD vacuum in its infrared sector using the numerical estimations of glueball masses.[226,227] For instance, for the optimal value of (α_s) as

$\alpha_s \equiv 0.12$ with the glueball masses $m_B = 2.102\,\text{GeV}$ and $m_\phi = 4.205\,\text{GeV}$, Eq. (17) leads to $R_c = 0.094\,\text{fm}$ and $d_c = 18.003\,\text{fm}^{-2}$.

The deconfinement phase transition in the dual QCD vacuum therefore expected to appear around the above-mentioned critical values for a typical coupling of $\alpha_s = 0.12$ in the near-infrared region of QCD. In this case, for $R_c \equiv 0.094\,\text{fm}$, the corresponding flux tube number density acquires its critical value of $18.003\,\text{fm}^{-2}$ and the first part of the energy expression (Eq. (193)) dominates which demonstrates the confinement of color isocharges in the low energy–momentum scale of QCD vacuum. However, below $R_c = 0.094$ fm, the quarks and gluons appear as free states and the system shifted toward electrically dominated deconfined phase and mathematically govern by the second part of the expression (Eq. (193)). Consequently, there is the possibility of sharp increase in the flux tube number density tube system; the flux tube annihilation may take place which then leads to the generation of dynamical quarks and gluons. The gluon self-interactions are then expected to play a major role in the thermalization of QCD system and create an intermediate state of quark–gluon plasma (QGP). As a result of such flux tube melting in the high momentum transfer sector of QCD vacuum, the system is expected to evolve with an intermediatory QGP phase.

Furthermore, the general form of color-electric field may be evaluated by using equation (Eq. (190)) for the case of multi-flux tube system on the S^2-sphere is obtained as

$$E_m(\theta) = \tilde{E}_m(\theta)\exp(-Rm_B\sin\theta), \tag{202}$$

where $\tilde{E}_m(\theta) = \frac{nC\alpha_s^{1/2}}{4\pi^{1/2}R^{3/2}\sin^{3/2}\theta}(1 - 2Rm_B\sin\theta)$. The profile of such color electric field as a function of the polar angle θ for different values of radius (R) at $\alpha_s = 0.12$ in the infrared sector of QCD has been presented by a $(2-d)$ graphics given by Fig. 49. It clearly shows that in the infrared sector of QCD, for a large sphere enclosing the flux tubes, the color electric flux gets localized or spread around the poles ($\theta = 0$ and π) while it gets uniformly distributed for the small sphere case and acquires a constant value at the critical radius R_c as given by Eq. (201).

18.4. *Summary and conclusions*

In this paper, we have studied the color confining structure of dual QCD vacuum in the SU(2) pure gauge theory at zero temperature. In the present scenario for the nonperturbative regime of QCD, the flux tube configuration in dual QCD vacuum has been analyzed by breaking the magnetic symmetry of the system in a dynamical way. Its implication, in turn, is extended to discuss the dynamics of quark–hadron phase transition by computing the associated critical parameters of phase transition at zero temperature. Further, the study of chromoelectric field profiles at different length scales on S^2- sphere has been shown to lead that at large distance scale, the color electric flux is localized toward the pole ($\theta = o, \pi$) where QCD monopole gets condensed while at small distance scale its uniform distribution takes place and at

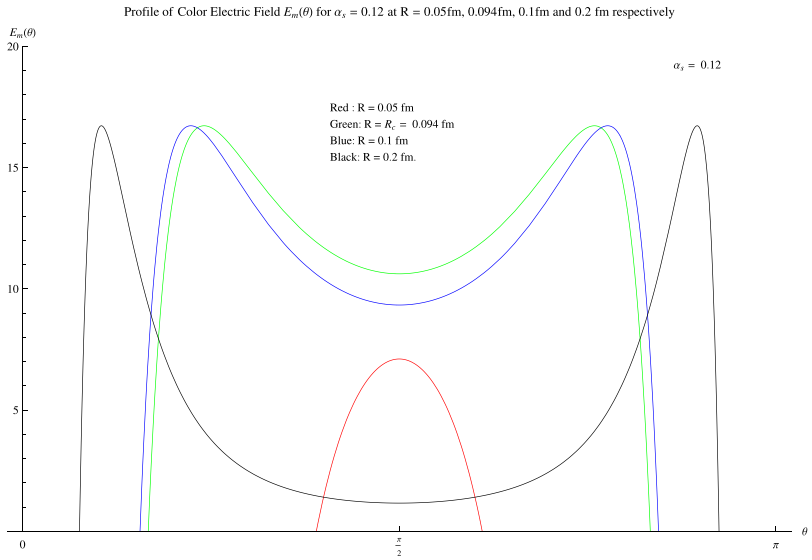

Fig. 49. (Color online) Profiles of color electric field $E_m(\theta)$ for $\alpha_s = 0.12$ as a function of θ.

$R = R_c$, the whole flux is shifted at the central region where QCD monopole density vanishes. Such variation of color electric field with the length scale also indicates the possibility of the formation of QGP before acquiring the fully deconfined state in the high energy regime. It may, therefore, be concluded that below the R_c, the topological configurations appearing within the QCD vacuum and their condensation at large distance scales can produce confining features in the system. The chromoelectric field profiles in the thermal environment[225] indicates the decreasing amplitude of the field as the temperature is increased toward and above the deconfinement temperature and shows good agreement with Monte Carlo simulation studies.[230]

The present gauge independent dual QCD formulation with its essential validity in the nonperturbative regime of QCD supported by recent lattice QCD studies[228,230] may be useful to investigate the dynamical problem like plasma oscillation and stability of flux tube configuration in a viable dual QCD formulation.

Acknowledgments

This writeup is a compilation of the contributions as presented in the "Workshop on Dynamics of QCD Matter" held from August 15–17, 2019, in NISER Bhubaneswar, India. The aim of this workshop was to enhance the direct exchange of scientific information among the younger members of the Relativistic Heavy-Ion Community in India, both from the experiments and theory. The focus of the discussions was on the fundamental understanding of strongly interacting matter at extreme conditions, as formed in ultra-relativistic nucleus–nucleus collisions, as well as on emergent QCD phenomena in high-multiplicity proton–proton

and proton–nucleus collisions. Organizers of the Workshop on Dynamics of QCD Matter (2019), Amaresh Jaiswal, Najmul Haque, Victor Roy, Ranbir Singh, Varchaswi Kashyap and Sudipan De, would like to thank NISER, particularly its head Prof. Sudhakar Panda. Special thanks to Professor Ashok Mahapatra, the chairperson of the School of Physical Sciences, for the encouragement and support. Last but not the least, we thank Department of Atomic Energy, Govt. of India, for providing the financial support. Lokesh Kumar acknowledges discussions with Bedangadas Mohanty and Natasha Sharma. The support from the SERB Grant No. ECR/2016/000109 is acknowledged and would like to thank the ALICE collaboration. Victor Roy is supported by the DST-INSPIRE Faculty research grant, India. Deeptak Biswas, Ritesh Ghosh and Deependra Singh Rawat are thankful to UGC, New Delhi for the financial assistance. Sabyasachi Ghosh thanks his collaborators Sourav Sarkar, Santosh K. Das, Jane Alam, Gastao Krein, Bedangadas Mohanty, Hiranmoy Mishra, Sandeep Chatterjee, Victor Roy, Sukanya Mitra, Anirban Lahiri, Sarbani Majumder, Rajarshi Ray, Sanjay K. Ghosh, whose direct/indirect impact is linked with the investigation series, which is briefly reviewed in present contribution. Sabyasachi Ghosh and Jayanta Dey acknowledge IIT-Bhilai, funded by Ministry of Human Resource Development (MHRD), Government of India. Ralf Rapp has been supported by the U.S. National Science Foundation under grant no. PHY-1913286. Work partially supported by Conselho Nacional de Desenvolvimento Científico e Tecnológico — CNPq, Grants. no. 304758/2017-5 (R.L.S.F), 305894/2009-9 (Gastão Krein), and 464898/2014-5(G.K) (INCT Física Nuclear e Aplicacões), and Fundacão de Amparo à Pesquisa do Estado do Rio Grande do Sul (FAPERGS), Grant No. 19/2551-0000690-0 (Ricardo L. S. Farias), and Fundacão de Amparo à Pesquisa do Estado de São Paulo (FAPESP), Grant No. 2013/01907-0 (Gastão Krein) and Coordenacão de Aperfeicoamento de Pessoal de Nível Superior (CAPES) (A.B.) — Brasil (CAPES) — Finance Code 001. Deeptak Biswas acknowledges kind hospitality of NISER. Amaresh Jaiswal is supported in part by the DST-INSPIRE faculty award under Grant No. DST/INSPIRE/04/2017/000038. Sutanu Roy is supported in part by the SERB Early Career Research Award under Grant No. ECR/2017/001354. Sumana Bhattacharyya was supported by the Council of Scientific and Industrial Research (CSIR), India. Vinod Chandra would like to acknowledge SERB for the Early Career Research Award (ECRA/2016), and DST, Govt. of India for INSPIRE-Faculty Fellowship (IFA-13/PH-55). Avdhesh Kumar thanks Wojciech Florkowski and Radoslaw Ryblewski for a very fruitful collaboration. This research was supported in part by the Polish National Science Center Grant No. 2016/23/B/ST2/00717. Arpan Das, Ritesh Ghosh, Sabyasachi Ghosh, Lokesh Kumar and Deependra Singh Rawat acknowledge the organizers of "Workshop on Dynamics of QCD matter 2019" for the invitation. All authors of this paper have contributed only to those sections of the report, which they cosign with their name. Only those have collaborated together, whose names appear together in the header of a given section.

References

1. ALICE (S. Acharya *et al.*), *Phys. Lett. B* **790** (2019) 35, arXiv:1805.04432 [nucl-ex].
2. C. Loizides, *Phys. Rev. C* **94** (2016) 024914, arXiv:1603.07375 [nucl-ex].
3. ALICE (A. G. Knospe), *PoS LHCP* **2018** (2018) 217.
4. ALICE (B. Abelev *et al.*), *Phys. Rev. C* **88** (2013) 044910, arXiv:1303.0737 [hep-ex].
5. ALICE (J. Adam *et al.*), *Phys. Lett. B* **760** (2016) 720, arXiv:1601.03658 [nucl-ex].
6. ALICE (J. Adam *et al.*), *Nature Phys.* **13** (2017) 535, arXiv:1606.07424 [nucl-ex].
7. ALICE (J. Adam *et al.*), *Phys. Lett. B* **758** (2016) 389, arXiv:1512.07227 [nucl-ex].
8. ALICE (B. B. Abelev *et al.*), *Phys. Lett. B* **728** (2014) 25, arXiv:1307.6796 [nucl-ex].
9. P. Koch, B. Muller and J. Rafelski, *Phys. Rep.* **142** (1986) 167.
10. ALICE (S. Acharya *et al.*), *Phys. Rev. C* **99** (2019) 024906, arXiv:1807.11321 [nucl-ex].
11. N. Sharma, J. Cleymans and L. Kumar, *Eur. Phys. J. C* **78** (2018) 288, arXiv:1802.07972 [hep-ph].
12. A. G. Knospe, C. Markert, K. Werner, J. Steinheimer and M. Bleicher, *Phys. Rev. C* **93** (2016) 014911, arXiv:1509.07895 [nucl-th].
13. F. Becattini, F. Piccinini and J. Rizzo, *Phys. Rev. C* **77** (2008) 024906, arXiv:0711.1253 [nucl-th].
14. D. E. Kharzeev, L. D. McLerran and H. J. Warringa, *Nucl. Phys. A* **803** (2008) 227, arXiv:0711.0950 [hep-ph].
15. Z. T. Liang and X. N. Wang, *Phys. Lett. B* **629** (2005) 20, arXiv:nucl-th/0411101 [nucl-th].
16. Y. G. Yang, R. H. Fang, Q. Wang and X. N. Wang, *Phys. Rev. C* **97** (2018) 034917, arXiv:1711.06008 [nucl-th].
17. U. Fano, *Rev. Mod. Phys.* **29** (1957) 74.
18. V. Skokov, A. Y. Illarionov and V. Toneev, *Int. J. Mod. Phys. A* **24** (2009) 5925, arXiv:0907.1396 [nucl-th].
19. R. C. Duncan and C. Thompson, *Astrophys. J. Lett.* **392** (1992) L9.
20. J. Alexandre, *Phys. Rev. D* **63** (2001) 073010, arXiv:hep-th/0009204 [hep-th].
21. W. Y. Tsai, *Phys. Rev. D* **10** (1974) 2699.
22. A. Das and N. Haque, *Phys. Rev. D* **101** (2020) 074033, arXiv:1908.10323 [hep-ph].
23. A. Ayala, R. L. S. Farias, S. Hernndez-Ortiz, L. A. Hernndez, D. M. Paret and R. Zamora, *Phys. Rev. D* **98** (2018) 114008, arXiv:1809.08312 [hep-ph].
24. G. S. Bali, B. B. Brandt, G. Endrődi and B. Gläßle, *Phys. Rev. D* **97** (2018) 034505, arXiv:1707.05600 [hep-lat].
25. R. V. Gavai and S. Gupta, *Phys. Rev. D* **71** (2005) 114014,
26. H. Niemi, G. S. Denicol, H. Holopainen and P. Huovinen, *Phys. Rev. C* **87** (2013) 054901,
27. A. Dash and V. Roy, arXiv:1908.05292 [hep-ph].
28. A. Bacchetta, *Eur. Phys. J. A* **52** (2016) 163.
29. L. V. Gribov, E. M. Levin and M. G. Ryskin, *Phys. Rep.* **100** (1983) 1.
30. F. Dominguez, C. Marquet, B. W. Xiao and F. Yuan, *Phys. Rev. D* **83** (2011) 105005, arXiv:1101.0715 [hep-ph].
31. M. G. A. Buffing, P. J. Mulders and A. Mukherjee, *Int. J. Mod. Phys. Conf. Ser.* **25** (2014) 1460003, arXiv:1309.2472 [hep-ph].
32. Y. Hatta, B. W. Xiao and F. Yuan, *Phys. Rev. Lett.* **116** (2016) 202301, arXiv:1601.01585 [hep-ph].
33. B. W. Xiao, F. Yuan and J. Zhou, *Nucl. Phys. B* **921** (2017) 104, arXiv:1703.06163 [hep-ph].

34. M. Siddiqah, N. Vasim, K. Banu, R. Abir and T. Bhattacharyya, *Phys. Rev. D* **97** (2018) 054009, arXiv:1801.01637 [hep-ph].
35. E. Levin and K. Tuchin, *Nucl. Phys. B* **573** (2000) 833, arXiv:hep-ph/9908317.
36. E. Levin and K. Tuchin, *Nucl. Phys. A* **691** (2001) 779, arXiv:hep-ph/0012167.
37. M. Prakash, M. Prakash, R. Venugopalan and G. Welke, *Phys. Rep.* **227** (1993) 321.
38. P. Romatschke and S. Pratt, arXiv:1409.0010 [nucl-th].
39. A. Djouadi, *Phys. Rep.* **457** (2008) 1, arXiv:hep-ph/0503172.
40. D. d'Enterria and C. Loizides, arXiv:1809.06832 [hep-ph].
41. J. Ghiglieri and U. A. Wiedemann, *Phys. Rev. D* **99** (2019) 054002, arXiv:1901.04503 [hep-ph].
42. S. Caron-Huot, *Phys. Rev. D* **79** (2009) 125009, arXiv:0903.3958 [hep-ph].
43. K. G. Wilson, *Phys. Rev.* **179** (1969) 1499.
44. K. G. Wilson and W. Zimmermann, *Commun. Math. Phys.* **24** (1972) 87.
45. G. D. Moore and O. Saremi, *J. High Energy Phys.* **0809** (2008) 015,
46. M. Laine, M. Vepsalainen and A. Vuorinen, *J. High Energy Phys.* **1010** (2010) 010, arXiv:1008.3263 [hep-ph].
47. K. Fukushima, *Lect. Notes Phys.* **871** (2013) 241, arXiv:1209.5064 [hep-ph].
48. L. McLerran and V. Skokov, *Nucl. Phys. A* **929** (2014) 184, arXiv:1305.0774 [hep-ph].
49. A. Bandyopadhyay, C. A. Islam and M. G. Mustafa, *Phys. Rev. D* **94** (2016) 114034, arXiv:1602.06769 [hep-ph].
50. B. Karmakar, R. Ghosh, A. Bandyopadhyay, N. Haque and M. G. Mustafa, *Phys. Rev. D* **99** (2019) 094002, arXiv:1902.02607 [hep-ph].
51. A. Das, A. Bandyopadhyay, P. K. Roy and M. G. Mustafa, *Phys. Rev. D* **97** (2018) 034024, arXiv:1709.08365 [hep-ph].
52. B. Karmakar, A. Bandyopadhyay, N. Haque and M. G. Mustafa, *Eur. Phys. J. C* **79** (2019) 658, arXiv:1804.11336 [hep-ph].
53. A. Perez Martinez, H. Perez Rojas and H. Mosquera Cuesta, *Int. J. Mod. Phys. D* **17** (2008) 2107, arXiv:0711.0975 [astro-ph].
54. T. Schäfer and D. Teaney, *Rep. Prog. Phys.* **72** (2009) 126001, arXiv:0904.3107 [hep-ph].
55. P. B. Arnold, G. D. Moore and L. G. Yaffe, *J. High Energy Phys.* **11** (2000) 001, arXiv:hep-ph/0010177 [hep-ph].
56. R. Marty, E. Bratkovskaya, W. Cassing, J. Aichelin and H. Berrehrah, *Phys. Rev. C* **88** (2013) 045204, arXiv:1305.7180 [hep-ph].
57. C. Sasaki and K. Redlich, *Nucl. Phys. A* **832** (2010) 62, arXiv:0811.4708 [hep-ph].
58. S. Ghosh, T. C. Peixoto, V. Roy, F. E. Serna and G. Krein, *Phys. Rev. C* **93** (2016) 045205, arXiv:1507.08798 [nucl-th].
59. P. Deb, G. P. Kadam and H. Mishra, *Phys. Rev. D* **94** (2016) 094002, arXiv:1603.01952 [hep-ph].
60. P. Chakraborty and J. I. Kapusta, *Phys. Rev. C* **83** (2011) 014906, arXiv:1006.0257 [nucl-th].
61. P. Singha, A. Abhishek, G. Kadam, S. Ghosh and H. Mishra, *J. Phys. G* **46** (2019) 015201, arXiv:1705.03084 [nucl-th].
62. R. Lang and W. Weise, *Eur. Phys. J. A* **50** (2014) 63, arXiv:1311.4628 [hep-ph].
63. W. Cassing, O. Linnyk, T. Steinert and V. Ozvenchuk, *Phys. Rev. Lett.* **110** (2013) 182301, arXiv:1302.0906 [hep-ph].
64. S. Ghosh, B. Chatterjee, P. Mohanty, A. Mukharjee and H. Mishra, *Phys. Rev. D* **100** (2019) 034024, arXiv:1804.00812 [hep-ph].
65. D. Fernandez-Fraile and A. Gomez Nicola, arXiv:0902.4829 [hep-ph].

66. S. Ghosh, G. Krein and S. Sarkar, *Phys. Rev. C* **89** (2014) 045201, arXiv:1401.5392 [nucl-th].
67. S. Ghosh, *Phys. Rev. C* **90** (2014) 025202, arXiv:1503.06927 [nucl-th].
68. S. Ghosh, *Braz. J. Phys.* **45** (2015) 687, arXiv:1507.01705 [nucl-th].
69. M. Rahaman, S. Ghosh, S. Ghosh, S. Sarkar and J. E. Alam, *Phys. Rev. C* **97** (2018) 035201, arXiv:1708.08300 [nucl-th].
70. P. Kalikotay, N. Chaudhuri, S. Ghosh, U. Gangopadhyaya and S. Sarkar, *Eur. Phys. J. A* **56** (2020) 79, arXiv:1908.02933 [nucl-th].
71. S. Ghosh, S. Ghosh and S. Bhattacharyya, *Phys. Rev. C* **98** (2018) 045202, arXiv:1807.03188 [hep-ph].
72. S. Ghosh, S. Samanta, S. Ghosh and H. Mishra, *Int. J. Mod. Phys. E* **28** (2019) 1950036, arXiv:1906.06029 [nucl-th].
73. J. Noronha-Hostler, J. Noronha and C. Greiner, *Phys. Rev. Lett.* **103** (2009) 172302, arXiv:0811.1571 [nucl-th].
74. G. P. Kadam and H. Mishra, *Phys. Rev. C* **92** (2015) 035203, arXiv:1506.04613 [hep-ph].
75. S. Ghosh, S. Chatterjee and B. Mohanty, *Phys. Rev. C* **94** (2016) 045208, arXiv:1607.04779 [nucl-th].
76. S. Ghosh, *Phys. Rev. D* **95** (2017) 036018, arXiv:1607.01340 [nucl-th].
77. L. P. Csernai, J. I. Kapusta and L. D. McLerran, *Phys. Rev. Lett.* **97** (2006) 152303, arXiv:nucl-th/0604032 [nucl-th].
78. J. I. Kapusta, *Landolt-Bornstein* **23** (2010) 563, arXiv:0809.3746 [nucl-th].
79. S. S. Adler *et al.* [PHENIX], *Phys. Rev. Lett.* **91** (2003) 182301, arXiv:nucl-ex/0305013 [nucl-ex].
80. P. Romatschke and U. Romatschke, *Phys. Rev. Lett.* **99** (2007) 172301, arXiv:0706.1522 [nucl-th].
81. A. Jaiswal and V. Roy, *Adv. High Energy Phys.* **2016** (2016) 9623034, arXiv:1605.08694 [nucl-th].
82. N. Demir and S. A. Bass, *Phys. Rev. Lett.* **102** (2009) 172302, arXiv:0812.2422 [nucl-th].
83. J. B. Rose, J. M. Torres-Rincon, A. Schäfer, D. R. Oliinychenko and H. Petersen, *Phys. Rev. C* **97** (2018) 055204, arXiv:1709.03826 [nucl-th].
84. E. Quack and S. P. Klevansky, *Phys. Rev. C* **49** (1994) 3283,
85. S. Ghosh, A. Lahiri, S. Majumder, R. Ray and S. K. Ghosh, *Phys. Rev. C* **88** (2013) 068201, arXiv:1311.4070 [nucl-th].
86. H. B. Meyer, *Phys. Rev. D* **76** (2007) 101701, arXiv:0704.1801 [hep-lat].
87. K. Saha, S. Ghosh, S. Upadhaya and S. Maity, *Phys. Rev. D* **97** (2018) 116020, arXiv:1711.10169 [nucl-th].
88. H. B. Meyer, *Phys. Rev. Lett.* **100** (2008) 162001, arXiv:0710.3717 [hep-lat].
89. P. B. Arnold, C. Dogan and G. D. Moore, *Phys. Rev. D* **74** (2006) 085021, arXiv:hep-ph/0608012 [hep-ph].
90. S. Gupta, *Phys. Lett. B* **597** (2004) 57, arXiv:hep-lat/0301006 [hep-lat].
91. G. Aarts, C. Allton, A. Amato, P. Giudice, S. Hands and J. I. Skullerud, *J. High Energy Phys.* **02** (2015) 186, arXiv:1412.6411 [hep-lat].
92. S. Jeon and V. Koch, *Phys. Rev. Lett.* **83** (1999) 5435, arXiv:nucl-th/9906074 [nucl-th].
93. H. T. Elze, M. Gyulassy and D. Vasak, *Nucl. Phys. B* **276** (1986) 706,
94. H. T. Elze, M. Gyulassy and D. Vasak, *Phys. Lett. B* **177** (1986) 402,
95. S. R. De Groot, W. A. Van Leeuwen and C. G. Van Weert, *Relativistic Kinetic Theory. Principles and Applications* (North-Holland, Amsterdam, Netherlands, 1980).

96. N. Weickgenannt, X. L. Sheng, E. Speranza, Q. Wang and D. H. Rischke, *Phys. Rev. D* **100** (2019) 056018, arXiv:1902.06513 [hep-ph].
97. S. Mao and D. H. Rischke, *Phys. Lett. B* **792** (2019) 149, arXiv:1812.06684 [hep-th].
98. X. L. Sheng, R. H. Fang, Q. Wang and D. H. Rischke, *Phys. Rev. D* **99** (2019) 056004, arXiv:1812.01146 [hep-ph].
99. X. l. Sheng, D. H. Rischke, D. Vasak and Q. Wang, *Eur. Phys. J. A* **54** (2018) 21, arXiv:1707.01388 [hep-ph].
100. F. Karsch and E. Laermann, *Phys. Rev. D* **50** (1994) 6954, arXiv:hep-lat/9406008 [hep-lat].
101. P. Zhuang, J. Hufner and S. P. Klevansky, *Nucl. Phys. A* **576** (1994) 525,
102. C. Sasaki, B. Friman and K. Redlich, *Phys. Rev. D* **75** (2007) 074013, arXiv:hep-ph/0611147 [hep-ph].
103. I. A. Shovkovy, *Lect. Notes Phys.* **871** (2013) 13, arXiv:1207.5081 [hep-ph].
104. D. E. Kharzeev, *Prog. Part. Nucl. Phys.* **75** (2014) 133, arXiv:1312.3348 [hep-ph].
105. M. Buballa, *Phys. Rep.* **407** (2005) 205, arXiv:hep-ph/0402234 [hep-ph].
106. K. Fukushima, M. Ruggieri and R. Gatto, *Phys. Rev. D* **81** (2010) 114031, arXiv:1003.0047 [hep-ph].
107. M. N. Chernodub and A. S. Nedelin, *Phys. Rev. D* **83** (2011) 105008, arXiv:1102.0188 [hep-ph].
108. R. Gatto and M. Ruggieri, *Phys. Rev. D* **85** (2012) 054013, arXiv:1110.4904 [hep-ph].
109. M. Ruggieri and G. X. Peng, *J. Phys. G* **43** (2016) 125101, arXiv:1602.05250 [hep-ph].
110. L. Yu, H. Liu and M. Huang, *Phys. Rev. D* **94** (2016) 014026, arXiv:1511.03073 [hep-ph].
111. R. L. S. Farias, D. C. Duarte, G. Krein and R. O. Ramos, *Phys. Rev. D* **94** (2016) 074011, arXiv:1604.04518 [hep-ph].
112. V. V. Braguta, E. M. Ilgenfritz, A. Y. Kotov, B. Petersson and S. A. Skinderev, *Phys. Rev. D* **93** (2016) 034509, arXiv:1512.05873 [hep-lat].
113. V. V. Braguta, V. A. Goy, E. M. Ilgenfritz, A. Y. Kotov, A. V. Molochkov, M. Muller-Preussker and B. Petersson, *J. High Energy Phys.* **06** (2015) 094, arXiv:1503.06670 [hep-lat].
114. R. L. S. Farias, G. Dallabona, G. Krein and O. A. Battistel, *Phys. Rev. C* **73** (2006) 094, arXiv:hep-ph/0510145 [hep-ph].
115. S. S. Avancini, A. Bandyopadhyay, D. C. Duarte and R. L. S. Farias, *Phys. Rev. D* **100** (2019) 116002, arXiv:1907.09880 [hep-ph].
116. W. Florkowski, J. Hufner, S. P. Klevansky and L. Neise, *Ann. Phys.* **245** (1996) 445, arXiv:hep-ph/9505407 [hep-ph].
117. V. Dmitrasinovic, *Phys. Rev. C* **53** (1996) 1383,
118. A. Das, D. Kumar and H. Mishra, *Phys. Rev. D* **100** (2019) 094030, arXiv:1907.12332 [hep-ph].
119. D. C. Duarte, R. L. S. Farias and R. O. Ramos, *Phys. Rev. D* **99** (2019) 016005, arXiv:1811.10598 [hep-ph].
120. J. K. Boomsma and D. Boer, *Phys. Rev. D* **80** (2009) 034019, arXiv:0905.4660 [hep-ph].
121. J. Rafelski and B. Muller, *Phys. Rev. Lett.* **36** (1976) 517.
122. D. Tong, arXiv:1606.06687 [hep-th].
123. R. L. S. Farias, K. P. Gomes, G. I. Krein and M. B. Pinto, *Phys. Rev. C* **90** (2014) 025203, arXiv:1404.3931 [hep-ph].
124. T. D. Lee and G. C. Wick, *Phys. Rev. D* **9** (1974) 2291,
125. J. C. Collins and M. J. Perry, *Phys. Rev. Lett.* **34** (1975) 1353,

126. N. Itoh, *Prog. Theor. Phys.* **44** (1970) 291,
127. M. Luzum and P. Romatschke, *Phys. Rev. C* **78** (2008) 034915, arXiv:0804.4015 [nucl-th].
128. M. Luzum and P. Romatschke, *Phys. Rev. Lett.* **103** (2009) 262302, arXiv:0901.4588 [nucl-th].
129. H. Song, S. A. Bass, U. Heinz, T. Hirano and C. Shen, *Phys. Rev. Lett.* **106** (2011) 192301, arXiv:1011.2783 [nucl-th].
130. M. Luzum, *Phys. Rev. C* **83** (2011) 044911, arXiv:1011.5173 [nucl-th].
131. B. Schenke, S. Jeon and C. Gale, *Phys. Lett. B* **702** (2011) 59, arXiv:1102.0575 [hep-ph].
132. C. Gale, S. Jeon, B. Schenke, P. Tribedy and R. Venugopalan, *Phys. Rev. Lett.* **110** (2013) 012302, arXiv:1209.6330 [nucl-th].
133. R. S. Bhalerao, A. Jaiswal and S. Pal, *Phys. Rev. C* **92** (2015) 014903, arXiv:1503.03862 [nucl-th].
134. L. D. Landau, *Izv. Akad. Nauk Ser. Fiz.* **17** (1953) 51,
135. BRAHMS (M. J. Murray), arXiv:nucl-ex/0404007 [nucl-ex].
136. BRAHMS (I. G. Bearden *et al.*), *Phys. Rev. Lett.* **94** (2005) 162301, arXiv:nucl-ex/0403050 [nucl-ex].
137. BRAHMS (M. Murray), arXiv:0710.4576 [nucl-ex].
138. P. Steinberg, *Nucl. Phys. A* **752** (2005) 423, arXiv:nucl-ex/0412009 [nucl-ex].
139. P. Steinberg, *PoS CPOD* **2006** (2006) 036, arXiv:nucl-ex/0702019 [nucl-ex].
140. C. Y. Wong, *Phys. Rev. C* **78** (2008) 054902, arXiv:0808.1294 [hep-ph].
141. D. K. Srivastava, J. Alam and B. Sinha, *Phys. Lett. B* **296** (1992) 11,
142. D. K. Srivastava, J. e. Alam, S. Chakrabarty, B. Sinha and S. Raha, *Ann. Phys.* **228** (1993) 104,
143. D. K. Srivastava, J. Alam, S. Chakrabarty, S. Raha and B. Sinha, *Phys. Lett. B* **278** (1992) 225,
144. B. Mohanty and J. E. Alam, *Phys. Rev. C* **68** (2003) 064903, arXiv:nucl-th/0301086 [nucl-th].
145. Y. Hama, T. Kodama and O. Socolowski, Jr., *Braz. J. Phys.* **35** (2005) 24, arXiv:hep-ph/0407264 [hep-ph].
146. C. E. Aguiar, T. Kodama, T. Osada and Y. Hama, *J. Phys. G* **27** (2001) 75, arXiv:hep-ph/0006239 [hep-ph].
147. S. Pratt, *Phys. Rev. C* **75** (2007) 024907, arXiv:nucl-th/0612010 [nucl-th].
148. A. Bialas, R. A. Janik and R. B. Peschanski, *Phys. Rev. C* **76** (2007) 054901, arXiv:0706.2108 [nucl-th].
149. T. Csorgo, M. I. Nagy and M. Csanad, *Phys. Lett. B* **663** (2008) 306, arXiv:nucl-th/0605070 [nucl-th].
150. G. Beuf, R. Peschanski and E. N. Saridakis, *Phys. Rev. C* **78** (2008) 064909, arXiv:0808.1073 [nucl-th].
151. T. Osada and G. Wilk, *Central Eur. J. Phys.* **7** (2009) 432, arXiv:0810.3089 [hep-ph].
152. L. D. Landau and E. M. Lifshitz, *Fluid Mechanics* (Butterworth-Heinemann, Oxford, 1987).
153. D. Biswas, K. Deka, A. Jaiswal and S. Roy, arXiv:1910.13368 [hep-ph].
154. E-0895 (J. L. Klay *et al.*), *Phys. Rev. C* **68** (2003) 054905, arXiv:nucl-ex/0306033 [nucl-ex].
155. NA49 (C. Alt *et al.*), *Phys. Rev. C* **77** (2008) 024903, arXiv:0710.0118 [nucl-ex].
156. NA49 (S. V. Afanasiev *et al.*), *Phys. Rev. C* **66** (2002) 054902, arXiv:nucl-ex/0205002 [nucl-ex].

157. M. Gazdzicki, M. Gorenstein and P. Seyboth, *Acta Phys. Polon. B* **42** (2011) 307, arXiv:1006.1765 [hep-ph].
158. L. N. Gao and F. H. Liu, *Adv. High Energy Phys.* **2015** (2015) 641906, arXiv:1509.09034 [nucl-th].
159. C. Gupt, R. K. Shivpuri, N. S. Verma and A. P. Sharma, *Nuovo Cim. A* **75** (1983) 408.
160. R. J. Fries, B. Muller, C. Nonaka and S. A. Bass, *Phys. Rev. Lett.* **90** (2003) 202303, arXiv:nucl-th/0301087.
161. P. F. Kolb, J. Sollfrank and U. W. Heinz, *Phys. Rev. C* **62** (2000) 054909, arXiv:hep-ph/0006129.
162. S. A. Voloshin, *Nucl. Phys. A* **715** (2003) 379, arXiv:nucl-ex/0210014.
163. Z. W. Lin and C. M. Ko, *Phys. Rev. Lett.* **89** (2002) 202302, arXiv:nucl-th/0207014.
164. H. Grad, *Comm. Pure Appl. Math.* **2** (1949) 331.
165. P. Romatschke, *Int. J. Mod. Phys. E* **19** (2010) 1, arXiv:0902.3663 [hep-ph].
166. A. Jaiswal, *Phys. Rev. C* **87** (2013) 051901, arXiv:1302.6311 [nucl-th].
167. A. Jaiswal, *Phys. Rev. C* **88** (2013) 021903, arXiv:1305.3480 [nucl-th].
168. H. Song, arXiv:0908.3656 [nucl-th].
169. P. Romatschke and U. Romatschke, arXiv:1712.05815 [nucl-th].
170. T. S. Biro, E. van Doorn, B. Muller, M. H. Thoma and X. N. Wang, *Phys. Rev. C* **48** (1993) 1275 [nucl-th/9303004].
171. A. Muronga, *Phys. Rev. Lett.* **88** (2002) 062302; [Erratum-*ibid.* **89** (2002) 159901], arXiv:nucl-th/0104064.
172. A. Jaiswal, R. S. Bhalerao and S. Pal, *Phys. Rev. C* **87** (2013) 021901, arXiv:1302.0666 [nucl-th].
173. W. Florkowski, A. Jaiswal, E. Maksymiuk, R. Ryblewski and M. Strickland, *Phys. Rev. C* **91** (2015) 054907, arXiv:1503.03226 [nucl-th].
174. J. R. Bhatt and V. Sreekanth, *Int. J. Mod. Phys. E* **19** (2010) 299, arXiv:0901.1363 [hep-ph].
175. J. R. Bhatt, H. Mishra and V. Sreekanth, *Phys. Lett. B* **704** (2011) 486 arXiv:1103.4333 [hep-ph].
176. K. Rajagopal and N. Tripuraneni, *J. High Energy Phys.* **1003** (2010) 018 arXiv:0908.1785 [hep-ph].
177. J. R. Bhatt, H. Mishra and V. Sreekanth, *J. High Energy Phys.* **1011** (2010) 106 arXiv:1011.1969 [hep-ph].
178. J. R. Bhatt, H. Mishra and V. Sreekanth, *Nucl. Phys. A* **875** (2012) 181 arXiv:1101.5597 [hep-ph].
179. C. Shen, U. Heinz, P. Huovinen and H. Song, *Phys. Rev. C* **84** (2011) 044903 arXiv:1105.3226 [nucl-th].
180. V. Sreekanth, *manuscript under preparation*
181. S. Mitra and V. Chandra, *Phys. Rev. D* **97** (2018) 034032, arXiv:1801.01700 [nucl-th].
182. V. Chandra and V. Ravishankar, *Phys. Rev. D* **84** (2011) 074013, arXiv:1103.0091 [nucl-th].
183. J. L. Anderson and H. R. Witting *Physica* **74** (1974) 466.
184. M. Bluhm, B. Kampfer and K. Redlich, *Phys. Lett. B* **709** (2012) 77, arXiv:1101.3072 [hep-ph].
185. S. Bhadury, M. Kurian, V. Chandra and A. Jaiswal, *J. Phys. G* **47** (2020) 085108, arXiv:1902.05285 [hep-ph].
186. L. Adamczyk *et al.* [STAR], *Nature* **548** (2017) 62, arXiv:1701.06657 [nucl-ex].
187. J. Adam *et al.* [STAR], *Phys. Rev. C* **98** (2018) 014910, arXiv:1805.04400 [nucl-ex].

188. I. Karpenko and F. Becattini, *Eur. Phys. J. C* **77** (2017) 213, arXiv:1610.04717 [nucl-th].
189. F. Becattini, I. Karpenko, M. Lisa, I. Upsal and S. Voloshin, *Phys. Rev. C* **95** (2017) 054902, arXiv:1610.02506 [nucl-th].
190. F. Becattini and I. Karpenko, *Phys. Rev. Lett.* **120** (2018) 012302, arXiv:1707.07984 [nucl-th].
191. T. Niida [STAR], *Nucl. Phys. A* **982** (2019) 511, arXiv:1808.10482 [nucl-ex].
192. F. Becattini, W. Florkowski and E. Speranza, *Phys. Lett. B* **789** (2019) 419, arXiv:1807.10994 [hep-th].
193. W. Florkowski, B. Friman, A. Jaiswal and E. Speranza, *Phys. Rev. C* **97** (2018) 041901, arXiv:1705.00587 [nucl-th].
194. W. Florkowski, B. Friman, A. Jaiswal, R. Ryblewski and E. Speranza, *Phys. Rev. D* **97** (2018) 116017, arXiv:1712.07676 [nucl-th].
195. W. Florkowski, B. Friman, A. Jaiswal and E. Speranza, *Acta Phys. Polon. Supp.* **10** (2017) 1139, arXiv:1708.04035 [hep-ph].
196. W. Florkowski, B. Friman, A. Jaiswal, R. Ryblewski and E. Speranza, *Acta Phys. Polon. Supp.* **11** (2018) 507, arXiv:1810.01709 [nucl-th].
197. W. Florkowski, A. Kumar and R. Ryblewski, *Phys. Rev. C* **98** (2018) 044906, arXiv:1806.02616 [hep-ph].
198. W. Florkowski, A. Kumar and R. Ryblewski, *Prog. Part. Nucl. Phys.* **108** (2019) 103709, arXiv:1811.04409 [nucl-th].
199. W. Florkowski, A. Kumar, R. Ryblewski and R. Singh, *Phys. Rev. C* **99** (2019) 044910, arXiv:1901.09655 [hep-ph].
200. F. Becattini, V. Chandra, L. Del Zanna and E. Grossi, *Ann. Phys.* **338** (2013) 32, arXiv:1303.3431 [nucl-th].
201. D. Vasak, M. Gyulassy and H. T. Elze, *Ann. Phys.* **173** (1987) 462.
202. W. Florkowski, M. P. Heller and M. Spalinski, *Rept. Prog. Phys.* **81** (2018) 046001, arXiv:1707.02282 [hep-ph].
203. U. W. Heinz and P. F. Kolb, *Nucl. Phys. A* **702** (2002) 269, [hep-ph/0111075].
204. P. Romatschke, *Phys. Rev. Lett.* **120** (2018) 012301, arXiv:1704.08699 [hep-th].
205. W. A. Hiscock and L. Lindblom, *Phys. Rev. D* **31** (1985) 725.
206. I. Muller, *Z. Phys.* **198** (1967) 329.
207. W. Israel and J. M. Stewart, *Ann. Phys.* **118** (1979) 341.
208. J. C. Maxwell, *Phil. Trans. R. Soc.* **157** (1867) 49.
209. M. P. Heller and M. Spalinski, *Phys. Rev. Lett.* **115** (2015) 072501, arXiv:1503.07514 [hep-th].
210. R. Baier, P. Romatschke and U. A. Wiedemann, *Phys. Rev. C* **73** (2006) 064903, [hep-ph/0602249].
211. G. S. Denicol, H. Niemi, E. Molnar and D. H. Rischke, *Phys. Rev. D* **85** (2012) 114047, Erratum: [*Phys. Rev. D* **91** (2015) 039902] arXiv:1202.4551 [nucl-th].
212. S. Jaiswal, C. Chattopadhyay, A. Jaiswal, S. Pal and U. Heinz, *Phys. Rev. C* **100** (2019) 034901, arXiv:1907.07965 [nucl-th].
213. G. S. Denicol and J. Noronha, *Phys. Rev. D* **97** (2018) 056021, arXiv:1711.01657 [nucl-th].
214. C. Chattopadhyay, A. Jaiswal, S. Jaiswal and S. Pal, *Nucl. Phys. A* **982** (2019) 911, arXiv:1807.05544 [nucl-th].
215. M. Strickland, *J. High Energy Phys.* **1812** (2018) 128, arXiv:1809.01200 [nucl-th].
216. A. Behtash, C. N. Cruz-Camacho, S. Kamata and M. Martinez, *Phys. Lett. B* **797** (2019) 134914, arXiv:1805.07881 [hep-th].
217. A. Kurkela, U. A. Wiedemann and B. Wu, arXiv:1907.08101 [hep-ph].

218. D. J. Gross and F. Wilczek, *Phys. Rev. D* **8** (1973) 3633.
219. H. D. Politzer, *Phys. Rev. Lett.* **30** (1973) 1346.
220. Y. Nambu, *Phys. Rev. D* **10** (1974) 4262.
221. G. 't Hooft, *Nucl. Phys. B* **190** (1981) 455.
222. V. P. Pandey and H. C. Chandola, *Phys. Lett. B* **476** (2000) 193.
223. H. C. Chandola and D. Yadav, *Nucl. Phys. A* **829** (2009) 151.
224. D. S. Rawat, H. C. Pandey, H. C. Chandola and D. Yadav, *Springer Proc. Phys.* **203** (2018) 625.
225. H. C. Chandola, D. Singh Rawat, H. C. Pandey, D. Yadav and H. Dehnen, *Adv. High Energy Phys.* **2020** (2020) 4240512, arXiv:1904.11714 [hep-th].
226. Y. M. Cho, *Phys. Rev. D* **21** (1980) 1080.
227. Y. M. Cho, *Phys. Rev. D* **23** (1981) 2415.
228. Y. M. Cho, F. H. Cho and J. H. Yoon, *Phys. Rev. D* **87** (2013) 085025, arXiv:1206.6936 [hep-th].
229. H. B. Nielsen and P. Olesen, *Nucl. Phys. B* **61** (1973) 45.
230. P. Cea, L. Cosmai, F. Cuteri and A. Papa, *J. High Energy Phys.* **1606** (2016) 033, arXiv:1511.01783 [hep-lat].